

Understanding Galaxy Evolution Through Emission Lines

Lisa J. Kewley,^{1,2} David C. Nicholls,^{1,2}
and Ralph S. Sutherland¹

¹Research School for Astronomy & Astrophysics, Australian National University, Canberra, Australian Capital Territory 2611, Australia; email: lisa.kewley@anu.edu.au

²ARC Centre of Excellence for All Sky Astrophysics in 3 Dimensions (ASTRO 3D), Canberra, Australian Capital Territory 2611, Australia

Annu. Rev. Astron. Astrophys. 2019. 57:511–70

First published as a Review in Advance on
July 5, 2019

The *Annual Review of Astronomy and Astrophysics* is
online at astro.annualreviews.org

<https://doi.org/10.1146/annurev-astro-081817-051832>

Copyright © 2019 by Annual Reviews.
All rights reserved

**ANNUAL
REVIEWS CONNECT**

www.annualreviews.org

- Download figures
- Navigate cited references
- Keyword search
- Explore related articles
- Share via email or social media

Keywords

galaxies, HII regions, fundamental parameters

Abstract

We review the use of emission lines for understanding galaxy evolution, focusing on excitation source, metallicity, ionization parameter, ISM pressure, and electron density. We discuss the physics, benefits, and caveats of emission line diagnostics, including the effects of theoretical model uncertainties, diffuse ionized gas, and sample selection bias. In anticipation of upcoming telescope facilities, we provide new self-consistent emission line diagnostic calibrations for complete spectral coverage from the UV to the IR. These diagnostics can be used in concert to understand how fundamental galaxy properties have changed across cosmic time. We conclude the following:

- The UV, optical, and IR contain complementary diagnostics that can probe the conditions within different nebular ionization zones.
- Accounting for complex density gradients and temperature profiles is critical for reliably estimating the fundamental properties of HII regions and galaxies.
- Diffuse ionized gas can raise metallicity estimates, flatten metallicity gradients, and introduce scatter in ionization parameter measurements.
- New 3D emission line diagnostics successfully separate the contributions from star formation, AGN, and shocks using integral field spectroscopy.

We summarize with a discussion of the challenges and major opportunities for emission line diagnostics in the coming years.

Contents

1. INTRODUCTION	512
1.1. Definitions	513
1.2. Theoretical Models	516
1.3. Nebular Structure	519
2. ISM PRESSURE AND ELECTRON DENSITY DIAGNOSTICS	523
3. THE IONIZATION PARAMETER IN GALAXY EVOLUTION STUDIES ...	526
3.1. Ultraviolet Ionization Parameter Diagnostics	528
3.2. Optical Ionization Parameter Diagnostics	530
3.3. Infrared Ionization Parameter Diagnostics	531
3.4. Mixed Line Ratio Diagnostics	531
4. METALLICITY IN GALAXY EVOLUTION STUDIES	532
4.1. Auroral Line Metallicities	533
4.2. Auroral-Strong Line Calibrations	535
4.3. Recombination Line Methods	538
4.4. Theoretical Metallicity Diagnostics	539
4.5. Theoretical Ultraviolet Metallicity Diagnostics	540
4.6. Theoretical Optical Metallicity Diagnostics	544
4.7. Theoretical Infrared Metallicity Diagnostics	546
5. EXCITATION SOURCES IN GALAXY EVOLUTION STUDIES	547
5.1. Excitation Sources Using Single-Aperture Spectroscopy	548
5.2. Excitation Sources Using Integral Field Spectroscopy	553
5.3. Excitation Source Modeling	554
6. DIFFUSE IONIZED GAS	556
7. CHALLENGES	557

1. INTRODUCTION

A galaxy spectrum contains a wealth of information on the fundamental physical processes occurring within the galaxy. A single optical spectrum alone can tell us the chemical abundance, the amount of dust, the electron density, the age of the stellar population, the pressure of the ISM, and the rate of star formation. The same spectrum can reveal whether there is an actively feeding supermassive black hole in the center of the galaxy or whether there are shocks from massive stellar winds or gas collisions due to mergers, jets, or other transformative processes. If an actively feeding supermassive black hole resides in the galaxy, the spectrum can tell us about the accretion rate, the shape of the AGN radiation field, and the strength of that radiation field. If the spectrum reveals shocks, the emission lines can be used to gauge the shock velocity, the density of the gas in the shock, and the mechanical energy of the shock. In this way, galaxy spectra allow us to understand the dominant power source of galaxies, the star-formation history of galaxies, the chemical history of galaxies, and the prevalence of galactic-scale winds in galaxies. Specific spectral features or combinations of features used to infer galaxy properties are called diagnostics. Diagnostics are calibrated either empirically or theoretically to allow estimates of fundamental galaxy properties.

MODELING GALAXY SPECTRA

To try to make a model of an atom by studying its spectrum is like trying to make a model of a grand piano by listening to the noise it makes when thrown downstairs.
—Anonymous

Therefore, making a model of a galaxy by studying its spectrum is like modeling an entire symphony orchestra from the noise it makes when falling downstairs. As we model galaxy spectra, it is crucial to understand the limitations of the models and the conditions where the models are invalid.

Our ability to model galaxy spectra has advanced rapidly over the past few decades. The first models were based on individual two- or three-level model atoms, which were applied to HII regions and planetary nebulae. The electron density and electron temperature were derived, with assumptions about the state and structure of the gas, including constant density and constant electron temperature. Fortunately, we no longer need to rely on simple atoms and assumptions to derive galaxy properties. Thanks to sophisticated quantum mechanical modeling and laboratory measurements, we now have large databases of atomic data, including atomic energy levels, collision and excitation rates, and collision cross sections, as well as data on the composition and effects of astronomical dust. At the same time, ground and space telescope observations have built enormous databases of stellar spectra while physics laboratories have advanced our understanding of the processes that produce spectra, including photoionization, collisional excitation, and shock physics. Now, galaxy spectral models include the latest atomic data and radiative transfer physics, including detailed dust processes, and shock processes. (See the sidebar titled Modeling Galaxy Spectra.)

Space-based IR telescopes and efficient high-resolution optical and IR spectrographs on the world's largest ground-based telescopes have recently unlocked the rest-frame IR and UV emission-line spectra of galaxies. With these new windows, we can now track the evolution of fundamental galaxy properties across 12 billion years of cosmic time to 1/10th the age of the Universe (i.e., to $z \sim 4$). In the coming decade, new larger space- and ground-based telescopes will reveal the first galaxies in the Universe, >13 billion years ago. Rest-frame UV emission lines will become critical for understanding the early phases of galaxy evolution while the full suite of UV, optical, and IR lines will be required to track the evolution of fundamental galaxy properties across cosmic time.

In this review, we focus on the emission lines in a galaxy spectrum from the UV to the IR. We do not cover the use of emission lines to measure star-formation rates (SFRs) or dust extinction because both topics have already been widely reviewed (see Kennicutt 1998; Calzetti et al. 2007, 2010; Calzetti 2013; da Cunha 2016). Here, we review and expand on the existing library of diagnostics for the electron density, ISM pressure, chemical abundance, and excitation source of galaxies. For this purpose, we use the latest pressure and density models from Kewley (2019), calculated by combining Starburst99 and MAPPINGS v5.1 photoionization models. In anticipation of upcoming telescope facilities, we use our new models to recalibrate some of the existing optical diagnostics, and for spectral regions where diagnostics are missing, we provide new diagnostics. These UV–optical–IR diagnostics can be used in concert to understand how fundamental galaxy properties have changed across cosmic time.

1.1. Definitions

Atomic and ionic energy levels can be populated and depopulated by collisions with electrons and, less frequently, by collisions with heavier particles such as protons. Here, we focus on electron

Electron density (n_e):

the number of electrons per unit volume in a nebula, in number of electrons per cubic centimeter

collisions and radiative processes, giving a brief mathematical description of this process. We refer the reader to Peimbert et al. (2017) for an excellent tutorial of the heating and cooling processes occurring in gaseous nebulae. A comprehensive overview of the physics of gaseous nebulae can be found in many existing papers and textbooks, including Strömgren (1939, 1948), Seaton (1960), Osterbrock (1989), Aller (1984), and Dopita et al. (2003).

For thermal electron energy distributions, the collisional excitation rate per unit volume, R_{ij}^{coll} ($\text{cm}^{-3} \text{ s}^{-1}$) from energy level i to energy level j is given by

$$R_{ij}^{\text{coll}} = n_e N_i \alpha_{ij}, \quad 1.$$

where n_e is the electron density per unit volume and N_i is the density of the ions with electrons in the lower level i . The collisional coefficient α_{ij} ($\text{cm}^3 \text{ s}^{-1}$) depends on the temperature, T , of the gas through an exponential thermal excitation term, $\exp(-E_{ij}/kT)$, and a power-law term, $T^{-1/2}$, by

$$\alpha_{ij} = k_{\text{coll}} \frac{\Omega_{ij}}{g_i} T^{-1/2} \exp\left(\frac{-E_{ij}}{kT}\right), \quad 2.$$

with $k_{\text{coll}} = [(2\pi\hbar^4)/(km_e^3)]^{1/2} \approx 8.63 \times 10^{-6}$. Here, Ω_{ij} is the collision strength for the transition from level i to level j , g_i is the statistical weight of level i , and E_{ij} is the energy difference between levels i and j . The relative importance of each of the two temperature terms governs whether a line ratio pair is sensitive to the electron density or pressure of the gas.

The upper energy level j can also be depopulated by collisional de-excitation by electrons. The collisional de-excitation rate, R_{ji}^{dex} , is given by

$$R_{ji}^{\text{dex}} = n_e N_j \beta_{ji}, \quad 3.$$

with

$$\beta_{ji} = k_{\text{coll}} \frac{\Omega_{ji}}{g_j} T^{-1/2}. \quad 4.$$

Here, Ω_{ji} is the collision strength for the transition from level j to level i , and g_j is the statistical weight of level j . The term β_{ji} is similar to α_{ij} , but does not contain an exponential thermal excitation term.

In the past, the collision strengths were approximated using methods by Seaton (1958), with a classical formula and a Gaunt factor correction $G(T)$:

$$\Omega_{ij} = \frac{8\pi}{\sqrt{3}} E_{ij}^{-1} \text{gf}_{ij} G(T). \quad 5.$$

For modern atomic data, the collision strengths are computed numerically from full quantum mechanical collision calculations. In either case, Ω_{ij} retains a dependence on temperature. This residual temperature dependence becomes important for the mid-IR fine structure lines.

Finally, the radiative depopulation rate of level j is given simply by A_{ji} , the spontaneous transition probability, and the density of ions with populations in level j . The radiative depopulation rate is independent of temperature:

$$R_{ji}^{\text{rad}} = N_j A_{ji}. \quad 6.$$

The electron density is often calculated using simple atom models, assuming a constant nebular density and temperature. The nebular pressure, P , is related to the nebula temperature, T , and

total particle density n through the ideal gas assumption $P = nkT$. Assuming that the nebular temperature and the ISM pressure are related, the ISM pressure can be approximated using the mean nebular temperature T_e :

$$P_{\text{ISM}} \approx nkT_e, \quad 7.$$

where the total density n is approximated from the electron density through $n \sim 2n_e(1 + \text{He}/\text{H})$. In a fully ionized plasma, the electron temperature is often assumed to be $\sim 10^4$ K, and P_{ISM} is assumed to be directly proportional to n_e .

A critical value in determining the state of the plasma in a nebula is the ionization parameter,

$$q = \Phi_{\text{H}^0}/n_{\text{H}}, \quad 8.$$

which is the ratio of the local ionizing photon flux Φ ($\text{cm}^{-2} \text{s}^{-1}$) and the local hydrogen density n_{H} (cm^{-3}). For a spherical geometry, the ionization parameter q_s at radius R can be defined to take into account the spherical divergence of radiation:

$$q = \frac{L_{\text{H}^0}}{4\pi R^2 n_{\text{H}}}, \quad 9.$$

where L_{H^0} is the ionizing photon luminosity (s^{-1}) above the Lyman limit. This dimensional ionization parameter is related to the dimensionless ionization parameter U by dividing by the speed of light (i.e., $U \equiv q/c$). The dimensionless ionization parameter is typically $-3.2 < \log U < -2.9$ for local HII regions (Dopita et al. 2000) and star-forming galaxies (Moustakas 2006, Moustakas et al. 2010). The ionization parameter q has units of velocity (cm s^{-1}) and, to first order, can be considered the velocity of the ionization front that an ionizing radiation field is able to drive into the surrounding neutral medium.

Different ionization parameter calibrations from different authors cannot be used interchangeably. Some calibrations use the ionization parameter at the inner edge of a plane parallel nebula [$U(R_{\text{in}})$] (Kewley & Dopita 2002, Kobulnicky & Kewley 2004, Levesque et al. 2010), whereas Stasińska et al. (2015) derive a volume-averaged ionization parameter, \bar{U} :

$$\bar{U} = \frac{\alpha_{\text{B}}^{2/3}}{c} \left(\frac{3}{4\pi} n_{\text{H}} \epsilon^2 L_{\text{H}^0} \right)^{1/3} \left[(1 + f_{\text{S}}^3)^{1/3} - f_{\text{S}} \right], \quad 10.$$

where α_{B} is the case B recombination coefficient, ϵ is the volume filling factor of the gas, and $f_{\text{S}} = R_{\text{in}}/R_{\text{S}}$ is the ratio of the model inner radius R_{in} to the Strömgren radius, where the Strömgren radius is calculated assuming $R_{\text{in}} = 0$. Jaskot & Ravindranath (2016) adopt $\alpha_{\text{B}} = 2.6 \times 10^{-13} \text{ cm}^3 \text{s}^{-1}$, the value for 10^4 K gas from Storey & Hummer (1995), to derive useful conversions for comparison among ionization parameter values in the literature. They relate \bar{U} to the ionization parameter at the Strömgren radius, $U(R_{\text{S}})$, and to the ionization parameter at the inner radius, $U(R_{\text{in}})$:

$$\bar{U} = 3U(R_{\text{S}}) \left[(1 + f_{\text{S}}^3)^{1/3} - f_{\text{S}} \right], \quad 11.$$

$$\bar{U} = 3U(R_{\text{in}}) f_{\text{S}}^2 \left[(1 + f_{\text{S}}^3)^{1/3} - f_{\text{S}} \right]. \quad 12.$$

The ionization parameter can be defined in other ways, depending on the models used and the application. In theoretical star cluster models, the ionization parameter represents the ratio of the ionizing radiation pressure to the gas pressure (Yeh & Matzner 2012). Most different ionization parameter calibrations are based on different geometries. In practice, if spherical or plane parallel models have the same ionization parameter (defined at the same distance in the nebula), they

ISM pressure
[log(P/k)]: the pressure within the HII region, which is generally at a higher pressure than the surrounding diffuse medium, in $\text{cm}^{-3} \text{K}$

produce very similar spectra, assuming all other parameters are held constant (e.g., Dopita et al. 2000).

The gas-phase metallicity strongly influences the emission from HII regions and galaxies. The gas-phase metallicity is usually calculated as the oxygen abundance relative to hydrogen and is defined in units of $\log(\text{O}/\text{H}) + 12$. Oxygen is used to define the overall gas-phase metallicity because oxygen is the dominant element by mass in the Universe and is readily observable in the optical spectrum using temperature-sensitive collisionally excited lines. These lines are sensitive to the oxygen abundance both through the amount of oxygen in the gas as well as through the electron temperature of the gas. The electron temperature is sensitive to the total gas-phase metal abundance (i.e., all the metals, not just oxygen) because metals act as coolants in a nebula. As the nebula cools, there are fewer collisional excitations and the strength of collisionally excited lines becomes anticorrelated with the gas-phase metallicity.

1.2. Theoretical Models

Current galaxy spectral models are based on the combination of stellar evolution synthesis simulations and photoionization models. These two components have evolved separately and are still used as stand-alone codes, depending on the application.

1.2.1. Stellar evolutionary synthesis models. The first stellar evolutionary synthesis models for galaxies were developed by Tinsley (1968), who calculated a large population of stars with continuous star formation in bins of stellar mass. She placed the stellar population on the Hertzsprung–Russell (HR) diagram and evolved the population according to evolutionary tracks. Stars of different mass evolve along different tracks, and the spectrum of an entire population can be calculated by stopping the tracks at a given age. By adjusting the rate of stellar births and the age of the stellar population, Tinsley’s models successfully reproduced the colors, mass-to-light ratios, relative gas masses, and types of galaxies.

Stellar evolutionary synthesis models developed substantially over the subsequent decades. Major advances include chemical evolution calculations and massive star evolution (Talbot & Arnett 1971, Truran & Cameron 1971), stellar and gas-phase abundances (Tinsley 1972), heavy element yields (Tinsley 1973), changing star-formation histories (Larson & Tinsley 1978), secondary nucleosynthesis (Arimoto & Yoshii 1986), nebular emission and internal extinction (Guiderdoni & Rocca-Volmerange 1987), and stellar mass loss (Alongi et al. 1993). New observational data sets have also been incorporated, including giant branch luminosity functions (Tinsley & Gunn 1976); the UV spectra of stars (Rocca-Volmerange et al. 1981, Bruzual 1983); stars in the horizontal, asymptotic giant, and post-asymptotic giant branches (pAGBs; Buzzoni 1989); near-IR stellar spectra (Bruzual & Charlot 1993); and stellar atmosphere opacities (Bressan et al. 1993). Modern stellar evolution synthesis models are still based on Tinsley’s method, but they now use isochrone synthesis, in which isochrones are fitted to the evolutionary tracks across different masses rather than discretely assigning stellar mass bins to specific tracks (e.g., Charlot & Bruzual 1991).

In the mid-1990s, stellar evolution synthesis codes diverged into two types: fixed metallicity and chemical evolution. Many different stellar evolutionary synthesis models now exist, and each code has its advantages and disadvantages. Fixed metallicity stellar evolution models include sophisticated treatment of stellar processes such as stellar rotation, mixing, metal opacities, and massive-star evolution (Leitherer et al. 1999). Some models provide high spectral resolution for modeling the contribution from stellar atmospheres and winds to blended UV lines (Vazdekis et al. 2016). The chemical evolution spectral synthesis models include the evolution of the

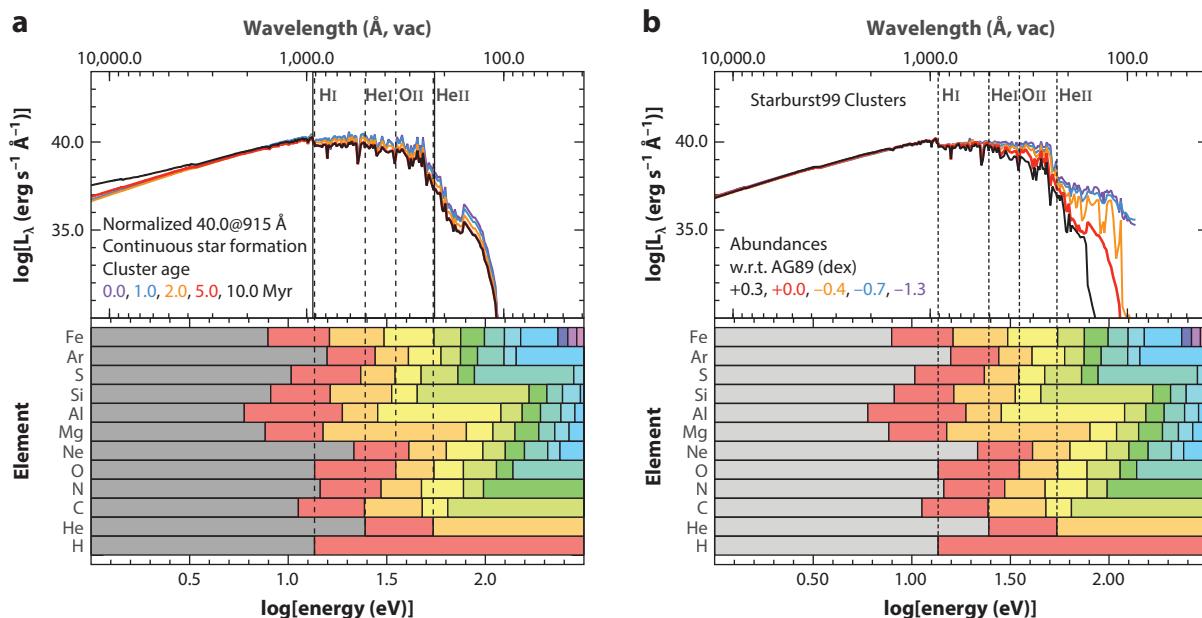


Figure 1

(a) The spectral energy distribution for Starburst99 simulations of star clusters with ages of 0–10 Myr. (b) The spectral energy distribution for Starburst99 simulations of star clusters for metallicities scaled with respect to Anders & Grevesse (1989) with log scaling factors of +0.3, 0.0, −0.4, −0.7, and −1.3 [i.e., $\log(\text{O}/\text{H}) + 12 = 9.23, 8.93, 8.53, 8.23$, and 7.63]. In both panels, the ionization potentials of four key elements (H I, He I, O II, and He II) are shown as vertical dashed lines, and the ionization potentials of 12 selected elements are shown in the lower halves of the panels for comparison.

stellar and gas-phase metallicities over cosmic time (Bressan et al. 1994, Kotulla et al. 2009, Fioc et al. 2011). Models now include extinction and gas physics (Fioc et al. 2011), and dust absorption and reemission (Piovan et al. 2006).

Many stellar evolutionary synthesis models are now available. Starburst99 includes detailed models for massive stars, including metal opacities, and is useful for modeling the global emission from starburst galaxies (Leitherer et al. 1999). The SLUG (Stochastically Lighting Up Galaxies) code treats stellar populations stochastically and is particularly useful for modeling H II regions and star-forming dwarf galaxies (Krumholz et al. 2015). The PÉGASE (Projet d’Étude des GALaxies par Synthèse Évolutive) code includes detailed chemical evolution of the stellar population, with less emphasis on modeling massive stars or their atmospheres (Fioc et al. 2011), whereas PÉGASE-HR is a high-resolution version of PÉGASE and provides reliable fits to the continua of quiescent galaxies. The latest version of GALAXEV (Bruzual & Charlot 2011) includes new stellar tracks and treatment of the extreme UV (EUV) ionizing radiation field, as well as new thermally pulsing asymptotic giant branch star models based on observations in the Large Magellanic Cloud and Small Magellanic Cloud [see Gutkin et al. (2016) for a description]. Schaerer (2013) and Conroy (2013) give useful overviews of the full range of stellar evolution synthesis models available.

The shape of the ionizing radiation field produced by stellar evolution models depends on the age of the stellar population and on the metallicity. Certain diagnostics will therefore be very sensitive to, for example, the presence of Wolf–Rayet (WR) stars or other features of the EUV radiation field. **Figure 1a** shows how the shape of the ionizing radiation field changes for a continuously forming cluster as the stellar population ages from 0 Myr to 6 Myr, normalized at 915 Å. The ionization potentials of key atomic elements are given in the lower half of the panels for comparison.

The number of ionizing photons in the spectrum at the ionization potential of each atomic species will determine the ionization structure of the nebula. **Figure 1** shows that the change in age from 0 to 5 Myr causes a larger change in He^+ ionizations than O^+ ionizations owing to the different ionization potentials of He^+ and O^+ .

The metallicity also strongly affects the shape of the EUV radiation field, as shown in **Figure 1b**. The EUV radiation field emitted by star clusters is harder in low metallicity environments because (a) there are fewer metals in the stellar atmosphere to absorb the stellar radiation field, (b) massive stars at low metallicity have hotter effective temperatures, and (c) the main sequence lifetimes are longer at low metallicity because of lower mass-loss rates [see Levesque et al. (2010) for a discussion]. The effect of WR stars is also larger at high metallicities because WR winds are stronger and have longer lifetimes in metal-rich environments, and a smaller mass is required to reach the WR stage. In general, species with ionization potentials >1.5 eV are strongly affected by the metallicity of the EUV radiation field. Therefore, prior to applying an emission-line diagnostic, it is important to check the shape of the ionizing radiation field relative to the ionization potential of the emission lines of interest in order to understand how uncertain the EUV radiation field is at those wavelengths and to understand its sensitivity to age and metallicity.

1.2.2. Photoionization models. The physical conditions in photoionized regions are so complex that analytical solutions are impossible. Instead, we must rely on photoionization models. Early photoionization models were based on the observations by Struve & Elvey (1938), who showed that the gas around young O and B stars contains $\text{H}\alpha$ and $[\text{OII}] \lambda 3727$ emission. These observations inspired Strömgren (1939) to create the first model of these regions based on spheres of gas. A modified version of the Strömgren sphere is still used today to model HII regions.

Major advances in photoionization modeling of HII regions were made in the 1950s and 1960s. Zanstra (1951) showed that the ionization state of the gas can be calculated if the gas is optically thick to the incident radiation field. This assumption, known as the “on-the-spot” approximation, means that recombination of ions with electrons to the ground state produces diffuse radiation that immediately causes reionization of the neutral gas. Williams (1967) considered the ionization and thermal balance within the gas surrounding a diffuse ionizing radiation field, and Rubin (1968) modeled an HII region in thermal and ionization equilibrium with an arbitrary density distribution.

AGN photoionization models were developed separately. Early calculations of temperatures and densities in AGNs focused on quasi-stellar objects (QSOs) (Osterbrock & Parker 1966, Mathesz 1969), including stratified models in which distinct zones contain ions at different stages of ionization (Burbidge et al. 1966; Bahcall & Kozlovsky 1969a,b). Optically thin and optically thick X-ray nebulae were considered (Tarter & Salpeter 1969, Tarter et al. 1969), and the physics of Auger ionization, Compton heating, and charge transfer collisions were subsequently included (Hatchett et al. 1976, Halpern & Grindlay 1980). Davidson (1972) calculated iterative photoionization models in which the gas has a central QSO ionizing source and spherical symmetry. High-temperature shocks were suggested as a possible cause of the forbidden lines of QSO and Seyfert galaxies (MacAlpine 1974), whereas Shields (1974) showed that a power-law radiation field can explain the emission from the radio-loud Seyfert 1 galaxy 3C 120. Resonance line-trapping and collisional de-excitation can affect the emission-line spectrum in the high gas densities associated with nebulae around QSOs, and these were included in subsequent models (Krolik & McKee 1978, Ferland & Netzer 1979, Kallman & McCray 1982).

Over the past three decades, two large self-consistent photoionization codes emerged that include the physical developments discussed above: MAPPINGS (Binette et al. 1985; Sutherland & Dopita 1993, 2017) and CLOUDY (Ferland et al. 1998, 2017). MAPPINGS includes self-consistent

treatment of nebular, dust, and shock physics and can be applied to HII regions, AGNs, and regions shocked by supernovae, galactic winds, and jets. CLOUDY includes self-consistent treatment of nebular, dust, and molecular physics and can be applied to HII regions, AGNs, and photodissociation regions (PDRs). These photoionization models were originally used as stand-alone codes with blackbody and power-law radiation fields to simulate regions excited by star formation and AGNs, respectively. It is now known that a blackbody does not provide an accurate representation of the ionizing radiation field from a star-forming region because the stellar radiation field is transported through the stellar atmosphere. The helium and metals in the photosphere systematically absorb radiation from the star (known as line blanketing), significantly altering the spectral shape (Pauldrach et al. 2001). Stellar mass loss and rotation, and the effect of binary stars, can also alter the shape of the ionizing radiation field (Kurucz 1979; Pauldrach et al. 1986, 2012; Schmutz et al. 1989; Leitherer 2008; de Mink et al. 2009; Eldridge & Stanway 2012; Levesque et al. 2012).

More sophisticated techniques developed in the early 2000s. Stellar evolutionary synthesis and photoionization models were combined to analyze the optical spectra of HII regions (Dopita et al. 2000) and star-forming galaxies (Kewley et al. 2001a, Moy et al. 2001). More realistic AGN ionizing radiation fields were included in photoionization models to understand the properties of AGN spectra (Groves et al. 2004a,b; Thomas et al. 2016). Ideally, the stellar continuum and nebular gas are coupled self-consistently to produce line intensities that scale with the stellar population in terms of age and metallicity (see Byler et al. 2017).

1.3. Nebular Structure

Theoretical models assume an ionization structure, temperature structure, and density structure of the nebula. It is important to assess whether particular diagnostics will be applicable to HII regions or a galaxy of interest by comparing the observed ionization, temperature, and density structure with the theoretical models that are used to interpret the diagnostic line ratios.

1.3.1. Ionization structure. Ionization lines of different species probe different zones of a nebula because they have different ionization potentials and different critical densities. The X-ray spectrum (10–0.1 Å) and the EUV spectrum (4,000–10 Å) cover up to 31 ionization stages.¹ **Figure 2** gives the MAPPINGS v5.1 ionization zones for selected strong emission lines. Only a few sets of lines are produced throughout the nebula. The [OIII] and CIII] lines are both produced throughout the nebula, and derived properties may be considered as broadly representative of the overall ISM within the nebula. The [NII] and [OII] lines trace similar regions of the nebula and may be used to trace intermediate-zone pressures and metallicities. Higher-ionization species, such as [NeIV], [OV], [ArIV], [NIV], and [SV], trace regions of high ionization, close to the ionizing source. However, the [SII], [OI], and [NI] lines trace the very outer edge of the nebula, where the gas is only partially ionized.

Both MAPPINGS and CLOUDY assume plane parallel or spherical symmetry and cannot produce specific ionization structures that are seen in the Milky Way, such as the ionization bar in the Orion Nebula (e.g., Simpson et al. 1986, Rubin et al. 2011), but they can produce an overall equivalent spherical ionization structure (**Figure 3**) that reproduces the observed spectrum.

1.3.2. Temperature structure. Optical density-sensitive line ratios have traditionally been calibrated assuming a simple model atom and a single electron temperature (typically $T_e = 10^4$ K)

Critical density

(n_{crit}): the density where the collisional de-excitation probability equals the radiative de-excitation probability for the excited state, in cm s^{-1}

¹The National Institute of Standards and Technology (NIST) database gives the ionization potential of the elements (Kramida et al. 2018).

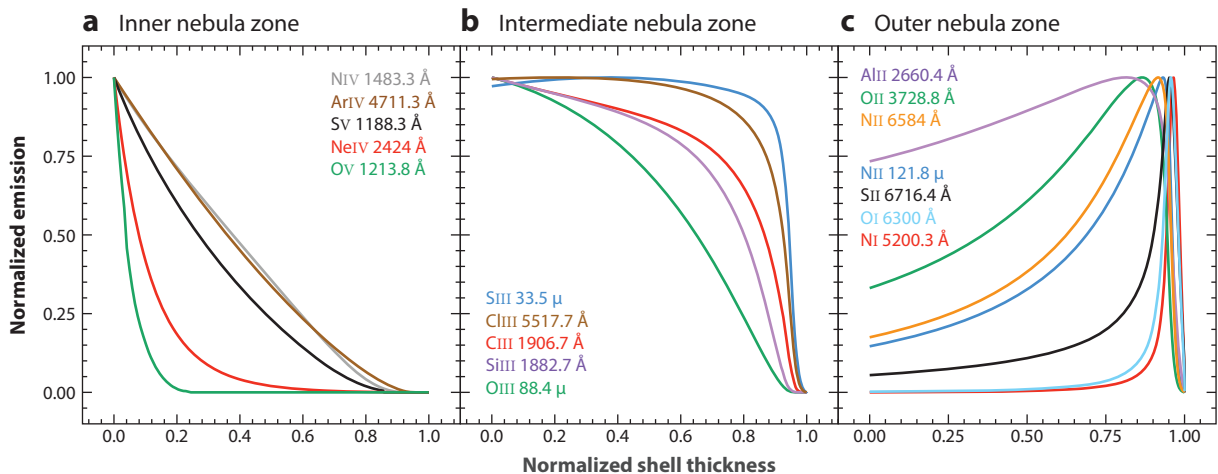


Figure 2

The ionization zones for selected strong emission lines in the UV, optical, and IR spectral regions. The panels correspond to emission lines produced in the (a) inner, (b) intermediate, and (c) outer zones of the nebula.

(e.g., Osterbrock 1989, Rubin et al. 1994). Single-temperature models have also been assumed in AGN and starburst photoionization models for determining the power source of galaxies (e.g., Filippenko 1985, Hill et al. 1999, Groves et al. 2004).

In current photoionization models, the electron temperature varies as a function of distance from the ionizing source. **Figure 4a** shows how the electron temperature varies through a theoretical nebula. The electron temperature can only be approximated by isothermal conditions for

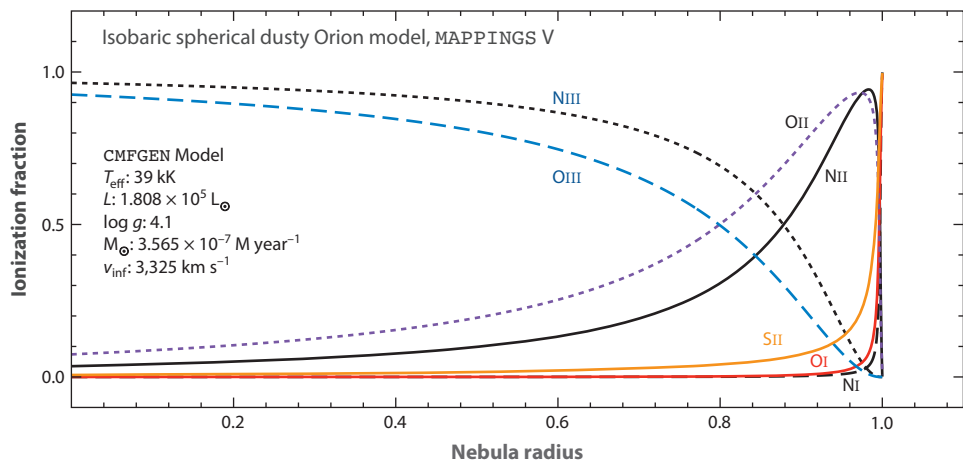


Figure 3

Spherical MAPPINGS v5.1 model of the ionization structure in Orion for isobaric conditions. Model parameters for the dominant central star Theta 1C are shown. Colored curves correspond to the ionization fractions of commonly observed emission lines of oxygen, sulfur, and nitrogen. These models use stellar population synthesis models from the stellar atmosphere code CMFGEN, where CMFGEN is the stellar modeling code from Hillier (2012), L is the luminosity, L_{\odot} is the luminosity expressed in solar luminosities, \dot{M}_{\odot} is the mass-loss rate in solar masses per year, and v_{inf} is a function of the escape velocity.

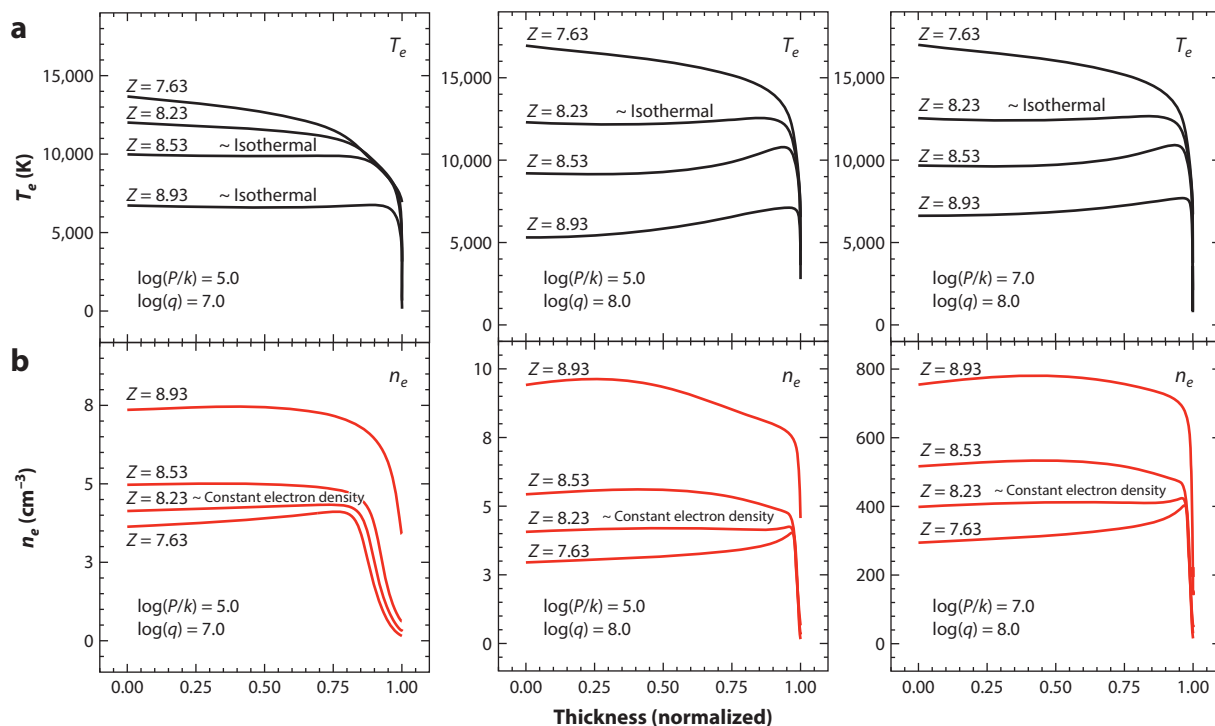


Figure 4

(a) The electron temperature and (b) electron density as a function of normalized model thickness for our MAPPINGS V pressure models with $\log(P/k) = 5.0$, $\log(q) = 7.0$ (left), $\log(P/k) = 5.0$, $\log(q) = 8.0$ (middle), and $\log(P/k) = 7.0$, $\log(q) = 8.0$ (right). Figure adapted from Kewley (2019).

some metallicities. At metallicities at or above $\log(\text{O}/\text{H}) + 12 \sim 8.5$, the nebula becomes hotter toward the outer edges because the soft ionizing photons have already been absorbed by metals closer to the ionizing source; this leaves predominantly hard ionizing photons, yielding more heat per ionization. In addition, the dominant coolant, $[\text{OIII}]$, dominates the cooling in the inner nebula zone, but it is not a significant coolant in the outer nebula.

The electron temperature structure in HII regions has been notoriously difficult to measure due to the weakness of the emission lines most sensitive to T_e (e.g., Luridiana & Cerviño 2003). Integral field spectroscopic studies of local HII regions have now made such measurements possible in just a few cases [see, e.g., Wang et al. (2004) for a discussion]. However, detailed observations have been made of the temperature structure across θ^1 Ori C in the Orion Nebula, shown in **Figure 5a**. The electron temperature in the $[\text{NII}]$ and $[\text{OIII}]$ zones is complex and varies across θ^1 Ori C, rising with distance from the ionizing source; this is similar to the predictions of the theoretical photoionization models with $\log(\text{O}/\text{H}) + 12 > 8.53$ and $\log(q) = 8$.

Assuming a constant temperature becomes particularly problematic when fixed-size apertures capture the light from an ensemble of HII regions, as is the case for global spectra of high-redshift galaxies. Fiber-based or slit-based spectra of nearby or distant galaxies represent the luminosity-weighted average of multiple (up to hundreds or thousands of) HII regions, each of which may contain a complex electron temperature structure. In addition, diffuse ionized gas (DIG) can contribute to electron temperature gradients and contaminate the emission lines observed in fixed-size apertures (Otte et al. 2002). Therefore, the spectra from an ensemble of HII regions cannot be

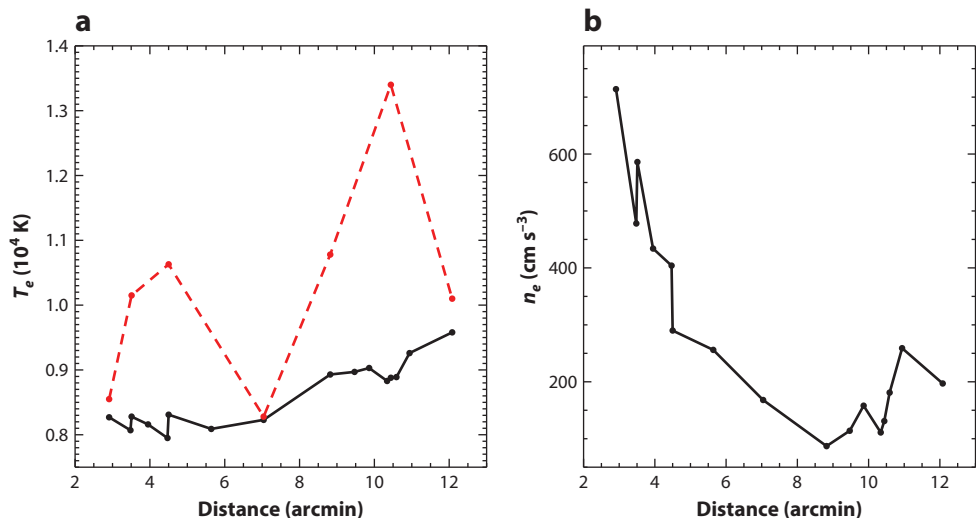


Figure 5

(a) The electron temperature and (b) electron density as a function of distance from the center (in arcmin) of the Orion nebula. The electron temperature is measured using the auroral [N II] $\lambda 5755$ (black solid line) and [O III] $\lambda 4363$ (red dashed line) emission lines. The electron density is measured using the [S II] $\lambda\lambda 6717, 31$ doublet. Data taken from Rubin et al. (2011).

robustly modeled using a constant temperature model. Models that allow a complex temperature structure or gradient will provide more realistic results.

1.3.3. Density structure. Current measurements of the electron density of H II regions and galaxies are based on single-atom models that assume a constant density across the H II regions. However, we know that this is not a realistic assumption. Ionized gas and radio continuum density measurements reveal complex radial gradients in many H II regions (Franco et al. 2000, Pérez et al. 2001, Binette et al. 2002, Luridiana & Cerviño 2003, McLeod et al. 2016) and flat gradients in others (García-Benito et al. 2010, Ramos-Larios et al. 2010). These density gradients are often anticorrelated with H II region size. Ultracompact H II regions typically have steep density gradients (de Pree et al. 1995, Franco et al. 2000, Kurtz 2002, Johnson & Kobulnicky 2003, Phillips 2007), whereas larger H II regions have more shallow or flat density gradients (Phillips 2008).

The Milky Way H II region density structure has been studied extensively in the IR. Simpson et al. (2004) found significant density variations of $40\text{--}4,000\text{ cm}^{-3}$ within a single H II region in the inner region of the Milky Way, whereas Rubin et al. (2011) found complex electron density structure in the Orion nebula with density variations of $80\text{--}700\text{ cm}^{-3}$. In **Figure 5b**, we show the density structure of Orion with measurements from Rubin et al. (2011) along θ^1 Ori C. The electron density is not a simple gradient from the ionizing source and is likely the result of a blister H II region and contamination by scattered light from a nearby, more dense region.

Photoionization models in pressure equilibrium calculate the electron density structure of the nebula based on the ionizing radiation field. **Figure 4b** shows how the electron density varies through a theoretical nebula for differing pressure, ionization parameters, and metallicity. At high metallicity, electron density gradients are seen, and at low metallicity, a more complex structure is seen, due to the relationship between electron density and ionization parameter, which is large at the outer edges of the nebula at low metallicity.

There are many potential causes for complex density structures. HII regions can trigger the formation of new stars through “collect and collapse” (Elmegreen et al. 1995) and “radiation driven implosion” (Bertoldi 1989). In the collect and collapse model, the HII region expands into a supersonically turbulent cloud, causing coagulation of gravitationally unstable clumps that can collapse and form new stars. In the radiation driven implosion model, hot stars penetrate the ISM and heat the cold low-density gas. The heating amplifies overdensities created by the turbulent ISM, which then collapse and form stars (Gritschneider et al. 2009, Dale et al. 2012). Both processes can create globules of dense gas (e.g., Tremblin et al. 2013, Walch et al. 2015, Schneider et al. 2016). Unusual geometries can also be created by stellar wind-driven outflows, creating horseshoe or other complex geometries (Park et al. 2010).

Galaxies too have complex density structure and gradients. Star-forming galaxies typically have electron densities that follow a $r^{-1/2}$ profile out to ~ 10 kpc (Gutiérrez & Beckman 2010). The electron density can also exhibit structure and is large at the edges of bars where gas collisions occur (Herrera-Camus et al. 2016), as well as in some extended regions associated with galactic-scale winds (Ho et al. 2014, Rose et al. 2018). Seyfert galaxies exhibit electron density gradients (Kakkad et al. 2018). In particular, in Seyfert galaxies the gas density (a) increases with the ionization potential of the ions, and (b) is anticorrelated with the electron temperature (Spinoglio et al. 2015).

Emission lines produced by different ions and different energy levels are sensitive to different density regimes, depending on the critical density of the transition. Lines with low critical densities, like [OII] and [SII], are affected by collisional de-excitation and are therefore weak in the high-density regions, whereas [ClII] and [ArIV] trace higher-density regions of a nebula. Likewise, the [OIII] fine structure lines have a significantly lower critical density than the [ArIV] or the [ClII] lines and, therefore, trace lower-density regions than the [ArIV] or [ClII] lines. The high-ionization line ratios like [ArIV] and [ClII] therefore trace the ISM pressure conditions within a luminosity-weighted average of the high-density clumps.

Where density gradients or clumpiness is expected, we recommend the use of models that include complex density gradients and profiles, such as models that assume pressure equilibrium. If constant density diagnostics are applied to HII regions or galaxies that contain density gradients or clumps, the properties derived will likely be dominated by the regions that produce the largest emission-line strengths and will not necessarily represent the galaxy average.

2. ISM PRESSURE AND ELECTRON DENSITY DIAGNOSTICS

Electron density diagnostics are based on UV, optical, or IR emission-line ratios of the same species. The first calibrations were developed for diagnosing the electron density in planetary nebulae using UV or optical spectroscopy (e.g., Aller 1961, Dopita et al. 1976, Stanghellini & Kaler 1989, Keenan et al. 1992, Copetti & Writzl 2002). Optical and UV density-sensitive line ratios were subsequently calibrated for HII regions (Esteban et al. 1999, Wang et al. 2004, Park et al. 2010) using simple model atoms. UV line ratios have also been used to derive the electron density in the gas around quasars (Nussbaumer & Schild 1979, Negrete et al. 2012). The IR fine structure lines were first used to measure the electron density in planetary nebulae over a decade ago (e.g., Liu et al. 2001), and they are now accessible as density diagnostics in local HII regions and galaxies as well as at high redshift (e.g., Maiolino et al. 2005, 2009; Ferkinhoff et al. 2010; Ivison et al. 2010; Valtchanov et al. 2011; Spinoglio et al. 2015).

Direct measurements of the electron density using the same methods are now being made for increasing numbers of galaxies, particularly at high redshift. Some studies find larger electron densities (Brinchmann et al. 2008, Hainline et al. 2009, Bian et al. 2010, Shirazi et al. 2013) on

average than in local galaxies, whereas others find similar electron densities to local galaxies (see Rigby et al. 2011, Bayliss et al. 2014). However, these large electron densities may be a selection effect. Kaasinen et al. (2017) matched high- z and local galaxies in stellar mass, SFR, and specific SFR. They showed that larger electron densities in high- z galaxies seen in previous work disappear when the samples are matched in SFR, implying that the observed large electron densities are a result of selecting samples of the most luminous galaxies at a given epoch.

Many electron density estimates assume a single-atom model with a constant electron temperature through the nebula. As discussed in Section 1.3.2, constant temperature is not a realistic assumption for most HII regions and galaxies. Full photoionization model grids with complex temperature structures have been developed to derive more realistic electron density estimates. Proxauf et al. (2014) use CLOUDY models to calibrate the [ArIII], [ArIV], [SII], and [OII] line ratios. Kewley (2019) uses photoionization models to calculate a suite of 13 density calibrations for various line ratios from the UV-FIR (far-IR), with minor corrections for metallicity and ionization parameter.

All electron density estimates assume that the electron density is constant across the HII region or galaxy. A constant density is not a valid assumption for many HII regions and galaxies. For these cases, the ISM pressure is a more realistic physical parameter to derive from most HII regions or ensembles of HII regions. The ISM pressure is a critical parameter in fully self-consistent models that include detailed nebular temperature and density structures. The pressure is determined by the combination of the mechanical energy produced by the stellar population as well as the strength and shape of the radiation field. Models with a constant pressure are appropriate when the sound-crossing time is less than the heating and cooling timescales, which occurs in the majority of HII regions (Field 1965, Begelman 1990). Gutiérrez & Beckman (2010) showed observationally that, to a first approximation, the HII regions can usually be considered as in pressure equilibrium with their surroundings.

Many pressure diagnostics depend strongly on the gas-phase metallicity. Different metallicity calibrations exhibit extremely large systematic discrepancies (up to 1 dex in $\log(\text{O}/\text{H}) + 12$) [see Kewley & Ellison (2008) for a review and discussion]. Due to these discrepancies, theoretical ISM pressure calibrations can only be used with metallicity calibrations that have been constructed using consistent theoretical models. For the pressure calibrations summarized here, many suitable consistent metallicity calibrations exist, from simple fits to MAPPINGS photoionization models given here, to the more sophisticated Bayesian methods of Blanc et al. (2015) and Thomas et al. (2018a) that simultaneously calculate the ionization parameter and metallicity probability distributions given the observed emission lines in a spectrum.

The UV contains several pressure and density sensitive emission-line ratios, which are described in detail by Kewley (2019). Some of these ratios, like the [SiII] $\lambda 1883$ /[SiII] $\lambda 1892$, [CII] $\lambda 1907$ /[CII] $\lambda 1909$, and [AlII] $\lambda 2660$ /[AlII] $\lambda 2669$ ratios, have been previously calibrated and successfully applied to planetary nebulae, to the gas around quasars, and to nearby HII regions (e.g., Nussbaumer & Schild 1979, Dufton et al. 1984, Clegg et al. 1987, Keenan et al. 1992, Negrete et al. 2012).

Figure 6a shows the relationship between the UV pressure-sensitive ratios, ISM pressure and electron density, as a function of metallicity. Calibrations of these diagnostics in terms of metallicity, as well as a minor secondary dependence on ionization parameter, are presented by Kewley (2019). The strong [SiII]/[SiII] and [CII]/[CII] ratios offer the most promise as UV electron density and pressure diagnostics for star-forming galaxies. The wavelengths in each of these ratios are sufficiently close that flux calibration and extinction correction are not necessary. The metallicity dependence of these ratios arises from the sensitivity of the C^{++} and S^{++} transitions to the electron temperature of the gas through their recombination coefficients. Both ratios are

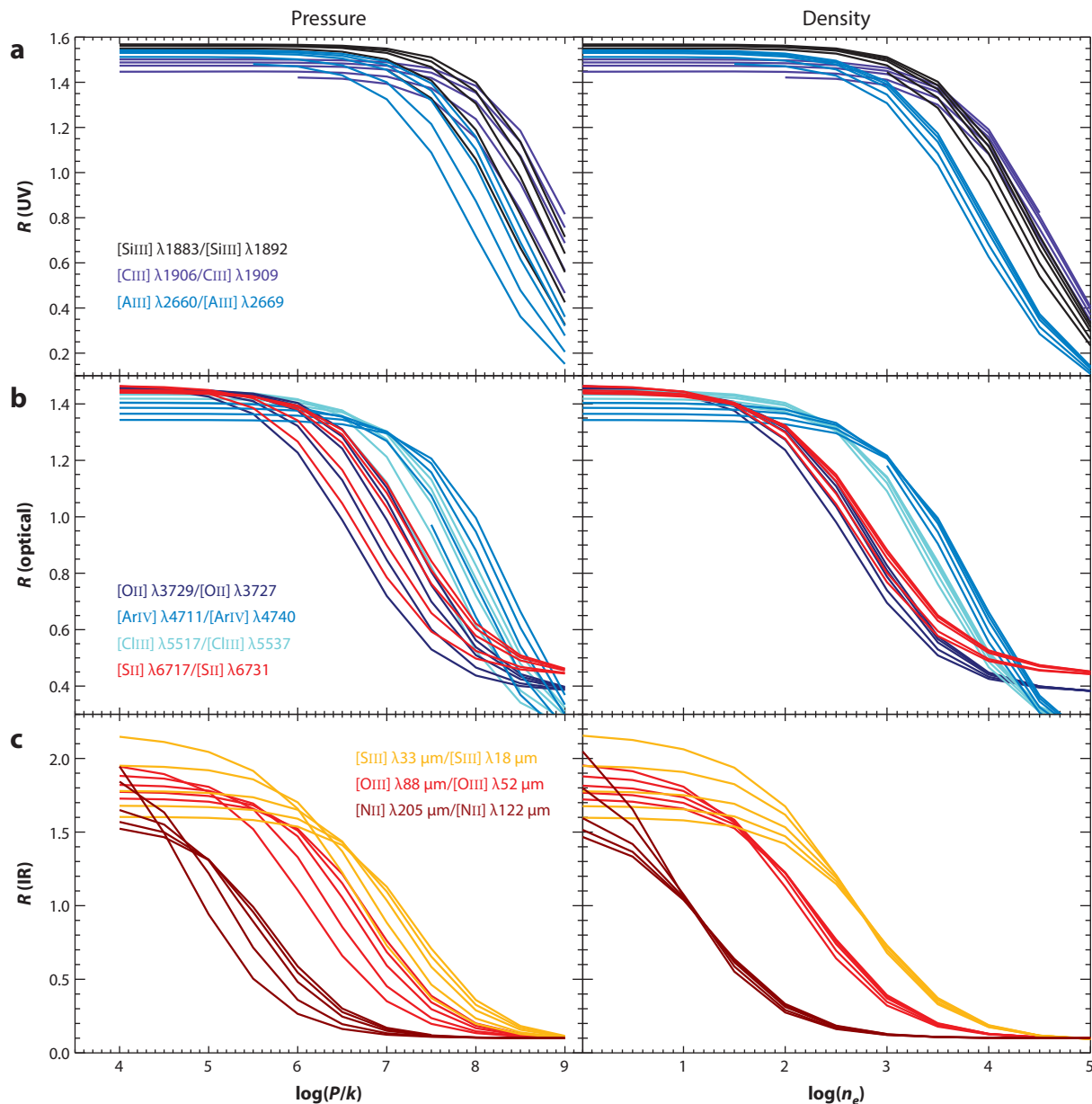


Figure 6

(a) UV, (b) optical, and (c) IR pressure and density diagnostics from Kewley (2019). For each ratio, models of constant metallicity are shown as lines from left to right corresponding to $\log(\text{O}/\text{H}) + 12 = [7.63, 8.23, 8.53, 8.93, \text{and } 9.23]$.

important tracers of dense environments [$\log(\frac{n_e}{\text{cm}^{-3}}) > 3.5$] and high pressures [$\log(\frac{P/k}{\text{cm}^{-3}\text{K}}) > 7$]. Both ratios have a residual dependence on temperature when used as a density diagnostic; temperature variations in the nebula may cause a scatter in the measured density of up to 0.3 dex.

High-ionization lines of neon and nitrogen can also be used as pressure and density diagnostics in the UV, but these ratios are weak in galaxies with high metallicity and low-ionization

parameter because the low-temperature and low-ionization parameter prevent ionization and collisional excitation of neon and nitrogen to their higher states. Care must be taken when using these two sets of lines because they may contain significant contributions from AGNs or shocked gas.

The optical contains many emission lines that together make density-sensitive line ratios, including the commonly used $[\text{OII}] \lambda 3729/[\text{OII}] \lambda 3726$ and $[\text{SII}] \lambda 6731/[\text{SII}] \lambda 6717$ ratios (**Figure 6b**). These calibrations have been used for decades to diagnose the electron density in planetary nebulae, HII regions, and galaxies (see, e.g., Osterbrock 1989, Kaasinen et al. 2017, and references therein). Weaker density-sensitive ratios such as the $[\text{ArIV}] \lambda 4711/[\text{ArIV}] \lambda 4740$, $[\text{NI}] \lambda 5198/[\text{NI}] \lambda 5200$, and $[\text{ClIII}] \lambda 5517/[\text{ClIII}] \lambda 5537$ ratios have been applied to planetary nebulae and local HII regions (e.g., Aller et al. 1970, Esteban et al. 1999, Lee & Hyung 2013). The CIII ratio traces high-density, high-pressure regions of the gas and is less sensitive to metallicity than the other diagnostics. The $[\text{ArIV}]$ and $[\text{NI}]$ lines are weak for metallicities and ionization parameters of most star-forming galaxies, and the $[\text{NI}]$ ratio depends strongly on metallicity above $\log(\text{O}/\text{H}) + 12 > 8.5$. This behavior is primarily caused by collisional effects between the upper levels in the pair, as well as transitions from higher levels [see Kewley (2019) for a full explanation].

The IR contains three extremely useful electron density diagnostics; the $[\text{SiII}] 33 \mu\text{m}/[\text{SiII}] 18 \mu\text{m}$, $[\text{OIII}] 52 \mu\text{m}/[\text{OIII}] 88 \mu\text{m}$, and $[\text{NII}] 205 \mu\text{m}/[\text{NII}] 122 \mu\text{m}$ ratios (**Figure 6b,c**). These ratios cover a broad range of densities, providing a complementary suite of diagnostics that can be used to build a comprehensive picture of the density structure of the ionized gas at a given redshift. These line ratios depend strongly on the metallicity, with a secondary dependence on ionization parameter.

The ionization parameter dependence of the pressure-sensitive line ratios is shown in figures 5–17 of Kewley (2019). To derive accurate ISM pressures, we recommend the interpolation of the theoretical model data given by Kewley (2019) with an estimated ionization parameter and metallicity.

3. THE IONIZATION PARAMETER IN GALAXY EVOLUTION STUDIES

The ionization parameter across normal star-forming galaxies is remarkably uniform. The dimensionless ionization parameter is typically $-3.2 < \log U < -2.9$ for local HII regions and star-forming galaxies (Dopita et al. 2000, Moustakas et al. 2010, Poetrodjojo et al. 2018). The largest ionization parameters in the local Universe are found in the largest star clusters, called super star clusters. The super star clusters in M82 have ionization parameters up to $\log(U) \sim -2.3$ (Förster Schreiber et al. 2001, Smith et al. 2006). Super star clusters in luminous IR galaxies have similar ionization parameters (Snijders et al. 2007, Indebetouw et al. 2009). Ionization parameters have not been observed above $\log(U) \sim -2.3$, suggesting that some mechanism or mechanisms moderate or limit the ionization parameter. Multiple mechanisms have been proposed, including expanding wind bubbles, radiation pressure confinement, and the effects of dust [see Yeh & Matzner (2012) for an excellent overview].

The global ionization parameter in galaxies is usually anticorrelated with the gas-phase metallicity, such that low-metallicity galaxies or HII regions have large ionization parameters (Dopita & Evans 1986). Bresolin et al. (1999) found that the ionization parameter in metal-poor disc HII regions is $\sim 4\times$ that in HII regions with solar metallicity. Similar results were reported by Maier et al. (2006) and Nagao et al. (2006). The cause of this anticorrelation between ionization parameter and metallicity is unknown. Dopita et al. (2006) proposed that the anticorrelation is caused by stellar atmospheres. At high metallicity, the stellar wind has a larger metal opacity and absorbs a larger fraction of the ionizing photons, leaving fewer EUV photons to ionize the surrounding HII region. Metal-rich stellar atmospheres also scatter photons from the photosphere more efficiently

than metal-poor atmospheres. This process allows luminous energy to be converted to mechanical energy more efficiently in the stellar wind region, reducing the number of ionizing photons incident on the HII region. Intriguingly, the metallicity–ionization parameter relation does not necessarily hold for spatially resolved data. In samples of HII regions within single galaxies, the ionization parameter generally does not correlate with metallicity (Garnett et al. 1997, Dors & Copetti 2005, Dors et al. 2011, Poetrodjojo et al. 2018).

The ionization parameter, measured directly using the [OIII]/[OII] lines, was larger in the past than today (Kaasinen et al. 2017). Over the past 6 billion years (from $z = 0$ to $z = 0.4$), the ionization parameter continued to fall by 0.1–0.25 dex, independent of metallicity and stellar mass (Kewley et al. 2015). This change is likely to be related to the fraction of young stars per unit volume, referred to as the cosmic star-formation density (Hirschmann et al. 2017).

Despite the importance of the ionization parameter in understanding the properties of ionizing sources and their influence on the surrounding ISM, very few ionization parameter calibrations existed until recently. The ionization parameter is typically measured by comparing two emission lines from the same atomic species that are in different ionization states. Many different species can be used to calculate the ionization parameter including carbon, sulfur, silicon, neon, nitrogen, and oxygen. The most sensitive ionization parameter diagnostics usually come from two states with the largest difference in ionization potentials. However, the ionization parameter can also be calculated using ionization-sensitive line ratios of different species.

Most high-ionization to low-ionization sets of lines are separated far in wavelength, requiring accurate flux calibration and extinction correction. Accurate flux calibration and/or extinction correction can be difficult at high redshift when ionization-sensitive emission lines are detected in different wavebands or when instrument flexure is severe. To overcome this issue, Kobulnicky & Phillips (2003) proposed using emission-line equivalent widths in lieu of fluxes. This method assumes that the continuum between the two ionization state lines is roughly constant between the wavelengths of interest. Tests indicate that this assumption holds for the rest-frame blue continuum between the [OII] $\lambda\lambda 3726, 9$ and [OIII] $\lambda\lambda 4959, 5007$ lines (Liang et al. 2007). However, we do not recommend the use of equivalent widths for UV ionization parameter diagnostics due to the strong underlying stellar UV continuum.

Below, we describe and provide new ionization parameter diagnostics from the UV through the IR. In **Table 1**, we provide bicubic surface fits to the ionization parameter in terms of $\log(R)$ and metallicity for $\log(P/k) = 5.0$ and $\log(P/k) = 7.0$, where R is the diagnostic line ratio. If the metallicity is unknown, our pressure diagnostics may be used with a metallicity estimated using the mass–metallicity (MZ) relation, or by assuming a metallicity of $\log(\text{O}/\text{H}) + 12 \sim 8.7$, and accounting for the potential difference between this assumed metallicity and the potential metallicity. Note that for the bicubic surface fits, some model data points at high-metallicity and high-ionization parameters have been removed from the fitting procedure, because the modeled behavior is double-valued and cannot be fitted by a simple function. For ionization parameter estimates outside the modeled range, the full model data from L.J. Kewley (in preparation) should be interpolated. The fits in **Table 1** have average errors of $\lesssim 3\%$ or less and cover the range $-4 \lesssim \log(U) \lesssim -2.5$ (or $6.5 \lesssim \log(q) \lesssim 8$).

Note that different authors have used different definitions of the ionization parameter, which can lead to confusion and errors when comparing ionization parameters calculated from different samples. Ionization parameters can be defined on the inner edge of the nebula or as an average throughout the nebula. The ionization parameter is usually defined in terms of the hydrogen density of the gas, but sometimes the ion density or the electron density is used instead. We recommend the application of consistent ionization parameter diagnostics when comparing HII regions and galaxies from different samples.

Table 1 Ionization parameter calibrations for the diagnostic line ratios shown in Figure 7

Bicubic surface fits: $z = A + Bx + Cy + Dxy + Ex^2 + Fy^2 + Gxy^2 + Hyx^2 + Ix^3 + Jy^3$, where $x = \log(\text{line ratio})$, $y = \log(\text{O}/\text{H}) + 12$, $z = \log(U)$								
R	$\frac{\text{CIII}}{\text{CII}}^b$	$\frac{\text{SiIII}}{\text{SiII}}^b$	$\frac{[\text{AlII}]}{[\text{AlI}]}^b$	$\frac{[\text{OIII}]}{[\text{OI}]}^b$	$\frac{[\text{SIII}]}{[\text{SII}]}^b$	$\frac{[\text{NIII}]}{[\text{NII}]}^c$	$\frac{[\text{SIV}]}{[\text{SII}]}^c$	$\frac{[\text{NIII}]}{[\text{NII}]}^c$
Fits for $\log(P/k) = 5.0^a$								
Z_{\min}	7.63	7.63	7.63	7.63	7.63	7.63	7.63	7.63
Z_{\max}	8.93	8.93	8.93	8.93	9.23	9.23	9.23	9.23
$\log(U_{\min})$	−3.98	−3.98	−3.98	−3.98	−3.98	−3.98	−3.98	−3.98
$\log(U_{\max})$	−2.98	−2.73	−2.73	−2.98	−2.48	−2.48	−2.48	−2.48
A	−354.86	−271.55	−56.999	13.768	90.017	−454.99	−236.35	−189.71
B	62.164	68.254	17.186	9.4940	21.934	19.251	10.170	13.207
C	137.35	102.23	22.538	−4.3223	−34.095	168.78	88.399	69.119
D	−15.604	−16.983	−3.4525	−2.3531	−5.0818	−4.6574	−2.3369	−3.1714
E	−1.5532	−2.7208	0.7664	−0.5769	−1.4762	0.0451	0.0849	0.1490
F	−17.901	−13.023	−3.0032	0.2794	4.1343	−21.058	−11.140	−8.5599
G	0.9936	1.0647	0.1910	0.1574	0.3096	0.2962	0.1467	0.1990
H	0.2048	0.3931	0.0000	0.0890	0.1786	0.0000	0.0000	0.0000
I	0.0000	0.0000	0.3419	0.0311	0.1959	0.0000	0.0000	0.0000
J	0.7778	0.5531	0.1300	0.0000	−0.1668	0.8765	0.4683	0.3535
RMS err (%)	1.69	2.71	3.01	1.35	1.96	1.92	2.05	2.94
Fits for $\log(P/k) = 7.0^a$								
Z_{\min}	7.63	7.63	7.63	7.63	7.63	7.63	7.63	7.63
Z_{\max}	8.93	8.93	8.93	8.93	9.23	9.23	9.23	9.23
$\log(U_{\min})$	−3.98	−3.98	−3.98	−3.98	−3.98	−3.98	−3.98	−3.98
$\log(U_{\max})$	−2.48	−2.48	−2.48	−2.48	−1.98	−1.98	−1.98	−1.98
A	−415.93	190.14	13.393	−48.953	22.308	−445.65	−213.24	−164.64
B	49.915	30.405	29.853	6.076	10.928	26.720	11.204	10.994
C	157.61	−67.224	−3.2608	18.139	−9.5322	164.91	80.309	59.247
D	−12.538	−7.1308	−6.5926	−1.4759	−2.3701	−6.4297	−2.6648	−2.6271
E	−0.7865	−4.1040	0.8510	−0.4753	−0.7150	−0.4018	−0.1224	0.1438
F	−20.097	7.6694	0.1452	−2.3925	1.1679	−20.531	−10.206	−7.2715
G	0.8021	0.4308	0.3855	0.1010	0.1432	0.4011	0.1721	0.1647
H	0.1180	0.5029	0.0000	0.0758	0.0793	0.0541	0.0325	0.0000
I	−0.0560	0.1883	0.3998	0.0332	0.1904	0.0000	0.0159	0.0000
J	0.8551	−0.2878	0.0021	0.1055	−0.0476	0.8529	0.4329	0.2976
RMS err (%)	2.43	2.59	1.62	1.48	1.28	1.42	1.71	2.52

Abbreviation: RMS err, root-mean-square error.

^aValid over $Z_{\min} \leq \log(\text{O}/\text{H}) + 12 \leq Z_{\max}$ and $\log(U_{\min}) \leq \log(U) \leq \log(U_{\max})$.

^bWavelengths in angstroms: $\frac{\text{CIII}}{\text{CII}} = \frac{1907 + 1908}{2323.50 + 2324.69 + 2325.40 + 2326.93 + 2328.12}$,
 $\frac{\text{SiIII}}{\text{SiII}} = \frac{1883 + 1892}{1808}$, $\frac{[\text{AlII}]}{[\text{AlI}]} = \frac{1856 + 1862}{1670}$, $\frac{[\text{OIII}]}{[\text{OI}]} = \frac{5007}{3727 + 3729}$, $\frac{[\text{SIII}]}{[\text{SII}]} = \frac{9069 + 9531}{6717 + 6731}$.

^cWavelengths in micrometers: $\frac{[\text{NIII}]}{[\text{NII}]} = \frac{15}{12}$, $\frac{[\text{SIV}]}{[\text{SII}]} = \frac{10.51}{18.71}$, $\frac{[\text{NIII}]}{[\text{NII}]} = \frac{57}{122}$.

3.1. Ultraviolet Ionization Parameter Diagnostics

The UV contains some excellent ionization parameter diagnostics, as shown in Figure 7. Carbon, silicon, sulfur, nitrogen, aluminium, and iron all have multiple stages of ionization that produce emission lines in the UV. Most of these ratios are sensitive to metallicity and ISM pressure; however, there are a few notable exceptions. The $([\text{CIII}] \lambda 1907 + \text{CIII} \lambda 1909)/([\text{CII}] \lambda 2325 \text{ blend})$ provides an ideal ionization parameter diagnostic for low-metallicity galaxies

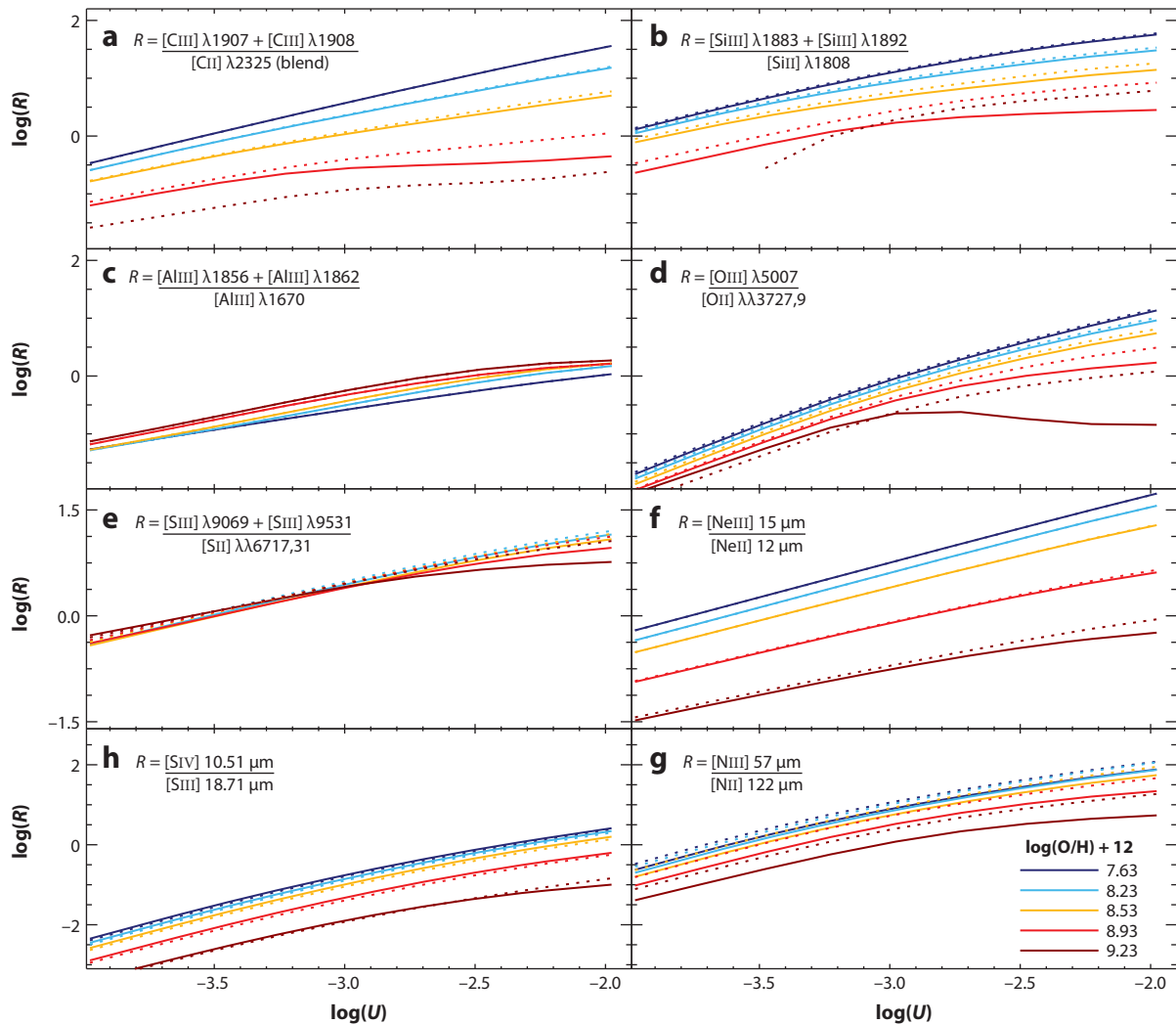


Figure 7

Useful ionization parameter diagnostic line ratios as a function of metallicity (colors *dark blue*, *light blue*, *orange*, *red*, and *burgundy* correspond to $\log(\text{O}/\text{H}) + 12 = [7.63, 8.23, 8.53, 8.93, \text{ and } 9.23]$, respectively). Solid and dotted lines correspond to ISM pressures $\log(P/k) = 5$ and $\log(P/k) = 7$, respectively.

($\log(\text{O}/\text{H}) + 12 \lesssim 8.5$). This diagnostic is based on the blend of lines at 2323.50 Å, 2324.69 Å, 2325.40 Å, 2326.93 Å, and 2328.12 Å, and is less sensitive to ISM pressure and metallicity for this metallicity range (L.J. Kewley, in preparation). The $\text{CIII}/[\text{CII}] \lambda 2325$ ratio is also insensitive to ISM pressure, but requires a correction for metallicity (**Figure 7a**).

The silicon ratios $\text{SiIII} \lambda 1206 / [\text{SiII} \lambda 1260]$ and $(\text{SiIII} \lambda 1883 + \text{SiIII} \lambda 1892) / [\text{SiII} \lambda 1808]$ are extremely stable to variations in pressure for metallicities $\log(\text{O}/\text{H}) + 12 \lesssim 8.5$. In the range $4 < \log(P/k) < 7$, both silicon ratios vary less than 0.1 dex with pressure (**Figure 7b**).

The commonly used optical $[\text{OIII}] / [\text{OI}]$ line ratio has an analog in the UV: $([\text{OIII}] \lambda 1666 + [\text{OIII}] \lambda 1660) / ([\text{OI}] \lambda 2470.22 + [\text{OI}] \lambda 2470.34)$. The UV $[\text{OIII}] / [\text{OI}]$ ratio depends strongly on the metallicity and is stable to variations in ISM pressure at $4 < \log(P/k) < 7$. This diagnostic

should not be used at large pressures and low metallicities; for $\log(P/k) > 7$, the $[\text{OIII}]/[\text{OII}]$ ratio can vary by up to 0.5 dex with pressure when the metallicity is $\log(\text{O}/\text{H}) + 12 \leq 8.23$. Note that in the low-density limit ($n_e \lesssim 20 \text{ cm}^{-3}$), the $[\text{OII}] \lambda\lambda 3727, 9$ line can be used with the $[\text{OII}] \lambda 2470$ doublet as an electron temperature diagnostic (D.C. Nicholls, L.J. Kewley, R.S. Sutherland, M.A. Dopita, in preparation).

The Al_{32} ratio, $([\text{AlII}] \lambda 1856 + [\text{AlII}] \lambda 1862)/[\text{AlII}] \lambda 1670$, is an ideal ionization parameter diagnostic if the spectrum can be corrected for extinction (**Figure 7c**). This ratio is relatively insensitive to metallicity and is stable for all ISM pressures spanned by our models ($4 < \log(P/k) < 9$) for metallicities $\log(\text{O}/\text{H}) + 12 \leq 8.93$. The Al_{32} ratio is usually weaker than the other ionization-sensitive UV lines and may not be observed in high-redshift galaxies except at the highest-ionization parameters.

3.2. Optical Ionization Parameter Diagnostics

The optical spectrum contains two strong-line ionization parameter diagnostics: O_{32} ,² based on the $[\text{OIII}] \lambda 5007/[\text{OII}] \lambda\lambda 3727, 29$ ratio, and S_{32} , based on the $([\text{SIII}] \lambda 9069 + [\text{SIII}] \lambda 9531)/[\text{SII}] \lambda\lambda 6717, 31$ ratio.

The O_{32} ratio was first proposed by Aller (1942) as an excitation diagnostic. This ratio was calibrated theoretically by Kewley & Dopita (2002) and Kobulnicky & Kewley (2004) using a combination of stellar evolution and photoionization models. Recent theoretical calibrations were made by Dors et al. (2011) using single-temperature photoionization models and Morisset et al. (2016) using hybrid photoionization models with fits to optical line ratios of a large sample of HII regions. The O_{32} ratio has a strong dependence on the the gas-phase metallicity, which led Kewley & Dopita (2002) to recommend an iterative approach to solve for both metallicity and ionization parameter. **Figure 7d** shows that in addition to metallicity, the O_{32} ratio is strongly influenced by the ISM pressure in metal-rich galaxies [$\log(\text{O}/\text{H}) + 12 > 9.0$] at pressures $\log(P/k) < 6$ due to collisional de-excitation of $[\text{OII}]$.

The S_{32} ratio was proposed by Kewley & Dopita (2002), but it has been difficult to measure in nearby galaxies because the far-red $[\text{SIII}]$ lines lie at the edge of optical bandpasses in a region of significant sky emission. More recent S_{32} calibrations have been made by Dors et al. (2011) and Morisset et al. (2016). **Figure 7e** shows that the S_{32} ratio is very sensitive to ionization parameter, varying by one and a half orders of magnitude across the full ionization parameter range of our models, with little variation with metallicity (varying only by 0.3 dex in the range of $7.63 < \log(\text{O}/\text{H}) + 12 < 8.93$). The S_{32} ratio is also insensitive to the ISM pressure for $4 < \log(P/k) < 7$.

An important caveat with the use of the S_{32} ratio is that the $[\text{SII}]$ lines have been underestimated by photoionization models in the past; this is especially true at low metallicities. This underestimation has been attributed to the stellar evolution models producing a radiation field that is too soft, i.e., has too few ionizing photons (Kewley et al. 2001a, Levesque et al. 2010), or to the poorly known dielectronic recombination coefficients of sulfur (e.g., Izotov et al. 2009). Dors et al. (2011) cite the use of single-temperature photoionization models as the culprit, but photoionization models with complex temperature structures also underestimate the $[\text{SII}]$ line strength (Levesque et al. 2010). This issue is discussed further in Section 5.3. Until photoionization models can reproduce the $[\text{SII}]$ line strengths across the full range of metallicities observed in HII regions, the S_{32} ratio should be used with caution.

²For readability, we prefer the term O_{32} , rather than $\text{O}32$.

3.3. Infrared Ionization Parameter Diagnostics

IR ionization parameter diagnostics are less affected by extinction than optical or UV diagnostics and are now accessible using sensitive IR and submillimeter instruments. For example, Yeh & Matzner (2012) investigate the use of mid-IR ionization parameters to diagnose radiation and wind pressures in star-forming regions.

The near-IR contains the $S_{32,\text{NIR}}$ ratio of $[\text{SiII}] \lambda 9530 / [\text{SiI}] 1 \mu\text{m}$, where the $[\text{SiI}] 1 \mu\text{m}$ line is a complex of the $[\text{SiI}]$ lines at 1.029, 1.032, 1.034, and 1.037 μm . The $[\text{SiI}] 1 \mu\text{m}$ complex is very weak ($0.02\text{--}0.00005 \times H\beta$), but it has been observed in low metallicity nearby galaxies (Izotov et al. 2009). The $S_{32,\text{NIR}}$ ratio has a complex relationship with pressure and metallicity and is least sensitive to these properties for metallicities $\log(\text{O}/\text{H}) + 12 \leq 8.93$ and for pressures $4 < \log(P/k) < 7$. The $S_{32,\text{NIR}}$ ratio becomes large in high-pressure environments because the $[\text{SiI}]$ lines are collisionally de-excited under these conditions.

The IR $[\text{SiIV}] 10.51 \mu\text{m} / [\text{SiII}] 18.71 \mu\text{m}$ ratio was proposed by Yeh & Matzner (2012), who provide a diagram that calibrates $[\text{SiIV}] / [\text{SiII}]$ in terms of both ionization parameter and hydrogen density. **Figure 7b** shows that the $[\text{SiIV}] / [\text{SiII}]$ ratio is a sensitive function of ionization parameter for all metallicities. This ratio is insensitive to ISM pressure except at the highest pressure and metallicity [$\log(\text{O}/\text{H}) + 12 > 9.0$ and $\log(P/k) = 9.0$]. The close spacing of the $[\text{SiIV}] 10.51 \mu\text{m}$ and $[\text{SiII}] 18.71 \mu\text{m}$ lines allows the ratio to be used even in spectra with limited wavelength coverage, but the $[\text{SiIV}]$ line is weak ($0.0001 \times H\beta$) and likely to be difficult to observe.

In the mid-IR, the Ne_{32} ratio of $[\text{NeIII}] 15 \mu\text{m} / [\text{NeII}] 12 \mu\text{m}$ is a useful diagnostic of the ionization parameter as long as the metallicity is known (**Figure 7f**). Although neon is a noble gas, the collisionally excited $[\text{NeIII}]$ and $[\text{NeII}]$ emission lines are sensitive to the electron temperature of the gas (and therefore the metallicity), especially at high metallicities [$\log(\text{O}/\text{H}) + 12 > 8.53$]. Thornley et al. (2000) first calibrated the Ne_{32} ratio using starburst models that include time evolution. Later, Yeh & Matzner (2012) calibrated the Ne_{32} ratio for ionization parameter and hydrogen density, showing that the Ne_{32} ratio is insensitive to the hydrogen density except at the highest densities. **Figure 7f** indicates that the Ne_{32} ratio is insensitive to ISM pressure, except at the highest metallicities [$\log(\text{O}/\text{H}) + 12 > 8.93$]. The FIR N_{32} ratio ($[\text{NIII}] 57 \mu\text{m} / [\text{NII}] 122 \mu\text{m}$) is less sensitive to metallicity but is more affected by the ISM pressure at high metallicities [$\log(\text{O}/\text{H}) + 12 > 8.53$] than either the $[\text{SiIV}] / [\text{SiII}]$ or $[\text{NeIII}] / [\text{NeII}]$ ratios (**Figure 7b**).

3.4. Mixed Line Ratio Diagnostics

Mixed line ratios are primarily used when lines from two ionization states of the same species are unavailable in a spectrum. This situation often occurs at redshift $z \sim 0.7$, where only part of the rest-frame blue spectrum is available in the optical. Mixed ratios usually have a larger dependence on the metallicity than ratios of a single species. Mixed ratios should only be used if the gas-phase metallicity is known and is considered in the ionization parameter diagnostic.

The optical $[\text{NeIII}] \lambda 3968 / [\text{OI}] \lambda \lambda 3727, 9$ ratio was first proposed by Levesque et al. (2010) for this situation. This ratio is very sensitive to the ISM pressure and metallicity and should only be used to determine ionization parameter if both the ISM pressure and metallicity can be reliably estimated.

The $[\text{OIII}] \lambda 5007 / H\beta$ ratio is correlated with ionization parameter for metallicities $\log(\text{O}/\text{H}) + 12 < 8.53$ ($[\text{OIII}] / H\beta < 0.5$). In this range, the $[\text{OIII}] / H\beta$ ratio varies less than 0.4 dex with metallicity and can be used to provide a rough estimate of the ionization parameter. The $[\text{OIII}] / H\beta$ should not be used to measure ionization parameter in super star clusters or luminous IR galaxies because the $[\text{OIII}] / H\beta$ ratio becomes insensitive to ionization parameter at $\log(U) > -2.63$.

The IR [OIII] 52 μm /[SIII] 33 μm ratio was used by Cotera et al. (2005) to trace the ionization parameter in the Arches cluster. Like [OIII]/H β , this ratio is a strong function of ionization parameter but becomes insensitive to ionization parameter at larger ionization parameters [$\log(U) > -2.63$] (L.J. Kewley, in preparation). The [OIII]/[SIII] ratio is insensitive to ISM pressure variations in the range of $4 < \log(P/k) < 6$.

4. METALLICITY IN GALAXY EVOLUTION STUDIES

Measuring the chemical history of galaxies is critical to our understanding of galaxy formation and evolution. In a simple closed-box model of chemical evolution, metals increase over time through each generation of star formation. However, the closed-box model can explain neither the complex relationship between the chemical abundances and the luminosity or stellar mass of galaxies (Tremonti et al. 2004, Dalcanton 2007, Finlator & Dave 2007) nor the evolution of these properties with time (Kobulnicky & Kewley 2004, Yuan et al. 2013, Zahid et al. 2013b).

The metallicity history of galaxies is usually characterized as a function of stellar mass. Theory predicts that as time progresses, the mean metallicity of galaxies increases with age as galaxies undergo chemical enrichment, whereas the stellar mass of a galaxy will increase with time as galaxies are built through merging and other accretion processes (e.g., Somerville & Primack 1999, Nagamine et al. 2001, De Lucia et al. 2004, Davé et al. 2011, and references therein).

The gas-phase metallicity strongly correlates with the stellar mass and the galaxy bolometric luminosity. A correlation between mass and metallicity naturally arises if low-mass galaxies have larger gas fractions than higher-mass galaxies, as observed in local galaxies (McGaugh & de Blok 1997, Bell & de Jong 2000, Boselli et al. 2001) and recently produced in simulations (Hunt et al. 2016, Ma et al. 2016, De Rossi et al. 2017). The detailed relationship between metallicity and mass depends on accretion of material from the intergalactic medium (IGM), as well as galactic-scale outflows driven by supernovae, stellar winds, or AGNs (Wild et al. 2008).

The MZ (mass–metallicity) and luminosity–metallicity (LZ) relations were observed first in irregular and blue compact galaxies (Lequeux et al. 1979, Kinman & Davidson 1981), and later in disk galaxies (e.g., Rubin et al. 1984, Wyse & Silk 1985, Vila-Costas & Edmunds 1992, Garnett 2002). The local MZ relation is now well known, thanks to large local spectroscopic surveys such as the Sloan Digital Sky Survey (SDSS) and the Two-degree Field Galaxy Redshift Survey (2dFGRS) (e.g., Baldry et al. 2002, Tremonti et al. 2004, Wu et al. 2016, and references therein). The local MZ relation is steep for masses $\lesssim 10^{10.5} M_{\odot}$ and flattens at higher stellar masses. These characteristics have been interpreted in terms of efficient galactic-scale winds that remove metals from low-mass galaxies ($M \lesssim 10^{10.5} M_{\odot}$) and a saturation in the chemical yield (Pettini 2002, Tremonti et al. 2004, Zahid et al. 2014). Alternative scenarios include low star-formation efficiencies in low-mass galaxies caused by supernova feedback (Brooks et al. 2007) and a variable integrated stellar initial mass function (Köppen et al. 2007).

Most investigations into the metallicity history of star-forming galaxies focus on the change in the MZ relation with redshift. The MZ relation (or the related LZ relation) has now been measured to $z > 3$ (e.g., Shapley et al. 2004; Savaglio et al. 2005; Erb et al. 2006; Liang et al. 2006; Maier et al. 2006; Zahid et al. 2011, 2013a; Yuan et al. 2013; Ly et al. 2016). Some authors have reported a tight correlation between gas-phase metallicity, stellar mass, and SFR that does not evolve with redshift (Lara-López et al. 2010, Mannucci et al. 2010, Henry et al. 2013). However, this relationship, its tightness, and observed evolution appear to be affected by systematic uncertainties in the derived metallicity, stellar mass, and SFRs (Yates et al. 2012, Andrews & Martini 2013, Sánchez et al. 2013, Cullen et al. 2014, Ly et al. 2014, Maier et al. 2014, Salim et al. 2014, Wuyts et al. 2014, Kashino et al. 2016). The relationship is also affected by environment

(Scudder et al. 2012) and may be caused by the more fundamental relationship between gas mass, stellar mass, and SFR (Lilly et al. 2013, Troncoso et al. 2014, Zahid et al. 2014, Ma et al. 2016).

Within galaxies, metallicity gradients vary depending on galaxy type, mass, and environment. Isolated spiral galaxies like our Milky Way typically have steep metallicity gradients, which is consistent with inside-out disk formation, in which early nuclear star formation enriches the central gas with metals (e.g., Chiappini et al. 2001). The gradient subsequently builds up over time as accretion from the surrounding IGM and satellites causes star formation to form further and further out in the disk (e.g., Fu et al. 2009, Kobayashi & Nakasato 2011, Cunha et al. 2016). When normalized by galaxy size, isolated galaxies have very similar gradients, suggesting a common star-formation and gas accretion history (Sánchez et al. 2014, Ho et al. 2015). Low-mass galaxies have flatter or even inverted gradients because the crossing timescale is short, allowing efficient mixing of the gas (Carton et al. 2018, Wang et al. 2018, and references therein).

The gas-phase metallicity gradient is extremely sensitive to environment and gas infall. Galaxy mergers drive pristine gas from the outer regions into the central regions, flattening metallicity gradients (Kewley et al. 2010, Rupke et al. 2010, Rosa et al. 2014, Torres-Flores et al. 2014). *N*-body merger models indicate that major gas infall occurs at two stages during the merger: at first close passage, and during final coalescence, both of which flatten metallicity gradients (Perez et al. 2011, Torrey et al. 2012). Cosmological simulations support this scenario (Bustamante et al. 2018). Late-stage mergers have extremely flat metallicity distributions (Rich et al. 2012). If galactic-scale winds quench star formation at late merger stages, the postmerger galaxy may not ever fully recover a steep metallicity gradient. Thus, the combination of observed metallicity gradients and *N*-body merger simulations has the potential to age-date mergers based on recent gas infall and to constrain the amount of star-formation quenching at late merger stages.

The gas-phase metallicity can be determined from a wide variety of emission lines from the UV through the IR. In HII regions, the abundance can sometimes be determined from recombination lines. Recombination lines from hydrogen and helium are readily observed in spectra of HII regions and galaxies, but the recombination lines of other elements, such as oxygen and carbon, are weak and are only measurable in a few nearby regions. Instead, three other techniques are commonly used. The traditional method for deriving metallicity, known as the direct method, is based on the electron temperature from sensitive auroral lines in the optical spectrum. The auroral lines are weak and often not detected in metal-rich galaxies. To overcome this problem, empirical calibrations were created, providing relations between auroral line metallicities and strong line flux ratios. However, both methods rely on samples of HII regions, simplified assumptions, and correction for unseen stages of ionization. To overcome these issues, theoretical methods based on photoionization models were developed. Each of these methods has its own strengths and weaknesses, and massive discrepancies exist among all methods [see Stasińska (2005), Kewley & Ellison (2008), and Peimbert et al. (2017) for an overview]. Here, we discuss each method and associated caveats.

4.1. Auroral Line Metallicities

The use of temperature-sensitive auroral lines to measure metallicities is commonly called the direct method. This is a misleading term because there are many steps and assumptions in the derivation of metallicity from an auroral line (see, e.g., Dinerstein 1990, López-Sánchez et al. 2012). A particularly useful tutorial is given by Pérez-Montero (2017). An ionic abundance is calculated with a simple photoionization model of a five-level atom, assuming a homogeneous (constant density, constant temperature) medium. The models of Aller (1984) or *Temden* of the Image Reduction and Analysis Facility (IRAF) (De Robertis et al. 1987, Shaw & Dufour 1995) are

commonly used, along with atomic data from Mendoza & Zeippen (1983). The atomic model is used in conjunction with the ratio of an auroral line to a nearby line of the same species to calculate the electron temperature, T_e , of that ionic zone.

The main auroral line used to determine metallicities is the [OIII] $\lambda 4363$ line. Both the [OIII] $\lambda 4363$ line and the nearby [OIII] $\lambda\lambda 4959, 5007$ lines are used to derive electron temperature in the O^{2+} zone, $T_e([OIII])$. $T_e([OIII])$ does not represent the average electron temperature, so the temperature in the unseen zones also needs to be estimated. Two ionization zones are usually assumed; a high-ionization ($H^+ + He^+$) zone and a low-ionization ($H^+ + He^0$) zone. Some authors use average electron temperatures of several atoms to estimate the electron temperature in each zone (e.g., López-Sánchez et al. 2012). Usually, the temperature in the O^+ zone, $T_e([OI])$, is calculated based on a fit to the relation between $T_e([OI])$ and $T_e([OIII])$ derived from photoionization models. An electron density needs to be included, which is calculated with the [OII] or [SII] doublets based on photoionization models of simple atoms. The temperatures are then used to calculate ionic abundances, which are the abundances of each ion (i.e., O^+ and O^{2+}).

To calculate the total oxygen abundance relative to hydrogen, the ionic abundances need to be corrected for the unseen stages of ionization. Usually, an ionization correction factor (ICF) is used. The ICF is based on photoionization models, sometimes with inputs from observed emission lines, such as [OII] $\lambda 3727$ or HeII $\lambda 4686$ (Izotov & Thuan 1999). Model fits to sets of emission-line fluxes can be used to derive the ICF (e.g., Stasińska 1980, Mathis & Rosa 1991). These models assume a hydrogen density, the gas distribution, and the fraction of ionizing photons that are absorbed by the nebula. Dust modifies the radiation field absorbed into the nebula, and the stellar radiation field needs to be accurately estimated using stellar atmosphere models. Mathis (1985) gives a comprehensive and useful summary of the computation method and issues inherent in estimating ICFs, as well as tables of ICFs for various species. López-Sánchez et al. (2012) provide a fit to the relationship between oxygen abundance and electron temperature. (See the sidebar titled A Note on Solar Abundances.)

Significant errors can be introduced into metallicity estimates through the ICF. The calculation of an ICF usually assumes that the electron temperature is constant and that the HII region is composed of atoms of only one, or a small number of, species. However, the electron temperature can differ by 2,000–3,000 K from one HII region to another (Hägele et al. 2006), and we know that HII regions are multizone ionized regions composed of atoms of many species. The ionization of elements depends strongly on the stellar radiation field, which is reliant on our understanding of stellar atmospheres. Hägele et al. (2008) show that an accurate T_e estimate requires the measurement of multiple faint auroral lines ([OII], [SII], [OIII], [SIII], and [NII]) and their accurate (better than 5%) ratios to Balmer recombination lines. Without these lines, the assumed ICF can differ significantly from the actual unseen stages of ionization in low-excitation HII regions, causing the T_e metallicity to be underestimated by up to 0.2 dex (Hägele et al. 2008).

A NOTE ON SOLAR ABUNDANCES

It is preferable to use $\log(O/H) + 12$ to refer to the gas-phase metallicity rather than units in terms of solar, because solar abundances are not representative of local present-day galactic abundances. Asplund et al. (2009) give a bulk solar abundance of $\log(O/H) + 12 = 8.72$ and a surface solar abundance of $\log(O/H) + 12 = 8.69$. The surface solar abundance shows evidence of evolution and mixing, and the bulk solar abundance is an estimate of the abundance when the Sun formed, i.e., 4.7 billion years ago. Local B stars [$\log(O/H) + 12 = 8.76$] may be more representative of local galactic abundances [see Nicholls et al. (2017) for a discussion].

In a chemically homogeneous medium, T_e lines originate from regions that are of low density and metal poor. This bias is caused by the fact that the T_e line is predominantly produced in hot gas (Dinerstein 1990). At the low temperatures typical of metal-rich regions, collisional excitation of the [OIII] lines is small. Therefore, integrated emission of the [OIII] $\lambda 4363$ line is weighted toward the hottest zones of an HII region. The standard auroral [OIII] $\lambda 4363$ line is therefore rarely observed at metallicities $\log(\text{O}/\text{H}) + 12 > 8.7$ (Peimbert 1967, Rubin 1969, Stasińska 2005), and it is highly sensitive to temperature gradients and stratification (Peimbert & Costero 1969). Multiple mechanisms for generating electron temperature fluctuations have been proposed, including shock waves and turbulence (Peimbert et al. 1991, O'Dell et al. 2015), mechanical energy from stellar winds produced by planetary nebulae (Peimbert et al. 1995), and WR stars (Gonzalez-Delgado et al. 1994).

This temperature effect causes a significant sample bias. Hoyos & Díaz (2006) analyzed a large sample of HII regions and analyzed the differences between galaxies with and without detections of the [OIII] $\lambda 4363$ line. They showed that HII regions and galaxies without auroral line detections are more metal rich, are more luminous, and have a lower ionization parameter than those in which the auroral line is detected. Theoretical models suggest that temperature gradients can cause the T_e metallicity to be systematically underestimated by up to 0.9 dex at high metallicity [$\log(\text{O}/\text{H}) + 12 \sim 9.0$] (Stasińska 2005).

Most auroral methods assume a constant density throughout the nebula. Copetti et al. (2000) found that 50% of their sample of galactic HII regions have internal variations in electron density, whereas 60% of giant extragalactic HII regions have internal electron density variations (Malmann et al. 2002). Luridiana & Cerviño (2003) discuss the effect of density gradients on abundances calculated using T_e methods with various ICFs. They find that the T_e metallicity from oxygen is relatively insensitive to density gradients, as long as all the different ionization stages of oxygen have been observed. However, they suggest that nitrogen and sulfur abundances may become unreliable where large density gradients exist.

Recently, Nicholls and colleagues (D.C. Nicholls, L.J. Kewley, R.S. Sutherland, M.A. Dopita, in preparation) used photoionization models to recalibrate the relationship between metallicity and the [OIII] $\lambda\lambda 1660, 66$, [OIII] $\lambda 2321$, and [OIII] $\lambda 4363$ auroral lines. These recalibrations include the latest collisional, radiative excitation/de-excitation, and collisional cross-section data, as well as full cascade from higher energy levels. Nicholls and colleagues point out that auroral line calibrations give an atomic equivalent temperature,³ which may be used to estimate an average temperature and oxygen abundance, but do not take into account the heterogeneous structure of emission-line nebulae. (See the sidebar titled A Note on Solar Abundances.)

4.2. Auroral-Strong Line Calibrations

Metallicity calibrations based on optical strong-line ratios were first developed for measuring metallicities in HII regions in which the auroral lines are not observed. These calibrations are derived by fitting the observed relationship between auroral metallicities and strong-line ratios and are often referred to as empirical methods. The use of the term empirical is misleading because it implies that the metallicities are directly observed and neglects the theoretical atomic models and assumptions that the auroral method is based on.

³Atomic equivalent temperature is the electron temperature of a dust-free, isolated assembly of oxygen atoms at a uniform electron density and a single electron temperature that generate the same emission-line flux ratios as those of observed data.

Many auroral strong-line calibrations exist in the literature. **Figure 8** compares the auroral strong-line calibrations for three commonly used metallicity-sensitive line ratios: R_{23} ,⁴ $[\text{OIII}]/\text{H}\beta/[\text{NII}]/\text{H}\alpha$ (known as O3N2), and $[\text{NII}]/\text{H}\alpha$. These calibrations were derived by the original authors using simple curve fits to auroral metallicities of either HII region spectra or integrated spectra of galaxies.

The differences among the auroral strong-line calibrations are dramatic: Estimates vary up to 1 dex in metallicity. The earlier calibrations were based on very small numbers of HII regions that led to unusual shapes in the lower-metallicity ends of the R_{23} and $[\text{NII}]/\text{H}\alpha$ calibrations. For calibrations developed after 1989, the discrepancies are up to 0.6 dex in R_{23} , 0.5 dex in O3N2, and more than 0.9 dex in $[\text{NII}]/\text{H}\alpha$. The magnitude of these discrepancies has not improved in the past decade, despite significantly larger samples of HII regions being used. The causes of these discrepancies are difficult to dissect and could be a product of many effects including all of the potential limitations with the auroral method described in Section 4.1 as well as sample bias.

Sample bias enters from at least two assumptions: (a) that HII regions will always show the auroral lines if observed for a sufficient time, and (b) that HII regions with auroral lines are representative of all HII regions and galaxies. In the past, the number of HII regions with measurable T_e abundances was small, and authors often combined T_e observations of HII regions from different galaxies (including galaxies of different types), and HII regions observed with different methods. In the 1970s–1990s, some HII region samples were observed with objective prism surveys, which are known to be biased toward strong $[\text{OIII}] \lambda 4959, 5007$. Recently, integral field spectroscopy has made it possible to derive T_e metallicities for large numbers of galaxies (Marino et al. 2013, Curti et al. 2017), which allows sample bias to be understood and largely overcome.

Recently, stacking has been used on large galaxy samples to increase the signal-to-noise (S/N) ratio of the auroral lines in galaxies (Liang et al. 2007, Andrews & Martini 2013, Brown et al. 2016). Andrews & Martini (2013) show that auroral metallicities have a factor of 2–3 times larger dependence on the SFR than strong-line metallicity methods, whereas Brown et al. (2016) show that the HII regions and stacked data used in auroral line samples and stacked galaxy data do not span the full range of line ratios seen in the full sample of individual SDSS galaxies. These studies emphasize the need to analyze all the HII regions in samples both with and without auroral line detections. A simple exercise to test for sample bias is to compare the strong-line ratio distributions (i.e., $[\text{OIII}]/[\text{OII}]$, $[\text{NII}]/\text{H}\alpha$, R_{23}) of the HII regions with and without auroral line detections. An auroral line subsample is only representative of all HII regions if it can span the full range of line ratios seen in all HII regions.

Some empirical calibrations attempt to overcome the sample biases of the empirical methods by including theoretical model fits to individual HII region data at the high-metallicity end (e.g., Pettini & Pagel 2004, Maiolino et al. 2008). One of the first metallicity calibrations, by Pagel et al. (1979), is based on HII regions with auroral metallicities at low abundances and on photoionization model fits to a metal-rich HII region in the galaxy M101. Such model fits rely on assumptions about the stellar radiation field within the HII region, and the resulting calibrations are still dependent on the choice of HII regions across the entire metallicity range. These mixed calibrations typically give metallicities that are in between auroral metallicities and pure photoionization methods.

Depletion of oxygen onto dust grains has traditionally not been taken into account in auroral line methods. Dust depletion measurements in nearby HII regions require a 0.08–0.11 dex correction to the oxygen abundance measurements (Mesa-Delgado & Esteban 2010, Peimbert & Peimbert 2010). Peimbert & Peimbert (2010) recommend dust corrections of +0.11 dex to the measured $\log(\text{O}/\text{H}) + 12$ for HII regions with $\log(\text{O}/\text{H}) + 12 > 8.3$, +0.10 dex for $8.3 > \log(\text{O}/\text{H}) + 12 > 7.8$, and +0.09 dex for HII regions with $7.8 > \log(\text{O}/\text{H}) + 12$.

⁴For readability, we prefer the term R_{23} , rather than R_{23} .

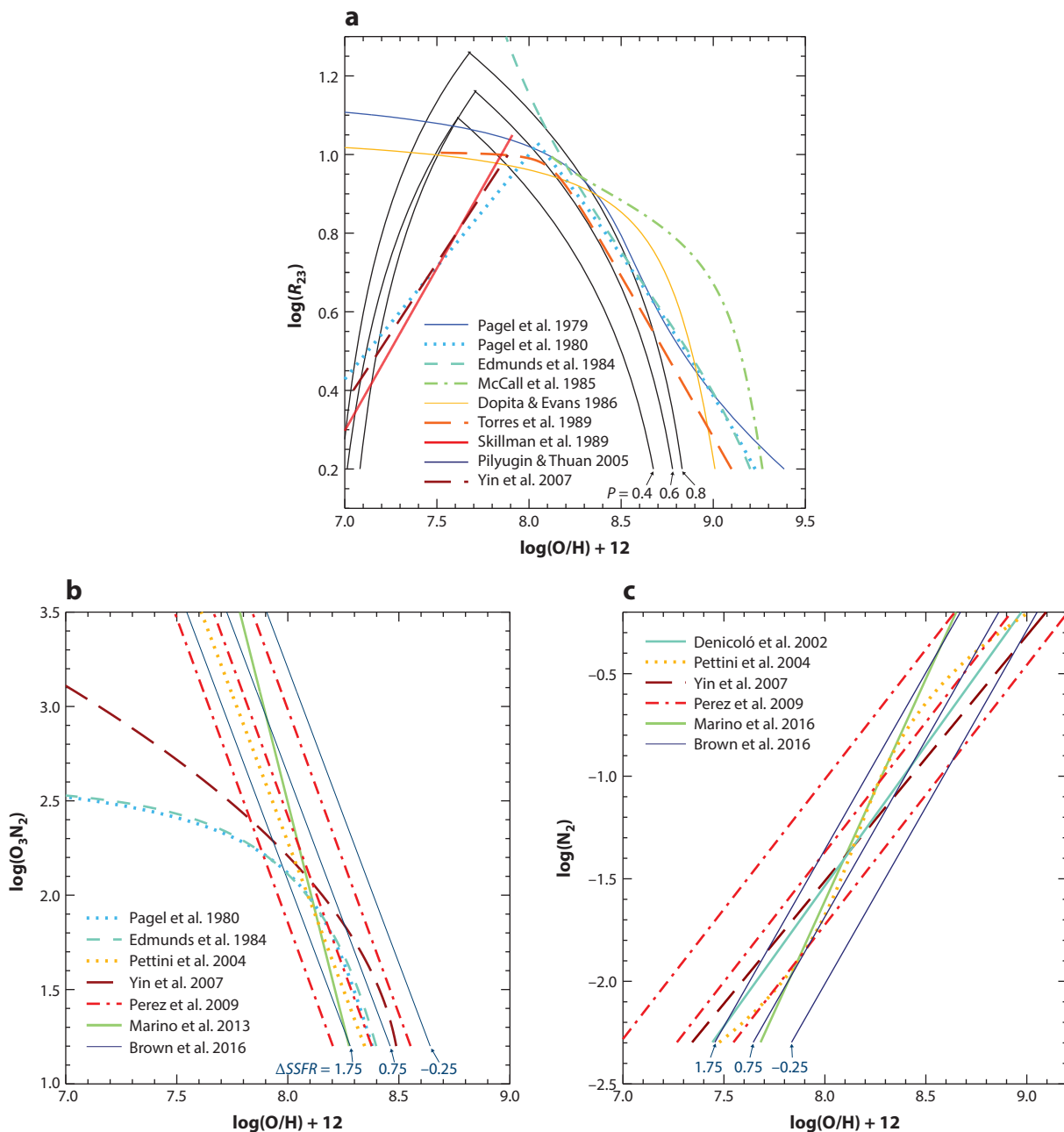


Figure 8

Empirical calibrations based on fits to T_e metallicities for samples of HII regions or galaxies. Empirical calibrations for the ratios of (a) R_{23} , (b) $[\text{OIII}]/\text{H}\beta/[\text{NII}]/\text{H}\alpha$ (O3N2), and (c) $[\text{NII}]/\text{H}\alpha$ (N_2) are shown. Some calibrations include corrections for the ionization state of the gas, which is represented by a parameter P in the Pilyugin & Thuan (2005) method, and an offset in specific star-formation rate, Δ_{SSFR} , in the Brown et al. (2016) method. Large discrepancies exist among the many empirical calibrations.

4.3. Recombination Line Methods

Recombination line fluxes are almost all proportional to the electron density and inversely proportional to the electron temperature. These relationships hold across an order of magnitude change in electron temperature and for densities up to 10^{10} cm^{-3} . As a result, an error in the measured electron temperature or density has negligible effect on the resulting metallicity estimates, and recombination lines are often used as a gold standard for comparison to other, more problematic metallicity estimation techniques. Peimbert et al. (2017) give an excellent tutorial and review of the use of recombination lines and auroral lines to determine metallicities. Aside from the helium lines, the $[\text{CII}] \lambda 4267$ and $[\text{OII}] \lambda 4650$ doublets are most commonly used to determine metallicities.

The main disadvantage of using recombination lines for deriving metallicities is that aside from hydrogen and helium, the recombination lines are very weak and are only seen in nearby HII regions and planetary nebulae. In these regions, the recombination lines have been successfully used to measure carbon and oxygen abundances in the Milky Way and in some nearby extragalactic HII regions (Peimbert & Peimbert 2013, and references therein). Recombination lines have been used to determine the steep metallicity gradient in our Milky Way (Esteban et al. 2005), as well as a flattening in the gradient at the outskirts of the Milky Way (Esteban et al. 2013).

In HII regions, recombination lines consistently give larger metallicities than auroral methods (French 1983, Peimbert et al. 1993, Mathis & Liu 1999). The electron temperatures of recombination lines are larger by $16.1 \pm 0.01\%$ than the electron temperatures of HII regions measured with the auroral lines (e.g., Peimbert & Peimbert 2013). The scatter in this offset for HII regions is remarkably small. For planetary nebulae, the offset is in the same direction and is larger on average ($27 \pm 0.03\%$). The logarithm of the difference between the recombination line and auroral metallicities is known as the abundance discrepancy factor (ADF). The ADF is around ~ 0.2 dex in many Milky Way and extragalactic HII regions (García-Rojas et al. 2005, 2014; García-Rojas & Esteban 2007; Esteban et al. 2009), but is as large as 0.59 dex in some cases (Liu et al. 2000, 2006; Tsamis et al. 2004, 2008; Mesa-Delgado & Esteban 2010). The ADFs for C/O and N/O abundances appear to be significantly smaller (Zuckerman & Aller 1986).

Peimbert (1967) proposed that electron temperature fluctuations in HII regions cause the ADF. Auroral lines are significantly more sensitive to the electron temperature of the gas than recombination lines; auroral lines depend exponentially on a single assumed electron temperature, whereas recombination methods scale with electron temperature through a power law. Peimbert & Peimbert (2013) show that the pressure within the regions where the auroral lines are produced is larger than the pressure within the recombination line regions, suggesting that the auroral lines are produced in higher pressure, higher temperature regions. These high-pressure regions may result from the dissipation of turbulent energy in shocks or from magnetic reconnection.

Electron temperature correction methods assume that the ADF is entirely due to electron temperature discrepancies and that the ISM is chemically homogeneous. However, Tsamis & Péquignot (2005) argue that small-scale chemical inhomogeneities from incomplete small-scale mixing are responsible for the abundance discrepancy. They produced tailored photoionization models to the UV, optical, IR, and radio spectra of 30 Doradus. Their models reproduce the recombination lines and nebular lines only if chemical inhomogeneities exist in the nebula.

High-S/N spatially resolved spectra of individual HII regions can quantify dust depletion, chemical inhomogeneities, and temperature fluctuations, which can then be taken into account in tailored photoionization modeling. When the thermal and ionization structure of the nebula and dust depletion are taken into account, the systematic temperature differences from different methods can be resolved in some cases (Peña-Guerrero et al. 2012).

Recently, Nicholls et al. (2012) proposed that there may be departures from thermal equilibrium in the electron energies described by a parameter κ . This distribution is capable of explaining the discrepancy in a physically plausible way. The equilibrium Maxwell–Boltzmann distribution is the limiting case of a κ distribution in which $\kappa = \text{infinity}$. Livadiotis et al. (2018) demonstrated that κ distributions can arise naturally in astrophysical plasmas. However, Draine & Kreisch (2018) argue that κ distributions do not arise in HII regions or planetary nebulae.

The full cause of the ADF remains unknown. Metallicity calibration discrepancies can mimic or hide metallicity evolution with redshift and may significantly change metallicity gradient estimates. Until the abundance discrepancy is conclusively resolved, we recommend (*a*) the application of a consistent calibration or calibrations across all samples or all HII regions being studied, and (*b*) the use of several metallicity calibrations to quantify the effect of different metallicity calibrations on the scientific conclusions.

4.4. Theoretical Metallicity Diagnostics

Purely theoretical metallicity calibrations were developed to overcome the systematic differences among the auroral strong-line calibrations as well as the discrepancy between the auroral and recombination line metallicities. Theoretical calibrations are calculated by combining stellar population synthesis and photoionization models. McGaugh (1991) created the first theoretical metallicity calibrations using stellar evolution tracks to calculate the ionizing radiation field corresponding to a zero-age burst. He calculated theoretical calibrations between line ratios and metallicity that take into account the relationship between radiation field and temperature. Theoretical calibrations were subsequently computed with updated photoionization models (e.g., Charlot & Longhetti 2001, Kewley & Dopita 2002, Kobulnicky & Kewley 2004, Dors et al. 2011, Nagao et al. 2011, Morisset et al. 2016, Byler et al. 2018, and references therein).

One of the major benefits of theoretical calibrations is that a large range of parameter space can be explored, allowing one to understand the effects of galaxy properties. In this section, we illustrate the effect of ionization parameter and ISM pressure on the diagnostic line ratios, and provide new calibrations that take these parameters into account, where needed. The main disadvantages of theoretical calibrations are the model assumptions, which include a plane parallel or spherical geometry, uncertain stellar atmosphere models, reliance on current atomic data, and (sometimes) a simplified temperature and density structure. We discuss these issues further in Sections 5.3 and 7.

Bayesian methods have recently been developed that use theoretical models to fit the observed nebular emission lines (Brinchmann et al. 2004, Tremonti et al. 2004, Blanc et al. 2015, Chevallard & Charlot 2016, Thomas et al. 2018a). These methods are primarily used to derive metallicity but may also be used to calculate the ISM pressure, ionization parameter, and other galaxy properties (e.g., Thomas et al. 2016). With Bayesian methods, the number of parameters being solved needs to be equal to or less than the number of constraints provided by the emission lines and continuum. Bayesian methods are very powerful, but without priors, they do not take into account the regimes over which specific lines are not valid diagnostics. For example, the [NII] and [OII] lines may be used in Bayesian methods as the main constraint of metallicity in the low-metallicity regime in which the [NII]/[OII] ratio is in fact insensitive to metallicity. An understanding of the sensitivity of the diagnostic lines to other galaxy parameters and the limitations of sets of emission lines is essential for interpreting the estimates derived from Bayesian methods. The use of priors is recommended to ensure that emission lines are only used when they provide useful estimates of the parameter of interest. (See the sidebar titled Understanding Bayesian Metallicity Estimates.)

UNDERSTANDING BAYESIAN METALLICITY ESTIMATES

Students should first apply individual strong-line calibrations to gain an understanding of the diagnostics being used prior to applying Bayesian methods. Being based on the same models, Bayesian methods suffer from many of the same limitations as the individual calibrations, and unreliable estimates can be difficult to identify without a physical understanding of the limitations of each set of emission lines.

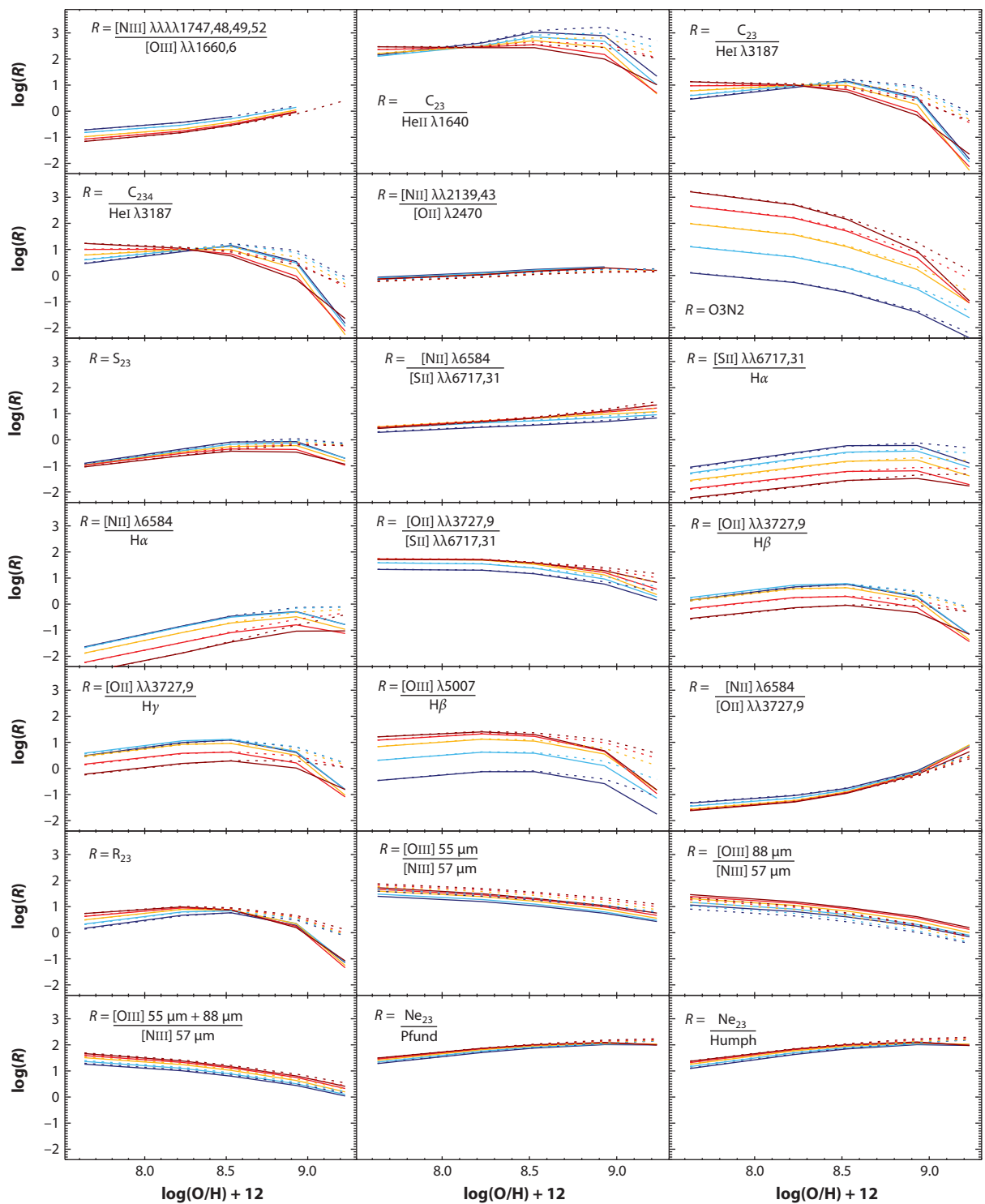
4.5. Theoretical Ultraviolet Metallicity Diagnostics

UV metallicity diagnostics are scarce and were originally developed to interpret *International Ultraviolet Explorer* or Cosmic Origins Spectrograph data of HII regions and small samples of galaxies. Recently, new UV diagnostics have been developed that will be key tools for interpreting spectra from the next-generation space and ground-based telescopes (Vidal-García et al. 2017, Byler et al. 2018). Byler et al. (2018) combined Starburst99 stellar evolution models with CLOUDY photoionization models to investigate the diagnostic potential of the UV lines, focusing on [CIII] λ 1907, CIII] λ 1909, OIII] $\lambda\lambda$ 1661,66, SiIII] $\lambda\lambda$ 1883,92, CIV $\lambda\lambda$ 1548,1551, NII] $\lambda\lambda$ 1750,52, and MgII λ 2796. They provide a useful suite of emission-line and equivalent width diagnostic diagrams for the separation and identification of metallicity and ionization parameter, as well as a figure giving key diagnostic UV emission lines and their observability with the Near-Infrared Spectrograph on the *James Webb Space Telescope*.

Figure 9 shows the most promising UV metallicity diagnostics, where colors correspond to ionization parameter, and solid and dotted lines give ISM pressures of $\log(P/k) = 5$ and $\log(P/k) = 7$, respectively. **Table 2** gives the coefficient fits for the diagnostics in terms of the ionization parameter.

Hydrogen lines are often used as baselines for metallicity diagnostics. There are no useful hydrogen lines in the UV, so we use the HeI λ 3187 and the HeII λ 1640 lines as proxies. The HeI λ 3187 line is an ideal proxy because it is $10\times$ stronger than HeII in a typical spectrum, and it is less sensitive to uncertainties in the EUV spectrum through the stellar atmosphere models. It is important to keep in mind that the ionization potential of the HeII line (54.4 eV) is in a region of the EUV spectrum where stellar atmosphere uncertainties are large, and the number of ionizations into He⁺ is very sensitive to the ionization parameter.

The UV contains many carbon lines that may be used in metallicity diagnostics. The C₂₃/HeI ratio is useful as a metallicity diagnostic in metal-rich regimes [$\log(\text{O}/\text{H}) + 12 > 8.5$], where the dependence on ionization parameter is significantly reduced. The CIII] $\lambda\lambda$ 1906, 08 lines are usually strong in star-forming galaxies and trace the C⁺⁺ zone, whereas the [CII] λ 2325 blend (i.e., the sum of 2323.50 Å, 2324.69 Å, 2325.40 Å, 2326.93 Å, and 2328.12 Å) traces the C⁺ zone. Ideally, the full suite of [CII], CIII], and [CIV] lines could be used to measure metallicity via the C₂₃₄/HeI ratio, but the [CIV] line can be contaminated by line-driven winds from massive stars, affecting the ratio by 0.1–0.3 dex (Byler et al. 2018). The C₂₃ ratios are double-valued with metallicity for most ionization parameters because (like all collisionally excited lines), at low metallicities, the nebula is hot, and the ionized carbon emission scales with carbon abundance. At high metallicity, the low temperatures prevent much of the collisional excitations of the carbon ions. In this domain, the mid-IR fine structure lines contribute significantly to the cooling of the nebula. Additional line ratios are needed to determine whether the C₂₃ metallicity lies on the upper or lower branch. The C₂₃ ratio is strongly dependent on both ionization parameter and ISM pressure, and C₂₃ diagnostics need to include a correction for these factors. However, at the large ionization parameters typical



(Caption appears on following page)

Figure 9 (Figure appears on preceding page)

UV–optical–IR metallicity diagnostic ratios versus metallicity in units of $\log(\text{O}/\text{H}) + 12$. Colors blue through red correspond to ionization parameter $\log(U) = [-3.98, -3.73, -3.48, -3.23, -2.98, -2.73, -2.48, -2.23, \text{ and } -1.98]$. Solid and dotted lines give ISM pressures of $\log(P/k) = 5$ and $\log(P/k) = 7$, respectively.

of high-redshift galaxies, the C_{23}/HeI and C_{234}/HeI ratios provide useful monotonic diagnostics of metallicity that vary little with ionization parameter.

The $\text{Si}_{23}/\text{HeI}$ and $\text{Si}_{23}/\text{HeII}$ ratios using the $\text{SiIII} \lambda\lambda 1883, 92$ and $\text{SiIII} \lambda 1808$ lines are sensitive metallicity diagnostics, but they should be used with caution because silicon can be heavily

Table 2 Metallicity diagnostic calibrations for UV and optical line ratios described in Sections 4.5–4.7

Bicubic surface fit: $z = A + Bx + Cy + Dxy + Ex^2 + Fy^2 + Gxy^2 + Hyx^2 + Ix^3 + Jy^3$, where $x = \log(R)$, $y = \log(U)$, $z = \log(\text{O}/\text{H}) + 12$, and $\log(P/k) = 5.0^a$					
R	$\frac{[\text{NII}]}{[\text{OII}]}^b$	$\frac{C_{23}}{\text{HeII}}^b$	$\frac{C_{23}}{\text{HeI}}^b$	$\frac{C_{234}}{\text{HeI}}^b$	$\frac{[\text{NII}]}{[\text{OII}]}^b$
Z_{\min}	7.63	8.53	8.53	8.53	7.63
Z_{\max}	8.93	9.23	9.23	9.23	8.93
A	8.0527	10.8288	10.3120	10.3407	12.3718
B	2.9475	0.1049	−0.6145	−0.5974	17.6449
C	−1.0845	2.1818	1.7227	1.7496	−1.7778
D	1.3608	0.5483	−0.1752	−0.1654	0.8281
E	2.1376	0.4194	−0.1032	−0.0986	17.8471
F	−0.3984	0.9858	0.6505	0.6585	−0.6297
G	0.2190	0.1893	−0.0224	−0.0211	0.0962
H	0.5947	0.0918	0.0205	0.0217	0.2310
I	0.8740	−0.1302	−0.0342	−0.0337	6.9436
J	−0.0427	0.1455	0.0733	0.0741	−0.0658
RMS err (%)	1.86	2.95	0.35	0.37	2.11
R	O3N2^b	S_{23}^b	$\frac{[\text{NII}]}{[\text{SiI}]}^b$	$\frac{[\text{SiI}]}{\text{H}\alpha}^b$	$\frac{[\text{NII}]}{\text{H}\alpha}^b$
Z_{\min}	8.23	7.63	7.63	7.63	7.63
Z_{\max}	8.93	8.53	8.53	8.53	8.53
A	10.312	11.033	5.8892	23.370	10.526
B	−1.6575	0.9907	3.1688	11.700	1.9958
C	2.2525	1.5789	−3.5991	7.2562	−0.6741
D	−1.3594	0.4233	1.6394	4.3320	0.2892
E	0.4764	−3.1663	−2.3939	3.1564	0.5712
F	1.1730	0.3666	−1.6764	1.0361	−0.6597
G	−0.2968	0.0654	0.4455	0.4315	0.0101
H	0.1974	−0.2146	−0.9302	0.6576	0.0800
I	−0.0544	−1.7045	−0.0966	0.3319	0.0782
J	0.1891	0.0316	−0.2490	0.0336	−0.0982
RMS err (%)	2.97	0.55	1.19	0.92	0.67

Abbreviation: RMS err, root-mean-square error.

^aValid over $Z_{\min} \leq \log(\text{O}/\text{H}) + 12 \leq Z_{\max}$ and $−3.98 \leq \log(U) \leq −1.98$.

^bWavelengths in angstroms: $[\text{NII}]/[\text{OII}] = \frac{1747.48, 49.52}{1660.66}$, $C_{23}/\text{HeII} = \frac{1906.08 + 2325\text{Å}^c}{1640}$, $C_{23}/\text{HeI} = \frac{1906.08 + 2325\text{Å}^c}{3187}$, $C_{234}/\text{HeI} = \frac{1906.08 + 2325\text{Å}^c + 1548.51}{3187}$, $[\text{NII}]/[\text{OII}] (\text{UV}) = \frac{2139.43}{2470}$, $\text{O3N2} = \frac{[\text{OII}]/\text{H}\beta}{[\text{NII}]/\text{H}\alpha} = \frac{5007/4861}{6584/6563}$, $S_{23} = \frac{[\text{SiI}] + [\text{SiII}]}{\text{H}\alpha} = \frac{6717.31 + 9069 + 9531}{6563}$, $[\text{NII}]/[\text{SiI}] = \frac{6584}{6717.31}$, $[\text{SiI}]/\text{H}\alpha = \frac{6717.31}{6563}$, $[\text{NII}]/\text{H}\alpha = \frac{6584}{6563}$.

^c $[\text{CII}]$ blend (2325b) = $[\text{CII}] \lambda 2323 + [\text{CII}] \lambda 2324 + [\text{CII}] \lambda 2325 + [\text{CII}] \lambda 2326 + [\text{CII}] \lambda 2328$.

Table 3 Metallicity diagnostic calibrations for optical and IR line ratios described in Section 4.5–4.7

Bicubic surface fit: $z = A + Bx + Cy + Dxy + Ex^2 + Fy^2 + Gxy^2 + Hyx^2 + Ix^3 + Jy^3$, where $x = \log(R)$, $y = \log(U)$, $z = \log(\text{O}/\text{H}) + 12$, and $\log(P/k) = 5.0^a$					
R	$\frac{[\text{OII}]}{[\text{Si}]}^b$	$\frac{[\text{OII}]}{\text{H}\beta}^b$	$\frac{[\text{NII}]}{[\text{OII}]}^b$	R_{23}^b	
Z_{\min}	8.23	8.53	7.63	8.53	
Z_{\max}	9.23	9.23	9.23	9.23	
A	12.4894	6.2084	9.4772	9.7757	
B	−3.2646	−4.0513	1.1797	−0.5059	
C	3.2581	−1.4847	0.5085	0.9707	
D	−2.0544	−1.9125	0.6879	−0.1744	
E	0.5282	−1.0071	0.2807	−0.0255	
F	1.0730	−0.1275	0.1612	0.3838	
G	−0.3445	−0.2471	0.1187	−0.0378	
H	0.2130	−0.1872	0.1200	0.0806	
I	−0.3047	−0.1052	0.2293	−0.0852	
J	0.1209	0.0173	0.0164	0.0462	
RMS err (%)	2.52	2.49	2.65	0.42	
R	$\frac{[\text{OII}]\,88\,\mu\text{m}}{[\text{NII}]\,57\,\mu\text{m}}$	$\frac{[\text{OII}]\,55\,\mu\text{m}}{[\text{NII}]\,57\,\mu\text{m}}$	$\frac{[\text{OII}]\,55+88\,\mu\text{m}}{[\text{NII}]\,57\,\mu\text{m}}$	$\frac{\text{Ne}_{23}}{\text{Pfund}}^c$	$\frac{\text{Ne}_{23}}{\text{Humph}}^c$
Z_{\min}	7.63	7.63	7.63	7.63	7.63
Z_{\max}	9.23	9.23	9.23	8.93	8.93
A	8.8463	8.8593	9.7206	−2.3231	−18.7919
B	−2.6206	−2.6454	−3.4595	23.2584	45.1168
C	−0.8838	−0.6418	−0.4186	−0.2016	−1.5507
D	−1.1524	−1.2794	−1.4070	1.9163	2.9812
E	1.3261	1.1269	1.6997	−16.559	−24.953
F	−0.3990	−0.3004	−0.3098	0.3813	0.3725
G	−0.1721	−0.2098	−0.1853	0.0005	0.0071
H	0.3436	0.3968	0.3625	−0.7283	−0.8470
I	−0.5433	−0.5161	−0.5318	4.1178	4.7163
J	−0.0489	−0.0360	−0.0444	0.0395	0.0396
RMS err (%)	1.70	1.69	1.69	1.57	1.81

Abbreviations: Humph, Humphrey- α line of hydrogen; Pfund, Pfund- α line of hydrogen; RMS err, root-mean-square error.

^aValid over $Z_{\min} \leq \log(\text{O}/\text{H}) + 12 \leq Z_{\max}$ and $-3.98 \leq \log(U) \leq -1.98$.

^bWavelengths in angstroms: $\frac{[\text{OII}]}{[\text{Si}]} = \frac{3727.9}{6717.31}$, $\frac{[\text{OII}]}{\text{H}\beta} = \frac{3727.9}{4861}$, $\frac{[\text{NII}]}{[\text{OII}]} = \frac{6584}{3727.9}$, $R_{23} = \frac{4959 + 5007 + 3727.9}{4861}$.

^cWavelengths in μm : $\frac{\text{Ne}_{23}}{\text{Pfund}} = \frac{23}{7.46}$, $\frac{\text{Ne}_{23}}{\text{Humph}} = \frac{23}{12.37}$.

depleted out of gas phase and onto dust grains. The amount of depletion varies from galaxy to galaxy, and silicon may be returned to the gas phase by grain destruction by supernova shocks, which affect magnesium, silicon, and iron (see, e.g., Jones 2000; N. Byler, L. Kewley, J. Rigby, A. Acharyya, in preparation). If dust depletion is known, and it is similar to the depletion used in the photoionization models, the Si_{23} diagnostics can be used at metallicities $\log(\text{O}/\text{H}) + 12 > 8.5$, where they depend little on ionization parameter.

The ideal UV metallicity diagnostic is the $[\text{NII}]/[\text{OII}]$ ratio based on the $[\text{NII}] \lambda 2139$, 43 and $[\text{OII}] \lambda 2470$ lines; this is with the proviso that the $\log([\text{NII}]/[\text{OII}])$ ratio can be determined within an accuracy of ~ 0.05 dex. The $[\text{NII}]$ line has both a primary and a secondary nucleosynthetic origin (e.g., Considère et al. 2000). In primary nucleosynthesis, nitrogen is created for the first time in

the current generation of stars. In secondary nucleosynthesis, nitrogen is created through fusion processes using elements that existed prior to the current generation of stars. For most metallicities [$\log(\text{O}/\text{H}) + 12 > 8.2$], secondary nucleosynthesis is the dominant production mechanism of nitrogen, making nitrogen highly sensitive to the overall metallicity of a galaxy. When combined with the temperature-sensitive $[\text{OII}]$ line, the $[\text{NII}]/[\text{OII}]$ ratio is an extremely strong function of metallicity and is unchanged for ISM pressures typical of star-forming galaxies [$4 < \log(P/k) < 6$]. Because $[\text{NII}]$ and $[\text{OII}]$ have similar ionization potentials, the $[\text{NII}]/[\text{OII}]$ ratio is not sensitive to ionization parameter, and it is relatively insensitive to the presence of a hard radiation field from an AGN or shocks (Kewley & Ellison 2008).

The UV $[\text{NIII}]/[\text{OIII}]$ ratio is a useful UV metallicity diagnostic, but it has a larger dependence on the ionization parameter than $[\text{NII}]/[\text{OII}]$ due to the ionization potentials of N^{++} and O^{++} . This ratio uses the NIII complex of five lines at 1747, 1748, 1749, 1752, and 1754 Å and the $[\text{OIII}]$ doublet at 1660 and 1666 Å. The $[\text{NIII}]/[\text{OIII}]$ ratio is insensitive to ISM pressure variations.

With limited UV wavelength coverage, many galaxies only have absorption lines available in their spectrum. Starburst galaxies produce strong interstellar absorption lines and stellar photospheric and wind lines, some of which are sensitive to the metallicity. Rix et al. (2004), Leitherer et al. (2011), and Zetterlund et al. (2015) provide useful diagnostics for interpreting the absorption lines in a UV spectrum.

4.6. Theoretical Optical Metallicity Diagnostics

The most commonly used theoretical optical metallicity diagnostic is the oxygen R_{23} ratio ($R_{23} = \{[\text{OII}] \lambda\lambda 3727, 9 + [\text{OIII}] \lambda\lambda 4959, 5007\}/\text{H}\beta$), first proposed by Pagel et al. (1979). Many theoretical calibrations of this ratio now exist (e.g., McGaugh 1991, Oey & Shields 2000, Kewley & Dopita 2002, Kobulnicky & Kewley 2004). Skillman (1989) was first to show that the relationship between R_{23} and metallicity depends on ionization parameter. Most subsequent theoretical calibrations included a correction for ionization parameter. The R_{23} ratio is relatively insensitive to the ionization parameter at metallicities above $\log(\text{O}/\text{H}) + 12 > 8.5$ because the $[\text{OIII}]$ and $[\text{OII}]$ lines have opposite dependencies on ionization parameter, which are roughly cancelled out. The R_{23} ratio is sensitive to the ISM pressure for high metallicities [$\log(\text{O}/\text{H}) + 12 > 8.5$] and should be used in conjunction with an ISM pressure diagnostic.

The $[\text{NII}]/[\text{OII}]$ ratio, based on the $[\text{NII}] \lambda 6584$ and $[\text{OII}] \lambda\lambda 3727, 9$ lines, is by far the most reliable metallicity diagnostic in the optical spectrum, with no dependence on ionization parameter, and only marginal dependence on the ISM pressure for $4 \leq \log(P/k) \leq 8$. Several simple optical $[\text{NII}]/[\text{OII}]$ metallicity calibrations have been developed (Jensen et al. 1976, Dopita & Evans 1986, Kewley & Dopita 2002). The $[\text{NII}]/[\text{OII}]$ ratio is highly sensitive to metallicity thanks to the primary and secondary nature of nitrogen plus the temperature sensitivity of the $[\text{OII}]$ line. The optical $[\text{NII}]/[\text{OII}]$ ratio is insensitive to ionization parameter and depends on ISM pressure only at the highest metallicities [$\log(\text{O}/\text{H}) + 12 \geq 9.23$] and at the highest ISM pressures [$\log(P/k) > 8$]. The $[\text{NII}]/[\text{OII}]$ ratio is also the least sensitive optical diagnostic to the presence of an AGN or DIG (Kewley et al. 2006a, Zhang et al. 2017).

Pettini & Pagel (2004) proposed a calibration called O3N2 that uses the $[\text{OIII}]/\text{H}\beta$ and $[\text{NII}]/\text{H}\alpha$ ratios ($\text{O3N2} = [\text{OIII}] \lambda 5007/\text{H}\beta)/([\text{NII}] \lambda 6584/\text{H}\alpha)$. This calibration is based on a combination of auroral metallicities and photoionization models and was developed for spectra of high-redshift galaxies in which flux calibration and extinction correction are difficult. **Figure 9** shows that the O3N2 ratio has a strong dependence on the ionization parameter, varying by 2–3 orders of magnitude across the entire metallicity range. We do not recommend the use of the

O3N2 ratio, especially at high redshift where the ionization parameter is usually significantly larger than in nearby HII regions. Instead, if only the red spectrum is available, we recommend the [NII] $\lambda 6584/\text{H}\alpha$ ratio, which has a smaller (although not negligible) ionization parameter dependence; the [NII]/H α metallicity varies by ~ 1 dex with ionization parameter. Several [NII]/H α calibrations are available (Storchi-Bergmann et al. 1994, Denicoló et al. 2002, Pettini & Pagel 2004). These calibrations are primarily based on the relationship between auroral metallicities and the [NII]/H α line ratio in local HII regions and include a hidden assumption that the ionization parameter of the sample that the calibration is being applied to is the same as the mean ionization parameter of the HII region sample that was used to derive the calibration. For high-redshift galaxies, we recommend the use of an [NII]/H α calibration that includes a correction for ionization parameter, such as that in **Table 2**.

To overcome the ionization parameter problem, Dopita et al. (2016) proposed a composite diagnostic based on the [NII] $\lambda 6574/[\text{SII}] \lambda \lambda 6717, 31$ and [NII]/H α ratios:

$$\log(\text{O}/\text{H}) + 12 = 8.77 + y + 0.45(y + 0.3)^5, \quad 13.$$

where $y = \log[\text{NII}]/[\text{SII}] + 0.264 \log[\text{NII}]/\text{H}\alpha$. The [NII]/[SII] ratio alone has a larger dependence on ionization parameter than the [NII]/[OII] ratio, and is independent of ISM pressure for $4 \leq \log(P/k) \leq 7$, although it has been used in the past as a metallicity diagnostic (Jensen et al. 1976). However, when combined with the [NII]/H α ratio, the Dopita et al. (2016) function becomes relatively insensitive to ionization parameter and ISM pressure over $4 \leq \log(P/k) \leq 7$ and is a promising diagnostic for high-redshift galaxies in which only the red spectrum may be available. (See the sidebar titled Nitrogen-Based Abundance Diagnostics.)

The [SII]/H α ratio ([SII] $\lambda \lambda 6717, 31/\text{H}\alpha$) has been calibrated by Denicoló et al. (2002) and Kewley & Dopita (2002). The [SII] lines are produced in a partially ionized zone at the edge of HII regions. The length of this partially ionized zone is extremely sensitive to the ionization parameter. Therefore, the [SII]/H α ratio is strongly dependent on the ionization parameter and is not a useful metallicity diagnostic unless the ionization parameter is determined to an accuracy of 0.05 dex in $\log(q)$. This ionization parameter dependence can be removed by including the [SIII] line on the numerator, called S_{23} ($S_{23} = \{[\text{SII}] \lambda \lambda 6717, 31 + [\text{SIII}] \lambda \lambda 9069, 9532\}/\text{H}\alpha$) (Vilchez & Esteban 1996, Díaz & Pérez-Montero 2000, Oey & Shields 2000, Kewley & Dopita 2002). Oey & Shields (2000) suggest also including the [SIV] 10.5 μm line on the numerator to create a diagnostic known as S_{234} . **Figure 9** shows that the S_{23} and S_{234} ratios are sensitive metallicity diagnostics, particularly at high pressure, when they become almost linear functions of metallicity, because large pressures strengthen [SIII] and [SIV] at high metallicity.

The [OII] $\lambda \lambda 3727, 9/[\text{SII}] \lambda \lambda 6717, 31$ ratio was proposed by Dopita & Evans (1986) as a metallicity diagnostic. This ratio is less sensitive to the ionization parameter than the [SII]/H α ratio and is useful for metallicities of $\log(\text{O}/\text{H}) + 12 > 8.2$. However, if the full optical spectrum is available to calculate this ratio, we recommend the use of the [NII]/[OII] ratio instead

NITROGEN-BASED ABUNDANCE DIAGNOSTICS

Nitrogen diagnostics are sensitive to the elemental N/O ratio. Our models account for the N/O ratio changing with metallicity owing to the primary and secondary nature of nitrogen. If the N/O ratio is expected to follow the standard primary and secondary curves, then these theoretical nitrogen metallicity diagnostics can be applied. However, if the N/O ratio is expected to be elevated, then tailored models with a given input N/O ratio should be used instead.

because the $[\text{NII}]/[\text{OII}]$ ratio is considerably less sensitive to the ionization parameter and ISM pressure.

The ratios of $[\text{OIII}] \lambda 5007/\text{H}\beta$, $[\text{OIII}] \lambda 5007/[\text{NII}] \lambda 6584$, $[\text{ArIII}] \lambda 7135/\text{OIII} \lambda 5007$, $[\text{SIII}] \lambda 9069/\text{OIII} \lambda 5007$, $[\text{NeIII}] \lambda 3967 + [\text{OII}] \lambda \lambda 3727, 9/\text{H}\gamma$, $[\text{NeIII}] \lambda 3967/[\text{OII}] \lambda \lambda 3727, 9$, and $[\text{OIII}] \lambda 5007/[\text{NeIII}] \lambda 3967$ have been proposed as metallicity diagnostics when limited sets of emission lines are available (Alloin et al. 1979, Dopita & Evans 1986, Charlot & Longhetti 2001, Nagao et al. 2006, Stasińska 2006, Pérez-Montero et al. 2007, Maiolino et al. 2008). Unfortunately, these ratios are relatively insensitive to metallicity, except in the very metal-rich regime $[\log(\text{O}/\text{H}) + 12 > 8.5]$, and are much more sensitive to the ionization parameter than to metallicity. If only a small portion of the spectrum around $[\text{OII}]$ is available (i.e., no $[\text{OIII}]$ or $\text{H}\beta$), we recommend the use of $[\text{OII}]/\text{H}\gamma$ as a metallicity diagnostic, which has a similar relationship to metallicity as that of R_{23} but with a larger ionization parameter dependence.

4.7. Theoretical Infrared Metallicity Diagnostics

IR emission lines were first used to study the abundance variations within the Milky Way, thus avoiding the effects of dust (see Simpson et al. 2004, and references therein). Most strong lines in the IR spectrum are high-ionization species and are unable to provide reliable diagnostics of metallicity without a significant dependence on the ionization parameter (see, e.g., Afflerbach et al. 1997). Fortunately, there are two neon lines ($[\text{NeII}] 12 \mu\text{m}$ and $[\text{NeIII}] 15 \mu\text{m}$) that, when combined with the nearby hydrogen lines (at either $7.46 \mu\text{m}$ or $12.37 \mu\text{m}$), give robust metallicity diagnostics that are independent of the ionization parameter and ISM pressure. We give calibrations for both hydrogen lines because while the Humphrey- α line at $12.37 \mu\text{m}$ is closest in wavelength to the neon lines, the Pfund- α line at $7.46 \mu\text{m}$ is approximately $10\times$ stronger in flux and is more observable.

Nagao et al. (2011) used photoionization models to calibrate the $([\text{OIII}] 57 \mu\text{m} + [\text{OIII}] 88 \mu\text{m})/[\text{NII}] 57 \mu\text{m}$, $[\text{OIII}] 51 \mu\text{m}/[\text{NII}] 57 \mu\text{m}$, and $[\text{OIII}] 88 \mu\text{m}/[\text{NII}] 57 \mu\text{m}$ ratios, taking into account the gas density and ionization parameter. These ratios provide useful diagnostics of metallicity, provided the ionization parameter is taken into account. The $([\text{OIII}] 51 \mu\text{m} + [\text{OIII}] 88 \mu\text{m})/[\text{NII}] 57 \mu\text{m}$ ratio is the most robust to changes in ISM pressure and is independent of ISM pressure for most of the normal range $[4 \leq \log(P/k) \leq 7]$. Calibrations for these metallicities are given in **Table 3**.

The FIR $[\text{NII}] 205 \mu\text{m}/[\text{CII}] 158 \mu\text{m}$ ratio has also been used as a metallicity diagnostic (Nagao et al. 2013). Unfortunately, this ratio is degenerate with metallicity (sometimes being triple-valued), with a 0.3 dex variation in metallicity from the ionization parameter. In addition, $[\text{CII}]$ may also originate from PDRs, which are not included in our photoionization model, and would need to be removed prior to the application of a metallicity calibration. (See the sidebar titled The Metallicity Calibration Scale.)

THE METALLICITY CALIBRATION SCALE

Caution: All emission-line metallicity calibrations suffer from systematic discrepancies of up to 0.7 dex in $\log(\text{O}/\text{H}) + 12$ (Kewley & Ellison 2008). Fortunately, relative metallicities calculated with the same calibration are usually (though not always) accurate to within 0.03 dex on average. Nevertheless, we recommend the use of three or more metallicity calibrations (preferably with different line ratios and by different authors), where possible, to check how the science results are influenced by the metallicity calibrations used.

5. EXCITATION SOURCES IN GALAXY EVOLUTION STUDIES

Understanding the relative fraction of star formation, AGNs, and shocks in galaxies has been a hot topic of research for several decades. We now know that many AGNs in local galaxies are often surrounded by circumnuclear regions of star formation; around half of nearby, optically selected Seyfert 2 galaxies host a nuclear starburst (e.g., Cid Fernandes et al. 2001; Veilleux et al. 2003, 2005). Star formation may be related to AGN fueling; AGN activity is observed systematically after stellar winds and supernovae in the nuclear regions have subsided (Wild et al. 2010), and AGN-driven winds may also quench star formation (e.g., Gabor et al. 2010).

Shock excitation in galaxies can be produced by many phenomena, including galactic-scale outflows, galaxy interactions, ram-pressure stripping, and AGN-related activity such as jets. Mergers can produce widespread shocks throughout galaxies that significantly affect the emission-line spectrum of a galaxy at both kiloparsec scales and subkiloparsec scales within a galaxy (Medling et al. 2015).

Many galaxies show evidence for wind-induced shocks. Our Milky Way has strong shocks near the Galactic center from stellar winds associated with WR stars (Simpson et al. 2007). Some galaxies have massive winds with outflow velocities of up to several hundred kilometers per second (e.g., Strickland et al. 2004, Veilleux et al. 2005, Sharp & Bland-Hawthorn 2010, Ho et al. 2016). These superwinds are produced by either (*a*) a combination of supernovae and wind-blown bubbles from massive stars (starburst-driven winds) or (*b*) outflows associated with the accretion of material onto AGNs (AGN-driven winds) [see Veilleux et al. (2005) for a review]. Starburst-driven winds may eject gas into the galactic halo, which can subsequently fall back onto the disk, like a galactic fountain. Powerful starburst winds may also drive gas outside galaxies and into the circumgalactic medium (Heckman et al. 2017). Integral field spectroscopy shows that starburst-driven winds are common in local disk galaxies of all stellar masses (Ho et al. 2016), although winds appear to be more common in galaxies with large star-formation surface densities and in galaxies that have experienced recent bursts of star formation (Heckman 2003).

Galactic-scale winds are readily observed with spectroscopy in edge-on galaxies because winds often produce conical structures with limb-brightening along the edges of expanding X-ray bubbles that entrain ambient cold gas. The wind bubbles expand supersonically, and shock waves excite emission lines from the UV through the IR. Fast shocks have a photoionizing precursor that produces strong high-ionization lines, whereas the hard radiation field from the shock front itself produces an extended partially ionized zone where low-ionization lines such as [O I], [N I], and [S II] are observed. Shocked regions may also have higher electron densities than the surrounding nonshocked medium (Ho et al. 2014).

Starburst-driven winds are commonly observed at high redshift ($z > 1$) because SFRs ($1\text{--}100\text{ M}_{\odot}\text{ year}^{-1}$) are higher than in the local Universe. Winds are observable at high redshift through either absorption or emission lines (e.g., Weiner et al. 2009, Steidel et al. 2010, Chisholm et al. 2018, Davies et al. 2019, Rigby et al. 2018). Davies et al. (2019) used emission lines to show that faster outflows with larger mass-loading factors are associated with higher star-formation surface densities at $2.0 < z < 2.6$, similar to local galaxies.

The field of excitation source diagnostics is currently in flux (no pun intended!). Many emission-line diagnostics have been developed to determine the dominant excitation source in galaxies, but these diagnostics were primarily developed for single-aperture spectroscopy with relatively small (~ 1 kpc) apertures. Recently, wide-area integral field spectroscopy and high spatial resolution integral field spectroscopy have revolutionized our ability to identify and separate multiple excitation sources in the same galaxy. In particular, the Multi Unit Spectroscopic Explorer and Keck Cosmic Web Imager instruments are likely to play a major role in our understanding of the power sources across nearby galaxies in the near future.

Theoretical models of excitation sources have been essential for understanding the relationship between specific line ratios and the fundamental properties of excitation sources. Major advances are currently being made in modeling the spectra from star-forming galaxies, AGNs, and shocks. It is now possible to model the spectra from galaxies that contain a mixture of excitation sources, although the models are not yet fully self-consistent.

Given these ongoing and exciting changes, we briefly review the current diagnostics in use for single-aperture spectroscopy in the UV, optical, and IR spectral regions. We then describe some of the most promising diagnostics for use with integral field spectroscopy. We end with an overview of the recent advances in excitation source modeling. Because these advances are occurring rapidly, and we expect further advances to be made in the coming 2–3 years, we refrain from providing new excitation-class diagnostics at this time.

5.1. Excitation Sources Using Single-Aperture Spectroscopy

The most common method to determine the excitation sources of galaxies is using ratios of strong optical emission lines. The excitation diagnostic diagram of $[\text{OIII}] \lambda 5007/\text{H}\beta$ versus $[\text{NII}] \lambda 6583/\text{H}\alpha$ is known as the Baldwin–Phillips–Terlevich (BPT) diagram, after Baldwin et al. (1981), who proposed the use of the $[\text{OIII}] \lambda 5007/\text{H}\beta$, $[\text{NII}] \lambda 6583/\text{H}\alpha$, and $[\text{OI}] \lambda 6300/\text{H}\alpha$ ratios for distinguishing among normal HII regions, planetary nebulae, and objects photoionized by a harder radiation field. HII regions and star-forming galaxies form a clean sequence on the BPT diagram from low metallicity to high metallicity. This sequence is known as the HII region abundance sequence or the star-forming galaxy abundance sequence (**Figure 10**). The position of this sequence can be affected by the metallicity of the ionized gas, the ISM pressure, the hardness of the ionizing radiation field, and the ionization parameter, as illustrated in **Figure 10b**. Due to these changes, the position of the star-forming abundance sequence on the BPT diagram is expected to change with redshift (Kewley et al. 2013).

Seyfert galaxies and shocks lie at large $[\text{OIII}]/\text{H}\beta$ ratios on the BPT diagram. It is well known that AGNs reside in the most massive and most metal-rich galaxies (e.g., Thomas et al. 2018a). Therefore, an AGN contribution raises the $[\text{NII}]/\text{H}\alpha$ ratio above the star-forming abundance sequence, allowing clean separation of galaxies containing an AGN. The position of AGNs on the BPT diagram is extremely sensitive to metallicity and will move toward smaller $[\text{NII}]/\text{H}\alpha$ ratios at low metallicity. Low-metallicity AGNs are extremely rare in local galaxies (Groves et al. 2006), but this is likely to change at high redshift, causing the AGN region to move toward, or even overlap with, the star-forming abundance sequence (Kewley et al. 2013). The series of galaxies joining the star-forming galaxy abundance sequence and the AGN region is commonly referred to as a mixing sequence. Galaxies that lie along the mixing sequence are commonly referred to as composites or transition objects. Composites may contain a mixture of star formation, shock excitation, and/or AGN activity.

Kennicutt & Keel (1984) and Keel (1983) extended the BPT classification scheme to include the $[\text{SiII}] \lambda\lambda 6716, 6731/\text{H}\alpha$ line ratio, which is also sensitive to the hardness of the ionizing radiation field. Osterbrock & Pogge (1985) and Veilleux & Osterbrock (1987) derived the first semiempirical classification lines to be used with the standard optical diagnostic diagrams. The full suite of standard optical diagnostic diagrams based on the $[\text{OIII}]/\text{H}\beta$, $[\text{NII}]/\text{H}\alpha$, $[\text{SiII}]/\text{H}\alpha$, and $[\text{OI}]/\text{H}\alpha$ line ratios are commonly known as Veilleux–Osterbrock (VO) diagrams (Veilleux & Osterbrock 1987).

The first purely theoretical optical classification scheme was developed by Kewley et al. (2001a) using a combination of stellar population synthesis, photoionization, and shock models to derive a maximum starburst line as an upper limit for star-forming galaxies on the BPT diagrams. Galaxies that lie above this line cannot be explained by any combination of pure starburst models and must

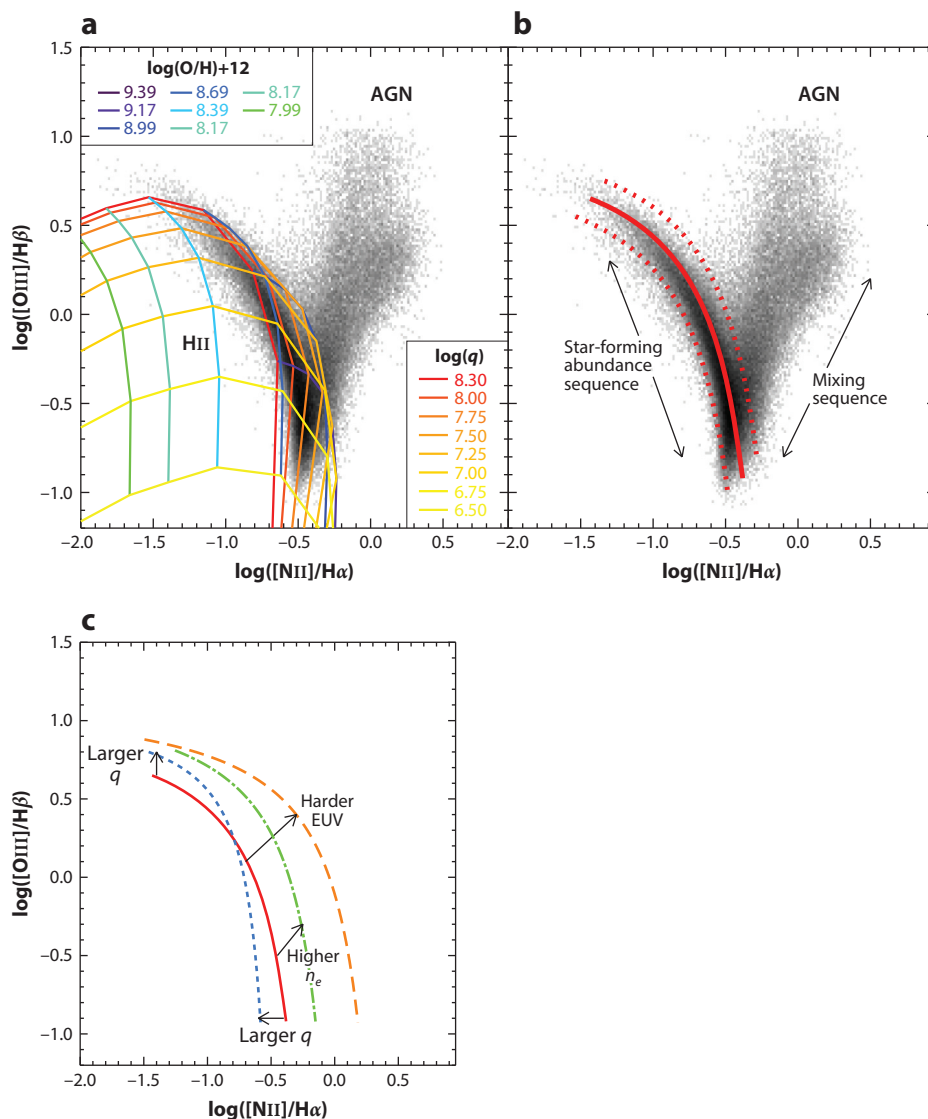


Figure 10

The [NII]/H α versus [OIII]/H β optical diagnostic diagram for the SDSS galaxies analyzed by Kewley et al. (2006b). (a) The colored curves show theoretical photoionization model fits to the star-forming abundance sequence. (b) The red solid curve shows the mean star-forming sequence for local galaxies. The shape of the red solid curve is defined by our theoretical photoionization models, whereas the position is defined by the best fit to the SDSS galaxies. The ± 0.1 dex curves (dashed lines) represent our model errors and contain 91% of the SDSS star-forming galaxies. (c) An illustration of the effect of varying different galaxy parameters on the star-forming galaxy abundance sequence in the [NII]/H α versus [OIII]/H β diagnostic diagram. Abbreviations: AGN, active galactic nucleus; EUV, extreme UV radiation field; HII, HII region-like spectra; n_e , electron density; q , ionization parameter in centimeters per second; SDSS, Sloan Digital Sky Survey.

SCHEME APPLICABILITY

Caution: Classification lines derived for local galaxies may not be applicable to high-redshift galaxies or spatially resolved regions within galaxies because the ionization parameter, the radiation field shape (due to the age of the stellar population) and/or the ISM pressure may be different from that in the nuclear spectra of local galaxies.

contain a significant fraction (30–50%) contribution from an AGN or shock excitation. To produce samples containing purely star-forming galaxies, Kauffmann et al. (2003) shifted the Kewley et al. model shape to fit a boundary to the SDSS star-forming galaxy sequence. Stasińska et al. (2006) subsequently used photoionization models to derive a new theoretical classification line for classifying local star-forming galaxies. (See the sidebar titled Scheme Applicability.)

The SDSS sample enabled a significant advance in the optical classification of galaxies because the large number of galaxies (~45,000) revealed for the first time clearly formed branches on the $[\text{SiII}]/\text{H}\alpha$ versus $[\text{OIII}]/\text{H}\beta$ and $[\text{OI}]/\text{H}\alpha$ versus $[\text{OIII}]/\text{H}\beta$ diagrams (Kewley et al. 2006b). On these two diagrams, one branch joins the star-forming galaxy abundance sequence to the Seyfert region, and the other branch joins the star-forming galaxy abundance sequence to the region where low ionization nuclear emission regions (LINERs) are located. The two branches are not observed on the BPT diagram, because the $[\text{NII}]/\text{H}\alpha$ ratio does not provide sufficient separation between the two branches, which overlap.

LINER emission can be produced by different emission mechanisms [see, e.g., Ho (2008) and Yan & Blanton (2012) for an overview]. Some LINER emission is associated with low-luminosity AGNs. These LINERs are identified with small (<1 kpc) nuclear apertures (Heckman 1980, Filippenko 1985, Ho et al. 1993), and they have properties consistent with gas ionized by the radiation from an inefficiently accreting, low-luminosity supermassive black hole (Ho et al. 1996, Constantin & Vogeley 2006). LINERs in the SDSS observed through ~ 1 kpc apertures follow the same relation in Eddington ratio as Seyfert galaxies but with a harder ionizing radiation field and a lower ionization parameter (Kewley et al. 2006b). Further evidence of AGNs in LINERs is found in the radio spectrum. More than 50% of nuclear LINERs have parsec-scale radio nuclei, with implied brightness temperatures $\gtrsim 10^7$ K, and subparsec jets (Heckman 1980, Nagar et al. 2005). High spatial resolution spectra and X-ray studies suggest that the ionizing radiation from the accretion onto the low-luminosity black hole produces insufficient ionizing radiation to produce the line ratios observed in LINERs (Flohic et al. 2006). Shocks by jets or other outflows may be required to power this LINER emission in addition to the emission from the AGN accretion disk (Molina et al. 2018).

LINER-type emission is also seen in the extended gas outside the nuclear regions (i.e., >1 kpc) (Phillips et al. 1986, Goudfrooij et al. 1994). Extended LINER emission can be produced by shocked regions produced by galactic-scale outflows (Dopita & Sutherland 1995; Ho et al. 2014, 2016). An evolved stellar population, such as pAGB stars can also produce extended LINER emission (e.g., Binette et al. 1994, Sarzi et al. 2010, Yan & Blanton 2012, Singh et al. 2013, Hsieh et al. 2017). The term LINER is not appropriate for these extended regions, because LINERs were originally defined as being “nuclear” on very small scales. An alternative name, LIER (low-ionization emission-line regions) has been suggested by some authors (Belfiore et al. 2016), but this definition can include both extended shocks and evolved stellar populations as power sources. In particular, the spatial and spectral resolution of many large integral field unit (IFU) surveys is insufficient to unequivocally rule out shocks from galactic-scale winds as the power source for extended LINER emission.

To avoid continued confusion in the literature regarding the power source in LINERs, we suggest that authors avoid the use of terms like LINER and LIER. We advocate the use of more descriptive power source terms with resolution scales, such as “low-luminosity AGNs over $<200 \text{ h}^{-1} \text{ pc}$ scales,” “galactic-scale wind shocks over a 1-kpc scale,” and “post-AGB emission-line regions over 1-kpc scales.” Where aperture size or spatial resolution cannot distinguish between potential power sources, this should be made clear. Furthermore, more than one of these power sources may exist in a galaxy. Aperture size, spectral resolution, and emission-line S/N ratios influence which excitation source is deemed responsible for the low-ionization emission.

Optical diagnostics are not ideal for separating excitation sources if shock emission is suspected. **Figure 11a** shows the location of our pressure models, the fast shock models of Allen et al. (2008), the slow shock models of Rich et al. (2011), and the AGN models of Thomas et al. (2016, 2018b) on the three standard optical diagnostic diagrams. Although the stellar photoionization models and the AGN models are separated, the fast and slow shock models lie in the same region as the AGN models. Mixing sequences between star formation and shocks likely coincide with mixing sequences between star formation and AGNs. The shock models lie predominantly away from the pure star-forming regions, but there is some overlap on the $[\text{NII}]/\text{H}\alpha$ versus $[\text{OIII}]/\text{H}\beta$ diagram of shock models with the star-forming sequence. Replacing the $[\text{OIII}]/\text{H}\beta$ ratio with $[\text{OIII}]/[\text{OII}]$ or $[\text{NeIII}]/[\text{OII}]$ improves the situation a little (**Figure 11b,c**), but there is still overlap among the power sources.

Some diagnostics in the UV are more promising. UV excitation source diagnostics were first developed to understand the UV spectra from high- z radio galaxies, where both shocks and AGNs may contribute to the spectrum (Villar-Martin et al. 1996, 1997). Unlike the optical spectrum, the UV contains a large suite of high-ionization emission lines that are stronger in shocked regions than in photoionized regions. Shocks drive high-temperature gas that produce large quantities of high-ionization lines such as $[\text{CIV}] \lambda 1549$ [see Groves et al. (2004) for an overview]. Many UV diagnostic diagrams have been proposed to separate (a) AGNs from shocks, (b) AGNs from star formation, or (c) star formation from shocks (Allen et al. 1998, Best et al. 2000, Moy & Rocca-Volmerange 2002, Groves et al. 2004b, Feltre et al. 2016, Jaskot & Ravindranath 2016). In particular, Feltre et al. (2016) investigates many UV diagnostic diagrams with current models.

The $\text{CIII}]/\text{HeII}$ ratio from the $\text{CIII}] \lambda 1909$ and $\text{HeII} \lambda 1640$ lines is one of the most useful discriminants between star formation and harder ionizing sources. The $\text{HeII} \lambda 1640$ line is weak in most star-forming galaxies, but even a $\text{CIII}]/\text{HeII}$ lower limit is useful for identifying star-formation-dominated galaxies. Ratios of $\log(\text{CIII}]/\text{HeII}) > 1$ are unambiguously produced by purely star-forming models. Shock and AGN models usually produce significantly smaller $\text{CIII}]/\text{HeII}$ ratios because harder radiation fields produce more HeII as well as more ionizations from C^{++} into C^{+++} . The $\text{CIII}]/\text{HeII}$ ratio is insensitive to changes in the ISM pressure.

The highest-ionization UV lines, like $\text{Nv} \lambda 1240$ and $[\text{Nv}] \lambda 3426$, are not typically produced in HII regions, and the presence of these lines are useful for diagnosing a harder ionizing radiation field than pure star formation. However, the ratio of $[\text{Nv}]$ to the other strong UV lines produces significant overlap between the AGNs and shock models and is not a useful diagnostic to separate AGNs from shocks.

Resonance lines like $[\text{CIV}]$ are commonly used in the UV spectrum, but radiative transfer of resonance lines is approximated with an escape probability that takes into account the opacity effect of dust, and these assumptions introduce additional uncertainties into the resulting model fluxes of $[\text{CIV}]$ (e.g., N. Byler, L. Kewley, J. Rigby, and A. Acharyya, in preparation).

A major disadvantage to the UV lines, and sometimes the optical lines, is that galaxies containing dust-obscured AGNs can be misclassified as purely star-forming galaxies. IR emission lines can identify AGNs in the presence of dust. Many useful line ratios are now in use for discriminating

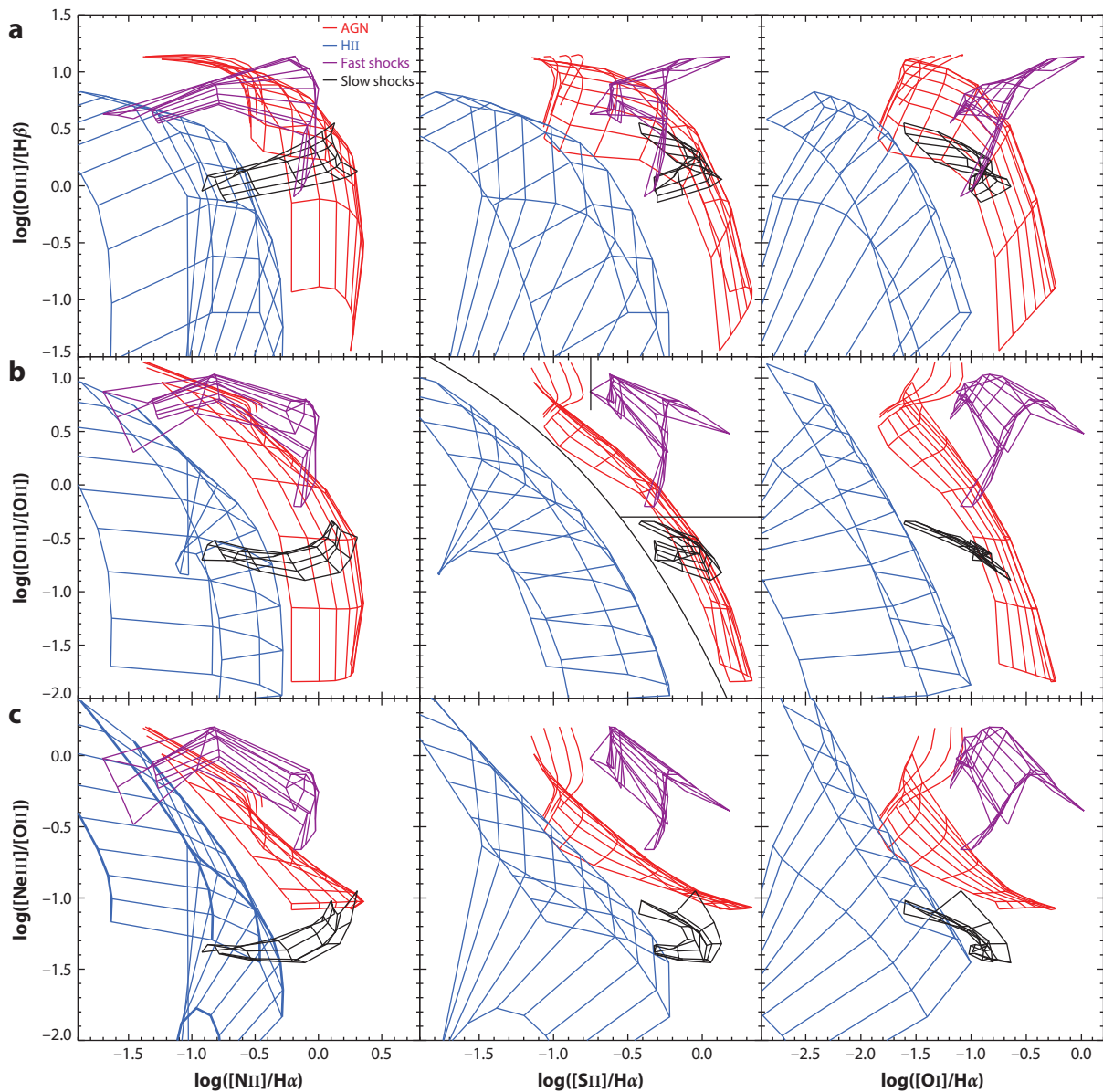


Figure 11

(a) The standard optical diagnostic diagrams showing the location of our pressure stellar photoionization models (*blue*), AGN photoionization models (*red*), fast shock models (*purple*), and slow shock models (*black*). (b) The standard optical diagnostic diagrams but with $[\text{OIII}]/\text{H}\beta$ replaced by $[\text{OIII}] \lambda 5007/[\text{OII}] \lambda \lambda 3727, 9$. (c) The standard optical diagnostic diagrams but with $[\text{OIII}]/\text{H}\beta$ replaced by $[\text{NeIII}] \lambda 3869/[\text{OII}] \lambda \lambda 3727, 9$. Abbreviation: AGN, active galactic nucleus.

AGNs from star formation in the IR spectrum (e.g., Genzel et al. 1998, Fernández-Ontiveros et al. 2016). Lutz (2014) discusses use of the IR diagnostics for galaxy evolution.

The ratio of high-ionization to low-ionization fine structure lines such as the $[\text{NeV}] 14.3, 24.3 \mu\text{m}/[\text{NeII}] 12.8 \mu\text{m}$ and $[\text{OIV}] 25.9 \mu\text{m}/[\text{NeII}] 12.8 \mu\text{m}$ line ratios discriminate between starbursts and AGNs, thanks to the harder radiation field from an AGN (Genzel et al. 1998). The

[Nev] and the [Oiv] lines have ionization potentials of >54 eV and are produced in the high-pressure narrow-line regions surrounding the AGNs [see Fernández-Ontiveros et al. (2016) for a discussion].

The IR continuum and polycyclic aromatic hydrocarbon (PAH) features can also provide useful diagnostics for distinguishing the excitation source. PAHs are destroyed by the harder radiation field associated with an AGN. Many IR diagnostics use PAH features, including those by Genzel et al. (1998), Laurent et al. (2000), Spoon et al. (2007), and Armus et al. (2007).

Some IR excitation diagnostics can simultaneously trace other properties of the galaxies. For example, Spoon et al. (2007) combined the $6.2\text{ }\mu\text{m}$ PAH emission feature and the strength of the $9.7\text{ }\mu\text{m}$ silicate absorption line to produce a sophisticated diagram that includes the effect of dust obscuration and geometry as well as excitation source. The [Oiv] $25.9\text{ }\mu\text{m}$ /[Oiii] $88\text{ }\mu\text{m}$ versus [Neiii] $15.6\text{ }\mu\text{m}$ /[Neii] $12.8\text{ }\mu\text{m}$ diagram proposed by Fernández-Ontiveros et al. (2016) is sensitive to both the excitation source and the metallicity of the gas through the neon lines.

Overall, the current suite of UV–IR excitation diagnostics is extensive and useful for diagnosing the power source in galaxies that contain a single power source. However, many galaxies contain multiple power sources, and single-aperture spectroscopy is able to neither unambiguously identify multiple power sources within an aperture nor estimate the relative contribution of the excitation sources to each emission line. Integral field spectroscopy overcomes this problem.

5.2. Excitation Sources Using Integral Field Spectroscopy

Different power sources can be unambiguously identified using high spectral and spatial resolution optical integral field spectroscopy, as long as the effects of beam smearing (emission from one pixel contributing to emission in another pixel) have been accounted for. The standard optical diagnostic diagrams can be used in conjunction with photoionization models to determine the fractional contribution from an AGN and star formation to each emission line, for every spaxel with sufficient S/N. If a galaxy displays a clean mixing sequence from the star-forming galaxy sequence to the AGN region on the BPT diagram, the relative distance along the sequence gives the fractional contribution from star formation and the AGN. If this fractional contribution is used with star formation and AGN photoionization models, the relative contribution to each emission line can be determined. Examples are discussed by Davies et al. (2014b,a; 2016) and D’Agostino et al. (2018). Davies et al. (2014a) showed that by using this method, the SFR can be successfully derived from the $\text{H}\alpha$ line after the AGN fractional contribution has been removed and that the bolometric luminosity of the AGN can be successfully estimated after the star-formation contribution has been removed from the [Oiii] emission line. This method holds substantial promise for future work investigating the starburst–AGN fraction as a function of redshift and environment, particularly if a similar method can be applied in the IR spectrum to overcome the effects of dust.

Separating shocks from star-forming regions can also be accomplished using high spectral resolution integral field spectroscopy. This method takes advantage of the impact of shocks on the gas kinematics. Gas excited by thermal shocks produces emission lines with velocity dispersions (i.e., emission-line widths in velocity units) around the mean shock velocity. These shocked components often present as separate kinematic components in integral field data, and show as broad lines, usually underlying the narrow lines typical of star-forming regions. Both galactic wind shocks and merger-induced shocks are known to produce separate kinematic components to the emission lines that have velocity dispersions of $150\text{--}500\text{ km s}^{-1}$, which is significantly larger than the velocity width of Hii regions or gas ionized by evolved stellar populations (both typically $<40\text{ km s}^{-1}$). With this method, shocks have been successfully separated from star-forming regions in merging

SHOCK CLASSIFICATION

With high spectral resolution integral field spectroscopy, shocked regions can be unambiguously identified when the following criteria are met:

1. The velocity dispersion distribution is bimodal.
2. The velocity dispersion of the broad component is greater than 80 km s^{-1} .
3. The velocity dispersions correlate with shock-sensitive emission-line ratios, such as $[\text{NII}]/\text{H}\alpha$, $[\text{SII}]/\text{H}\alpha$, or $[\text{OI}]/\text{H}\alpha$.
4. The line ratios are consistent with the predictions from shock models.

galaxies (Rich et al. 2010, 2011, 2015) and in isolated spiral galaxies (Ho et al. 2014, 2016). (See the sidebar titled Shock Classification.)

The correlation between velocity dispersion and line ratios such as $[\text{NII}]/\text{H}\alpha$ or $[\text{SII}]/\text{H}\alpha$ (see Rich et al. 2010) is critical for unambiguous identification of shocks because neither beam smearing nor aged stellar populations can produce correlations between velocity dispersion and emission-line ratios. High spectral resolution of $30\text{--}50 \text{ km s}^{-1}$ at $\text{H}\alpha$ is typically required to identify shocks with this method. Unfortunately, the spectral and spatial resolution of many current large IFU surveys are insufficient to separate evolved stellar populations from shock emission using velocity dispersion.

Separating shocks from both star formation and AGNs is significantly more difficult because the AGN narrow-line region also produces a kinematic component to the emission-line profiles that may have velocity dispersions similar to (or larger than) shocks. However, separation of all three power sources is now possible, using the spatial information afforded by integral field spectroscopy in conjunction with the emission-line ratios and velocity dispersion information. A 3D diagnostic diagram that uses radius as the x -axis, velocity dispersion as the y -axis, and a combined line ratio as the z -axis is able to separate all three power sources as long as two of the power sources are extended beyond the nucleus (D'Agostino et al. 2019). Any of the BPT or VO diagnostic line ratios can be used in this 3D diagram, and we recommend the use of multiple diagnostic line ratios for verification. **Figure 12** gives an example of the 3D diagram to separate shocks, AGNs, and star formation from D'Agostino et al. (2019). This diagram utilizes the fact that gas excited by an AGN can be identified by its central position within galaxies as well as its large velocity dispersion, which is typically $>300 \text{ km s}^{-1}$. Additional multiwavelength information such as hard-X-ray emission or a compact steep spectrum radio source can help to confirm the AGN identification. In **Figure 12**, at low line ratios and low velocity dispersions, star formation dominates. At large line ratios, large velocity dispersions, and large radii, shock emission dominates, whereas at large line ratios, large velocity dispersion, and small radii, the AGN dominates, producing a double-peaked fork shape that is two mixing sequences: (a) a star formation–shock mixing sequence and (b) a star formation–AGN mixing sequence. If this 3D diagram is combined with theoretical photoionization and shock models, one could potentially derive the fractional contribution from star formation, shocks, and AGNs to each spaxel and each emission line as long as the spectral resolution allows clean separation between the star-forming, shock, and AGN kinematic components.

5.3. Excitation Source Modeling

Modern excitation source diagnostics rely on stellar evolution synthesis, photoionization, and shock models both to (a) predict the regions of the diagrams where each power source is likely to

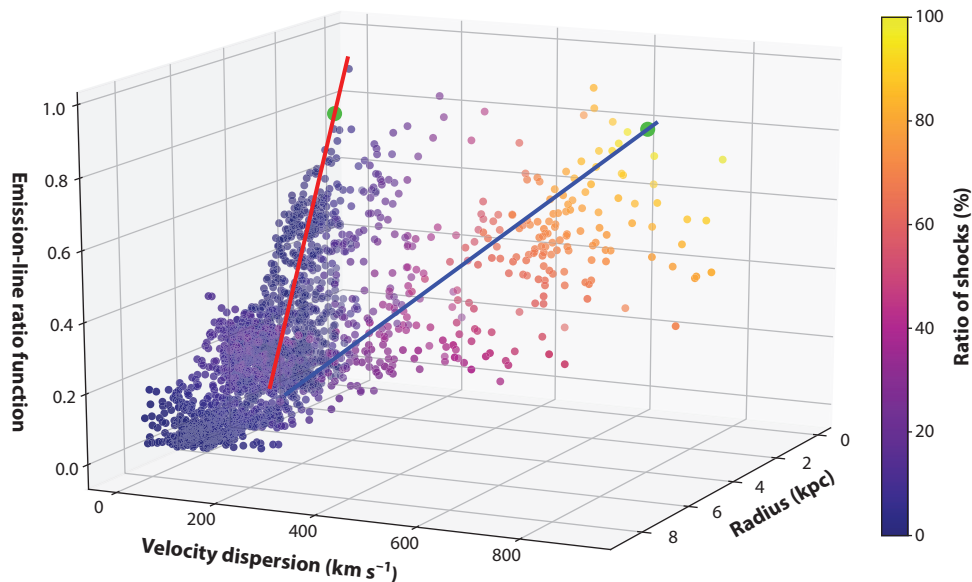


Figure 12

A 3D diagnostic diagram showing how star formation, AGNs, and shocks can be separated using a combination of emission-line ratios, velocity dispersion, and radial information. The colored circles are spaxels in NGC 1068, color coded according to shock fraction as shown in the legend. The red and blue lines indicate the direction of the starburst-AGN and starburst-shock mixing sequences, respectively. Data from D’Agostino et al. (2018).

be located and (b) understand the impact of star formation, AGNs, and shock properties on the predicted locations of the power sources on the diagnostic diagrams.

Most stellar evolutionary synthesis models are based on single stars. Single-star models all produce a relatively soft ionizing radiation field, with extremely similar (to within ~ 0.15 dex) emission-line predictions for the key optical diagnostic ratios (D’Agostino et al. 2019). Single-star stellar evolution models contain too few ionizing photons above >40 eV to reproduce the observed strength of key UV, optical, and IR emission lines, particularly at low metallicity. This problem was identified through comparisons between models and observations for the optical $[\text{SiII}]/\text{H}\alpha$ and $[\text{OI}]/\text{H}\alpha$ ratios in local galaxies (Kewley et al. 2001b), the $[\text{NIII}]$ line strength (e.g., Sellmaier et al. 1996), and the IR $[\text{OIV}] 25.9 \mu\text{m}/[\text{OIII}] 88 \mu\text{m}$ ratio (Fernández-Ontiveros et al. 2016). The lack of ionizing photons has been referred to as the $[\text{NIII}]$ problem, but it affects a substantially larger number of lines than just $[\text{NIII}]$.

Several methods have been proposed to produce more ionizing photons above >40 eV, including stellar rotation and binary star models. Stellar tracks calculated with stellar rotation produce a harder ionizing radiation field, which remains hard for longer timescales than stellar tracks without rotation included (Levesque et al. 2012). There are multiple reasons for this effect. Rotation causes stars to spend more of their lifetimes on the main sequence because helium enhancement causes rotating stars to have both hotter effective temperatures and larger luminosities than non-rotating stars (Leitherer 2008, Leitherer et al. 2014). Rotational mixing also extends the WR phase by causing more stellar mass loss, lowering the minimum mass for a WR star (Georgy et al. 2012). An entire population of rotating stars will contain a larger fraction of WR stars than a nonrotating population, and these WR stars will be longer lived. Stellar evolution synthesis models now include rotation, although a full suite of rotation models across the full metallicity range is still lacking.

Binary star models produce similar effects on the ionizing spectrum as models with rotation. Binary star models can produce a harder ionizing radiation field particularly at low metallicity (Xiao et al. 2018). Binary stars remove the hydrogen envelope of some red supergiants to form WR stars, which make a significant contribution to the ionizing radiation field, resulting in a radiation field that remains harder for a longer period of time than in single-star models (Eldridge & Stanway 2009). To reproduce the observed strengths of UV lines in high-redshift galaxies, binary star models require a subsolar metallicity and a depleted carbon-to-oxygen ratio (Eldridge & Stanway 2012). These advances, in combination with advances in stellar atmosphere modeling, may resolve the [NeIII] problem and provide more robust predictions of the UV–IR spectral lines for the next generation of excitation source diagnostics.

Shock models have also undergone significant advances recently. Fast shocks ($v > 500 \text{ km s}^{-1}$) produce strong high-ionization lines such as [OIII] (Allen et al. 1998, 2008), whereas slow shocks produce relatively weak high-ionization lines but strong low-ionization species such as [SII] and [NII] (Rich et al. 2011, 2015). This difference occurs because fast shocks produce a photoionizing precursor that produces significant ionization in front of the shock. Slow shocks are unable to drive a precursor (Sutherland & Dopita 2017). Previously, shocks and precursors were run separately, with several iterations of shock and precursor models to ensure that the ionization state of the precursor gas is reliable. The latest shock models include self-consistent treatment of shocks and their photoionizing precursor and the latest atomic data, and the shock models now span a significantly larger range of velocity (Sutherland & Dopita 2017). The new generation of shock models is currently only available for solar metallicity. When available, the full suite of metallicities will enable one to derive shock properties, such as the shock velocity and the metallicity in the shocked region using emission-line diagnostics.

To derive reliable excitation source diagnostics, theoretical modeling of pAGB stars is required to identify where pAGB stars contribute to the emission-line ratios. Theoretical modeling of pAGB star emission assumes that the radiation field produced by the pAGB stars ionizes nearby gas with a close to 100% covering fraction. Under these assumptions, pAGB star models can produce LINER emission spectra, although Yan & Blanton (2012) suggest that a larger ionization parameter is required than current pAGB models are able to produce. We expect further advances in pAGB star modeling in the near future, with the combination of new high spatial and spectral resolution integral field spectroscopy and pAGB models.

6. DIFFUSE IONIZED GAS

The ionizing radiation produced by the star clusters is only partially absorbed by the HII regions. Superbubble models suggest that the combined effects of supernovae, stellar winds, and large-scale ionization by OB associations create a complex density and ionization structure that can be porous to ionizing radiation, allowing some radiation to escape (Shields 1990). The escaped radiation ionizes the diffuse gas outside HII regions, both in the disk and up to several kiloparsecs above the disk. The gas that receives leaked ionizing radiation from HII regions is referred to as DIG.

The DIG has been studied extensively in the Milky Way (Minter & Balser 1997, Rand 1998, Madsen et al. 2006) (referred to as the warm ionized medium), and more recently in nearby galaxies (e.g., Zhang et al. 2017, Poetrodjojo et al. 2018, and references therein). These studies suggest that the radiation in the DIG may come from a variety of sources. Martin (1997) showed that the DIG has a radial gradient that is consistent with the dilution of radiation from a centralized source, indicating that the dominant excitation mechanism of the DIG is photoionization by the radiation from massive stars. However, in some galaxies, 30–50% of the DIG emission may come

from shock excitation (Martin 1997, Ramirez-Ballinas & Hidalgo-Gómez 2014), and a very minor component ($<20\%$ of $H\alpha$) may come from dust-scattered radiation (Barnes et al. 2015).

The absorption by the HII region produces a hard residual ionizing radiation field producing strong diffuse gas emission in low-ionization species, such as $[OI]$, $[NII]$, $[CII]$, and $[SII]$, and weak emission in high-ionization species such as $[OIII]$ [see reviews by Rand (1998), Mathis (2000), and Haffner et al. (2009)]. The DIG may contribute between 10–50% of the $H\alpha$ emission but may contaminate the $[NII]$, $[SII]$, and other low ionization lines up to $2\text{--}3\times$ more (Madsen et al. 2006, Oey et al. 2007, Blanc et al. 2009). As shown by Zhang et al. (2017), the $[NII]/[OI]$ ratio is relatively unaffected by the DIG, on average. The $[OIII]/[OI]$ ratios are also likely to be relatively unaffected by the DIG.

The line ratios of the DIG have important implications for estimates of the electron density, ISM pressure, ionization parameter, metallicity, and excitation source in galaxies. In spectra in which HII regions are unresolved, estimates of the electron density or ISM pressure using the $[SII]$ doublet are likely to be strongly contaminated by the DIG and are likely to yield density and pressure estimates that are larger than the true values. The DIG is likely to introduce scatter in estimates of the ionization parameter using $[OIII]/[OI]$, but the average ionization parameter will be close to the true value. The DIG will cause the metallicity to be overestimated if the $[NII]/H\alpha$ and $[SII]/H\alpha$ (or $[NII]/[SII]$) ratios are used, but the metallicity is likely to be close to the true (strong-line) value if the $[NII]/[OI]$ or R_{23} ratios are used. When the standard optical diagnostic diagrams are used to classify excitation source, strong contamination from the DIG may cause galaxies to be misclassified as LINERs.

One of the most serious consequences of the DIG is its effect on metallicity gradient measurements. In face-on spiral galaxies, the DIG contributes more at larger radii than at smaller radii, causing metallicity gradients to appear significantly flatter than the true gradient. Spatial resolution of the scales of the HII regions (40–100 pc) is required to overcome this problem. This has important implications for studies of metallicity gradients with large IFU surveys or at high redshift, where the spatial resolution is typically ~ 1 kpc.

7. CHALLENGES

Galaxy evolution studies require reliable emission-line diagnostics. The current challenges to theoretical modeling of galaxy spectra and observations of galaxies are opportunities to improve our estimates of fundamental galaxy properties in the future. In this section, we describe some areas in which improved theoretical models or observations will make a significant impact on galaxy evolution studies.

- **Stellar tracks:** Current stellar population synthesis and photoionization models are limited to a coarse grid of five metallicities that is determined by the metallicities of the stellar tracks and opacity tables. Stellar tracks track how stars of a given mass evolve on the Hertzsprung–Russell diagram and are computed from stellar evolution theory and large observational stellar libraries. Stellar tracks require a set of elemental abundance ratios as an input parameter and have usually been calculated by scaling the relative abundance ratios in Anders & Grevesse (1989). There are two problems with this. First, five sets of metallicities limit the resolution at which theoretical strong-line metallicity diagnostics can be calculated and the stellar evolution models and/or photoionization models are currently being interpolated. Ideally, stellar tracks (and opacity tables) would be calculated at intervals of 0.2–0.5 dex in $\log(O/H)$. Second, it is now known that the Anders & Grevesse (1989) relative abundance ratios do not match observed abundance ratios in HII regions in the Milky Way, Large Magellanic Cloud, or Small Magellanic Cloud at a given metallicity. Stellar tracks and opacity

tables that represent the observed abundance ratios in the Milky Way and nearby galaxies (see Nieva & Przybilla 2012, Nicholls et al. 2017) are critically needed and could be computed with current stellar evolution models and data sets. These tracks would allow consistent abundance ratios to be used in stellar population synthesis and photoionization models to derive high-resolution metallicity diagnostics for the first time.

- **Stellar population synthesis models:** The theoretical prediction of emission lines depends on the ionization potential of each emission line and is therefore sensitive to the shape of the ionizing EUV radiation field at the wavelength of the ionization potential. The EUV radiation field is produced solely by the stellar evolution synthesis models, and different models produce remarkably different SED shapes, depending on the input physics.

Despite significant advances in stellar population synthesis models, the cause(s) of the discrepancy between observed and predicted emission lines such as (but not limited to) [NeIII] remain unknown. Detailed multilevel non-local thermodynamic equilibrium (NLTE) treatment including radiation-driven wind theory and a consistent calculation of NLTE line blocking opacities for all contributing ionization stages is critical (Sellmaier et al. 1996, Giveon et al. 2002, Weber et al. 2015), as is understanding the contribution from scattered light to HII region spectra (Simón-Díaz et al. 2011). Stellar evolution models also need to include the effects of both stellar rotation and binary stars, rather than these effects being taken into account in different stellar evolution models. Ideally, both members of binary star systems would be evolved simultaneously with NLTE atmospheres that include metal opacities for all contributing ionization stages.

- **Ionization structure of HII regions:** High spatial resolution, high S/N observations with broad wavelength coverage across nearby HII regions are needed to understand the ionization structure in HII regions. Observations of multiple ionization states of different species is needed. Single-star HII regions are useful for such studies because the effective temperature of the ionizing star is known (Zastrow et al. 2013), but star clusters must be modeled also. With the detailed ionization structure known, it may be possible to reverse-engineer the detailed shape of the ionizing radiation field required to produce such an ionization structure through photoionization models. These observations would provide important constraints on the shape of the ionizing radiation field required from the stellar population synthesis models.
- **Super star clusters:** Spectra of high-redshift galaxies are a luminosity-weighted average of the star-forming regions within the spectral aperture. If super star clusters are common in high-redshift star-forming galaxies, then a larger proportion of super star clusters may dominate the emission-line ratios observed. Surface-brightness dimming may exacerbate this effect. The ionization parameter is large in local super star clusters $-1.5 < \log(U) < -2.3$ (Smith et al. 2006, Snijders et al. 2007). As seen in this review, the ionization parameter can significantly affect the measurement of fundamental galaxy properties such as the ISM pressure and the metallicity. To estimate the importance of this effect, systematic studies are needed on the properties of nearby super star clusters, as well as the fraction of super star clusters in galaxies as a function of redshift.
- **HII region structure:** Most photoionization models are calculated for radiation-bounded HII regions, in which the nebula ends where hydrogen is completely recombined. However, Nakajima et al. (2013) suggest that Lyman- α emitters at high redshift contain density-bounded HII regions. In a density-bounded nebula, the density is sufficiently low that the stars can ionize the entire nebula. Although the higher-ionization lines like [OIII] are closer to the star cluster and are unaffected by how the nebula is bounded, the hydrogen recombination zone may be shortened in density-bounded nebulae. The [OIII]/H β ratio observed

will then be larger in density-bounded nebulae than in a radiation-bounded nebula. The outer partially ionized zone is shortened in density-bounded nebulae, reducing the emission of [SII] and [OI] and possibly even [NII]. It is currently unclear whether density-bounded nebulae are common in normal star-forming galaxies either locally or at high redshift. Detailed ionization mapping of the HII regions in nearby galaxies would constrain the fraction of HII regions that are radiation bounded and density bounded. A mixture of radiation-bounded and density-bounded HII regions has been observed in the local group (Pellegrini et al. 2012).

A better understanding of the density structure of local HII regions is required. This area would benefit from high spatial resolution observations of nearby HII regions in a broad range of environments. In concert with these observations, complex theoretical modeling of HII regions needs to evolve from simple plane parallel or spherical geometries to full Monte Carlo radiative transfer codes in order to take complex geometries and density structures into account [see Steinacker et al. (2013) for a review]. Initial Monte Carlo radiative transfer or dust models with ray-tracing techniques have been developed (Gordon et al. 2001, Ercolano et al. 2008, Popescu & Tuffs 2013, Vandenbroucke & Wood 2018). These 3D models offer much promise for future modeling of HII regions and galaxies. For example, De Looze et al. (2014) and Law et al. (2011) use 3D radiative transfer to model the young stellar populations and dust-heating processes in nearby star-forming galaxies. De Looze et al. show that 3D models can reproduce the FIR and submillimeter observations of M51, and they calculate the relative contributions of stars and dust. Popescu et al. (2017) use their 3D models to solve for the UV-submillimeter interstellar radiation fields of the Milky Way, a notoriously difficult problem. We anticipate that the next major advance in the galaxy spectral modeling field will be the development of fully self-consistent 3D radiative transfer models, which will allow detailed dust and gas distributions to be embedded within the photoionized nebula with arbitrary temperature, density, and dust distributions. See Law et al. (2018) for recent promising work.

- **Identifying shocks:** Shock excitation can contaminate both low-ionization line ratios and high-ionization line ratios, depending on the shock velocity. High-resolution integral field spectroscopy allows the shock component to be resolved and separated from the HII region component of optical emission lines through the combination of morphological information, velocity maps, velocity dispersion, and emission-line ratios [see Ho et al. (2014) and Yuan et al. (2012) for examples of how shocks can be identified at low and high redshift, respectively]. We recommend that these tools be used to identify galaxies containing shocks prior to the application of emission-line diagnostics. In cases where shocks and star-forming regions can be separated, it is feasible to apply pressure, ionization parameter, and metallicity diagnostics to the HII region component of the spectra.

Three-dimensional diagnostics using velocity dispersion, radius, and line ratio information are exceptionally promising ways to separate and quantify the contribution from shocks, star formation, and AGNs across galaxies (D'Agostino et al. 2019). Currently, 3D diagnostics only exist for the optical. Extensions of such diagnostics to the UV and IR spectral ranges, as well as comprehensive studies of the location of theoretical models on these diagrams, are needed to fully exploit the potential of these diagnostics.

- **Diffuse ionized gas modeling:** Theoretical models are needed to help remove the DIG component from spectra. Unfortunately, current photoionization models can only partially reproduce the DIG line ratios (e.g., Bland-Hawthorn et al. 1997, Zhang et al. 2017), leading to additional ionizing sources being proposed. For example, Martin (1996) used a combination of photoionized gas with shock-ionized gas using various shock speeds and

turbulent mixing layers of various temperatures to model the DIG in irregular galaxies. Zhang et al. (2017) showed that photoionization models fail to reproduce the strength of the low-ionization optical lines and suggested that a radiation field from evolved stellar populations may resolve this discrepancy. High spatial resolution (10–100 pc) integral field spectroscopy of large samples of face-on galaxies is required to characterize the conditions within the DIG to help inform DIG models. With such information, DIG models might allow reliable properties to be derived for the global spectra of galaxies or coarse (~ 1 kpc) resolution integral field spectroscopy by providing an estimate of, and correction for, the contamination from the DIG to each emission line across a spectrum. In particular, it is necessary to understand the contamination from the DIG to the UV diagnostic line ratios, because it is currently difficult, and in many cases impossible, to observe the contribution from the DIG in the UV spectrum.

- **Understanding global spectra:** Understanding the properties derived for global spectra of galaxies (or for large spaxels within galaxies where HII regions are unresolved) is nontrivial but is critical for studies of the highest-redshift galaxies. Previous work in understanding global spectral properties uses single-slit spectroscopy of HII regions or integral field spectroscopy where HII regions are unresolved (e.g., Kobulnicky et al. 1999, Moustakas 2006, Gavazzi et al. 2018). Much may be learned by repeating these studies using significantly higher spatial resolution observations that resolve the temperature and density structure within HII regions. High spatial resolution observations of nearby galaxies could be used to simulate surface brightness dimming of high-redshift galaxies and then be convolved with the response functions of current and future instruments to understand how derived global properties of high-redshift galaxies relate to the actual properties within galaxies. For example, the global metallicity of a high-redshift galaxy may not be the true mean metallicity but may be weighted toward specific HII regions with certain sets of properties. Note that because high-redshift galaxies are not the same as local galaxies, theoretical simulations that place HII regions with complex temperature and density structures within a model galaxy from cosmological zoom-in simulations at a given redshift may help inform observational studies in the future. Recent theoretical work in this area indicates that there are large effects on metallicity gradients at high redshift from low S/N ratios and beam smearing (Acharyya et al. 2019). The inclusion of simulations of the DIG would significantly improve these simulations.
- **Limited sets of emission lines:** Some samples contain only limited sets of emission lines, necessitating the use of only two or three emission lines for diagnosing fundamental galaxy properties. Common examples include spectra of high-redshift galaxies obtained using IR bandpasses. Care must be taken not to derive more parameters than there are constraints from the emission lines. Each unique emission-line ratio provides a single constraint unless additional information is included, such as equivalent widths (where the continuum provides an additional constraint) or stellar masses. Theoretical models should be used to investigate the dependence of sets of line ratios on relevant galaxy properties prior to the application of the line ratios. If a specific line is to be used regularly in a given sample, we strongly recommend undertaking a comprehensive study of the properties of that line and potential caveats, such as the research by Jaskot & Ravindranath (2016). These authors use models with varying C/O abundances, dust content, gas density, nebular geometry, and optical depth to understand the impact of each of these properties on the CIII] line. Other lines that warrant such a study include, but are not limited to, the [CIV] $\lambda 1549$ line, the [SiIII] and SiIII] ($\lambda \lambda 1883, 92$) lines, and the UV and optical nitrogen lines. Tracking individual elements through cosmological simulations is also needed. Naiman et al. (2018) present such a study

of magnesium and europium. Further studies like these, extended to other elements, will be essential to inform galaxy evolution studies using emission lines with future extremely large telescopes.

DISCLOSURE STATEMENT

The authors are not aware of any affiliations, memberships, funding, or financial holdings that might be perceived as affecting the objectivity of this review.

ACKNOWLEDGEMENTS

The authors would like to thank the editor, Luis Ho, for his feedback and support of this manuscript. L.J.K. would like to acknowledge the staff and residents of Varuna, the National Writers' House, and the UNSW ASTRO 3D Writing Retreat for providing tranquility, excellent food, and a supportive writing atmosphere. Parts of this research were supported by the Australian Research Council (ARC) Centre of Excellence for All Sky Astrophysics in 3 Dimensions (ASTRO 3D), through project number CE170100013. L.J.K. gratefully acknowledges the support of an ARC Laureate Fellowship (FL150100113). This research has made extensive use of NASA's Astrophysics Data System Bibliographic Services.

LITERATURE CITED

- Acharyya A, Krumholz M, Federrath C, et al. 2019. *MNRAS*. Submitted
- Afflerbach A, Churchwell E, Werner MW. 1997. *Ap. J.* 478:190–205
- Allen MG, Dopita MA, Tsvetanov ZI. 1998. *Ap. J.* 493:571–82
- Allen MG, Groves BA, Dopita MA, et al. 2008. *Ap. J. Suppl.* 178:20–55
- Aller LH. 1942. *Ap. J.* 95:52
- Aller LH. 1961. In *Liege International Astrophysical Colloquia*, Vol. 10, pp. 534–37. Liege, Belg.: Inst. Astrophys., Univ. Liege
- Aller LH, ed. 1984. *Physics of Thermal Gaseous Nebulae*. Dordrecht, Neth.: Reidel
- Aller LH, Czyzak SJ, Walker MF, Krueger TK. 1970. *PNAS* 66:1–5
- Alloin D, Collin-Souffrin S, Joly M, Vigroux L. 1979. *Astron. Astrophys.* 78:200–16
- Alongi M, Bertelli G, Bressan A, et al. 1993. *Astron. Astrophys. Suppl.* 97:851–71
- Anders E, Grevesse N. 1989. *Geochim. Cosmochim. Acta* 53:197–214
- Andrews BH, Martini P. 2013. *Ap. J.* 765:140
- Arimoto N, Yoshii Y. 1986. *Astron. Astrophys.* 164:260–73
- Armus L, Charmandaris V, Bernard-Salas J, et al. 2007. *Ap. J.* 656:148–67
- Asplund M, Grevesse N, Sauval AJ, Scott P. 2009. *Annu. Rev. Astron. Astrophys.* 47:481–522
- Bahcall JN, Kozlovsky BZ. 1969a. *Ap. J.* 155:1077–97
- Bahcall JN, Kozlovsky BZ. 1969b. *Ap. J.* 158:529–33
- Baldry IK, Glazebrook K, Baugh CM, et al. 2002. *Ap. J.* 569:582–94
- Baldwin JA, Phillips MM, Terlevich R. 1981. *Publ. Astron. Soc. Pac.* 93:5–19
- Barnes JE, Wood K, Hill AS, Haffner LM. 2015. *MNRAS* 447:559–66
- Bayliss MB, Rigby JR, Sharon K, et al. 2014. *Ap. J.* 790:144–64
- Begelman MC. 1990. In *The Interstellar Medium in Galaxies*, ed. HA Thronson Jr., JM Shull. *Ap. Space Sci. Libr.* 161:287–304. Dordrecht, Neth.: Reidel
- Belfiore F, Maiolino R, Maraston C, et al. 2016. *MNRAS* 461:3111–34
- Bell EF, de Jong RS. 2000. *MNRAS* 312:497–520
- Bertoldi F. 1989. *Ap. J.* 346:735–55
- Best PN, Röttgering HJA, Longair MS. 2000. *MNRAS* 311:23–36

- Bian F, Fan X, Bechtold J, et al. 2010. *Ap. J.* 725:1877–85
- Binette L, Dopita MA, Tuohy IR. 1985. *Ap. J.* 297:476–91
- Binette L, González-Gómez DI, Mayya YD. 2002. *Rev. Mex. Astron. Astrofis. Conf. Ser.* 38:279–88
- Binette L, Magris CG, Stasińska G, Bruzual AG. 1994. *Astron. Astrophys.* 292:13–19
- Blanc GA, Heiderman A, Gebhardt K, et al. 2009. *Ap. J.* 704:842–62
- Blanc GA, Kewley L, Vogt FPA, Dopita MA. 2015. *Ap. J.* 798:99
- Bland-Hawthorn J, Freeman KC, Quinn PJ. 1997. *Ap. J.* 490:143–55
- Boselli A, Gavazzi G, Donas J, Scodreggio M. 2001. *Astron. J.* 121:753–67
- Bresolin F, Kennicutt RC Jr., Garnett DR. 1999. *Ap. J.* 510:104–24
- Bressan A, Chiosi C, Fagotto F. 1994. *Ap. J. Suppl.* 94:63–115
- Bressan A, Fagotto F, Bertelli G, Chiosi C. 1993. *Astron. Astrophys. Suppl.* 100:647–64
- Brinchmann J, Charlot S, White SDM, et al. 2004. *MNRAS* 351:1151–79
- Brinchmann J, Pettini M, Charlot S. 2008. *MNRAS* 385:769–82
- Brooks AM, Governato F, Booth CM, et al. 2007. *Ap. J. Lett.* 655:L17–20
- Brown JS, Martini P, Andrews BH. 2016. *MNRAS* 458:1529–47
- Bruzual G, Charlot S. 2011. *GALAXEV: evolutionary stellar population synthesis models*. Astrophysics Source Code Library. ascl:1104.005
- Bruzual AG. 1983. *Ap. J.* 273:105–27
- Bruzual AG, Charlot S. 1993. *Ap. J.* 405:538–53
- Burbidge GR, Burbidge M, Hoyle F, Lynds CR. 1966. *Nature* 210:774–78
- Bustamante S, Sparre M, Springel V, Grand RJJ. 2018. *MNRAS* 479:3381–92
- Buzzoni A. 1989. *Ap. J. Suppl.* 71:817–69
- Byler N, Dalcanton JJ, Conroy C, Johnson BD. 2017. *Ap. J.* 840:44
- Byler N, Dalcanton JJ, Conroy C, et al. 2018. *Ap. J.* 863:14
- Calzetti D. 2013. In *Secular Evolution of Galaxies, Proceedings of the 23rd Canary Islands Winter School of Astrophysics*, ed. J Falcon-Barroso, JH Knapen, pp. 419–58. Cambridge, UK: Cambridge Univ. Press
- Calzetti D, Kennicutt RC, Engelbracht CW, et al. 2007. *Ap. J.* 666:870–95
- Calzetti D, Wu SY, Hong S, et al. 2010. *Ap. J.* 714:1256–79
- Carton D, Brinchmann J, Contini T, et al. 2018. *MNRAS* 478:4293–316
- Charlot S, Bruzual AG. 1991. *Ap. J.* 367:126–40
- Charlot S, Longhetti M. 2001. *MNRAS* 323:887–903
- Chevallard J, Charlot S. 2016. *MNRAS* 462:1415–43
- Chiappini C, Matteucci F, Romano D. 2001. *Ap. J.* 554:1044–58
- Chisholm J, Bordoloi R, Rigby JR, Bayliss M. 2018. *MNRAS* 474:1688–704
- Cid Fernandes R, Heckman T, Schmitt H, et al. 2001. *Ap. J.* 558:81–108
- Clegg RES, Harrington JP, Barlow MJ, Walsh JR. 1987. *Ap. J.* 314:551–71
- Conroy C. 2013. *Annu. Rev. Astron. Astrophys.* 51:393–455
- Considère S, Coziol R, Contini T, Davoust E. 2000. *Astron. Astrophys.* 356:89–101
- Constantin A, Vogeley MS. 2006. *Ap. J.* 650:727–48
- Copetti MVF, Mallmann JAH, Schmidt AA, Castañeda HO. 2000. *Astron. Astrophys.* 357:621–36
- Copetti MVF, Writzl BC. 2002. *Astron. Astrophys.* 382:282–90
- Cotera AS, Colgan SWJ, Simpson JP, Rubin RH. 2005. *Ap. J.* 622:333–45
- Cullen F, Cirasuolo M, McLure RJ, et al. 2014. *MNRAS* 440:2300–12
- Cunha K, Frinchaboy PM, Souto D, et al. 2016. *Astron. Nachr.* 337:922
- Curti M, Cresci G, Mannucci F, et al. 2017. *MNRAS* 465:1384–400
- D’Agostino JJ, Kewley LJ, Groves BA, et al. 2019. *MNRAS* 485:38–42
- D’Agostino JJ, Poetrodjojo H, Ho IT, et al. 2018. *MNRAS* 479:4907–35
- da Cunha E. 2016. *LAU Focus Meet.* 29:184–85
- Dalcanton JJ. 2007. *Ap. J.* 658:941–59
- Dale JE, Ercolano B, Bonnell IA. 2012. *MNRAS* 427:2852–65
- Davé R, Finlator K, Oppenheimer BD. 2011. *MNRAS* 416:1354–76
- Davidson K. 1972. *Ap. J.* 171:213

- Davies RL, Förster Schreiber NM, Übler H, et al. 2019. *Ap. J.* arXiv:1808.10700
- Davies RL, Groves B, Kewley LJ, et al. 2016. *MNRAS* 462:1616–29
- Davies RL, Kewley LJ, Ho IT, Dopita MA. 2014a. *MNRAS* 444:3961–74
- Davies RL, Rich JA, Kewley LJ, Dopita MA. 2014b. *MNRAS* 439:3835–46
- De Looze I, Fritz J, Baes M, et al. 2014. *Astron. Astrophys.* 571:A69
- De Lucia G, Kauffmann G, White SDM. 2004. *MNRAS* 349:1101–16
- de Mink SE, Cantiello M, Langer N, et al. 2009. *Astron. Astrophys.* 497:243–53
- de Pree CG, Rodriguez LF, Goss WM. 1995. *Rev. Mex. Astron. Astrofis.* 31:39–44
- De Robertis MM, Dufour RJ, Hunt RW. 1987. *J. R. Astron. Soc. Can.* 81:195–220
- De Rossi ME, Bower RG, Font AS, Schaye J, Theuns T. 2017. *MNRAS* 472:3354–77
- Denicoló G, Terlevich R, Terlevich E. 2002. *MNRAS* 330:69–74
- Díaz AI, Pérez-Montero E. 2000. *MNRAS* 312:130–38
- Dinerstein HL. 1990. In *The Interstellar Medium in Galaxies*, ed. HA Thronson Jr., JM Shull. *Ap. Space Sci. Libr.* 161:257–85. Dordrecht, Neth.: Reidel
- Dopita MA, Evans IN. 1986. *Ap. J.* 307:431–40
- Dopita MA, Fischera J, Sutherland RS, et al. 2006. *Ap. J.* 647:244–55
- Dopita MA, Groves BA, Sutherland RS, Kewley LJ. 2003. *Ap. J.* 583:727–31
- Dopita MA, Kewley LJ, Heisler CA, Sutherland RS. 2000. *Ap. J.* 542:224–34
- Dopita MA, Kewley LJ, Sutherland RS, Nicholls DC. 2016. *Ap. Space Sci.* 361:61
- Dopita MA, Mason DJ, Robb WD. 1976. *Ap. J.* 207:102–9
- Dopita MA, Sutherland RS. 1995. *Ap. J.* 455:468
- Dors OL Jr., Copetti MVF. 2005. *Astron. Astrophys.* 437:837–47
- Dors OL Jr., Krabbe A, Hägele GF, Pérez-Montero E. 2011. *MNRAS* 415:3616–26
- Draine BT, Kreisich CD. 2018. *Ap. J.* 862:30
- Dufton PL, Keenan FP, Kingston AE. 1984. *MNRAS* 209:1P–4P
- Edmunds MG, Pagel BEJ. 1984. *MNRAS* 211:507–19
- Eldridge JJ, Stanway ER. 2009. *MNRAS* 400:1019–28
- Eldridge JJ, Stanway ER. 2012. *MNRAS* 419:479–89
- Elmegreen BG, Kimura T, Tosa M. 1995. *Ap. J.* 451:675
- Erb DK, Shapley AE, Pettini M, et al. 2006. *Ap. J.* 644:813–28
- Ercolano B, Young PR, Drake JJ, Raymond JC. 2008. *Ap. J. Suppl.* 175:534–42
- Esteban C, Bresolin F, Peimbert M, et al. 2009. *Ap. J.* 700:654–78
- Esteban C, Carigi L, Copetti MVF, et al. 2013. *MNRAS* 433:382–93
- Esteban C, García-Rojas J, Peimbert M, et al. 2005. *Ap. J. Lett.* 618:L95–98
- Esteban C, Peimbert M, Torres-Peimbert S. 1999. *Astron. Astrophys.* 342:L37–40
- Feltre A, Charlot S, Gutkin J. 2016. *MNRAS* 456:3354–74
- Ferkinhoff C, Hailey-Dunsheath S, Nikola T, et al. 2010. *Ap. J. Lett.* 714:L147–51
- Ferland G, Netzer H. 1979. *Ap. J.* 229:274–90
- Ferland GJ, Chatzikos M, Guzmán F, et al. 2017. *Rev. Mex. Astron. Astrofis.* 53:385–438
- Ferland GJ, Korista KT, Verner DA, et al. 1998. *Publ. Astron. Soc. Pac.* 110:761–78
- Fernández-Ontiveros JA, Spinoglio L, Pereira-Santaella M, et al. 2016. *Ap. J. Suppl.* 226:19
- Field GB. 1965. *Ap. J.* 142:531–67
- Filippenko AV. 1985. *Ap. J.* 289:475–89
- Finlator K, Davé R. 2008. *MNRAS* 385(4):2181–204
- Fioc M, Le Borgne D, Rocca-Volmerange B. 2011. *PÉGASE: metallicity-consistent spectral evolution model of galaxies*. Astrophysics Source Code Library. ascl:1108.007
- Flohic HMLG, Eracleous M, Chartas G, et al. 2006. *Ap. J.* 647:140–60
- Förster Schreiber NM, Genzel R, Lutz D, et al. 2001. *Ap. J.* 552:544–71
- Franco J, Kurtz S, Hofner P, et al. 2000. *Ap. J. Lett.* 542:L143–46
- French HB. 1983. *Ap. J.* 273:214–18
- Fu J, Hou JL, Yin J, Chang RX. 2009. *Ap. J.* 696:668–75
- Gabor JM, Davé R, Finlator K, Oppenheimer BD. 2010. *MNRAS* 407:749–71

- García-Benito R, Díaz A, Hägele GF, et al. 2010. *MNRAS* 408:2234–55
- García-Rojas J, Esteban C. 2007. *Ap. J.* 670:457–70
- García-Rojas J, Esteban C, Peimbert A, et al. 2005. *MNRAS* 362:301–12
- García-Rojas J, Simón-Díaz S, Esteban C. 2014. *Astron. Astrophys.* 571:A93
- Garnett DR. 2002. *Ap. J.* 581:1019–31
- Garnett DR, Shields GA, Skillman ED, et al. 1997. *Ap. J.* 489:63–86
- Gavazzi G, Consolandi G, Belladitta S, et al. 2018. *Astron. Astrophys.* 615:A104
- Genzel R, Lutz D, Sturm E, et al. 1998. *Ap. J.* 498:579–605
- Georgy C, Ekström S, Meynet G, et al. 2012. *Astron. Astrophys.* 542:A29
- Giveon U, Sternberg A, Lutz D, et al. 2002. *Ap. J.* 566:880–97
- Gonzalez-Delgado RM, Perez E, Tenorio-Tagle G, et al. 1994. *Ap. J.* 437:239–61
- Gordon KD, Misselt KA, Witt AN, Clayton GC. 2001. *Ap. J.* 551:269–76
- Goudfrooij P, Hansen L, Jorgensen HE, Norgaard-Nielsen HU. 1994. *Astron. Astrophys. Suppl.* 105:341–83
- Gritschneder M, Naab T, Walch S, et al. 2009. *Ap. J. Lett.* 694:L26–30
- Groves BA, Cecil G, Ferruit P, Dopita MA. 2004. *Ap. J.* 611:786–94
- Groves BA, Dopita MA, Sutherland RS. 2004a. *Ap. J. Suppl.* 153:9–73
- Groves BA, Dopita MA, Sutherland RS. 2004b. *Ap. J. Suppl.* 153:75–91
- Groves BA, Heckman TM, Kauffmann G. 2006. *MNRAS* 371:1559–69
- Guiderdoni B, Rocca-Volmerange B. 1987. *Astron. Astrophys.* 186:1–21
- Gutiérrez L, Beckman JE. 2010. *Ap. J. Lett.* 710:L44–48
- Gutkin J, Charlot S, Bruzual G. 2016. *MNRAS* 462:1757–74
- Haffner LM, Dettmar RJ, Beckman JE, et al. 2009. *Rev. Mod. Phys.* 81:969–97
- Hägele GF, Díaz ÁI, Terlevich E, et al. 2008. *MNRAS* 383:209–29
- Hägele GF, Pérez-Montero E, Díaz ÁI, et al. 2006. *MNRAS* 372:293–312
- Hainline KN, Shapley AE, Kornei KA, et al. 2009. *Ap. J.* 701:52–65
- Halpern JP, Grindlay JE. 1980. *Ap. J.* 242:1041–55
- Hatchett S, Buff J, McCray R. 1976. *Ap. J.* 206:847–60
- Heckman T, Borthakur S, Wild V, et al. 2017. *Ap. J.* 846:151
- Heckman TM. 1980. *Astron. Astrophys.* 87:152–64
- Heckman TM. 2003. In *Galaxy Evolution: Theory & Observations*, ed. V Avila-Reese, C Firmani, CS Frenk, C Allen. *Rev. Mex. Astron. Astrofis. Conf. Ser.* 17:47–55
- Henry A, Scarlata C, Domínguez A, et al. 2013. *Ap. J. Lett.* 776:L27
- Herrera-Camus R, Bolatto A, Smith JD, et al. 2016. *Ap. J.* 826:175
- Hill TL, Heisler CA, Sutherland R, Hunstead RW. 1999. *Astron. J.* 117:111–25
- Hillier JD. 2012. In *From Interacting Binaries to Exoplanets: Essential Modeling Tools*, *Proc. IAU Symp.* 282, ed. MT Richards, I Hubeny, 7:229–34. Cambridge, UK: Cambridge Univ. Press
- Hirschmann M, Charlot S, Feltre A, et al. 2017. *MNRAS* 472:2468–95
- Ho IT, Kewley LJ, Dopita MA, et al. 2014. *MNRAS* 444:3894–910
- Ho IT, Kudritzki RP, Kewley LJ, et al. 2015. *MNRAS* 448:2030–54
- Ho IT, Medling AM, Bland-Hawthorn J, et al. 2016. *MNRAS* 457:1257–78
- Ho LC. 2008. *Annu. Rev. Astron. Astrophys.* 46:475–539
- Ho LC, Filippenko AV, Sargent WLW. 1993. *Ap. J.* 417:63–81
- Ho LC, Filippenko AV, Sargent WLW. 1996. *Ap. J.* 462:183
- Hoyos C, Díaz AI. 2006. *MNRAS* 365:454–68
- Hsieh BC, Lin L, Lin JH, et al. 2017. *Ap. J. Lett.* 851:L24
- Hunt L, Dayal P, Magrini L, Ferrara A. 2016. *MNRAS* 463:2020–31
- Indebetouw R, de Messières GE, Madden S, et al. 2009. *Ap. J.* 694:84–106
- Ivison RJ, Swinbank AM, Swinyard B, et al. 2010. *Astron. Astrophys.* 518:L35
- Izotov YI, Thuan TX. 1999. *Ap. J.* 511:639–59
- Izotov YI, Thuan TX, Wilson JC. 2009. *Ap. J.* 703:1984–91
- Jaskot AE, Ravindranath S. 2016. *Ap. J.* 833:136
- Jensen EB, Strom KM, Strom SE. 1976. *Ap. J.* 209:748–69

- Johnson KE, Kobulnicky HA. 2003. *Ap. J.* 597:923–28
- Jones AP. 2000. *J. Geophys. Res.* 105:10257–68
- Kaasinen M, Bian F, Groves B, et al. 2017. *MNRAS* 465:3220–34
- Kakkad D, Groves B, Dopita M, et al. 2018. *Astron. Astrophys.* 618:A6
- Kallman TR, McCray R. 1982. *Ap. J. Suppl.* 50:263–317
- Kashino D, Renzini A, Silverman JD, Daddi E. 2016. *Ap. J. Lett.* 823:L24
- Kauffmann G, Heckman TM, Tremonti C, et al. 2003. *MNRAS* 346:1055–77
- Keel WC. 1983. *Ap. J.* 269:466–86
- Keenan FP, Feibelman WA, Berrington KA. 1992. *Ap. J.* 389:443–46
- Kennicutt RC Jr. 1998. *Annu. Rev. Astron. Astrophys.* 36:189–232
- Kennicutt RC Jr., Keel WC. 1984. *Ap. J. Lett.* 279:L5–9
- Kewley LJ, Dopita MA. 2002. *Ap. J. Suppl.* 142:35–52
- Kewley LJ, Dopita MA, Sutherland RS, et al. 2001a. *Ap. J.* 556:121–40
- Kewley LJ, Ellison SL. 2008. *Ap. J.* 681:1183–204
- Kewley LJ, Geller MJ, Barton EJ. 2006a. *Astron. J.* 131:2004–17
- Kewley LJ, Groves B, Kauffmann G, Heckman T. 2006b. *MNRAS* 372:961–76
- Kewley LJ, Heisler CA, Dopita MA, Lumsden S. 2001b. *Ap. J. Suppl.* 132:37–71
- Kewley LJ, Maier C, Yabe K, et al. 2013. *Ap. J. Lett.* 774:L10
- Kewley LJ, Rupke D, Zahid HJ, et al. 2010. *Ap. J. Lett.* 721:L48–52
- Kewley LJ, Zahid HJ, Geller MJ, et al. 2015. *Ap. J. Lett.* 812:L20
- Kewley LJ. 2019. *Ap. J.* In press
- Kinman TD, Davidson K. 1981. *Ap. J.* 243:127–39
- Kobayashi C, Nakasato N. 2011. *Ap. J.* 729:16
- Kobulnicky HA, Kennicutt RC Jr., Pizagno JL. 1999. *Ap. J.* 514:544–57
- Kobulnicky HA, Kewley LJ. 2004. *Ap. J.* 617:240–61
- Kobulnicky HA, Phillips AC. 2003. *Ap. J.* 599:1031–42
- Köppen J, Weidner C, Kroupa P. 2007. *MNRAS* 375:673–84
- Kotulla R, Fritze U, Weillbacher P, Anders P. 2009. *MNRAS* 396:462–84
- Kramida A, Ralchenko Y, Reader J, NIST ASD Team. 2018. *NIST Atomic Spectra Database, Ver. 5.6*. Gaithersburg, MD: Natl. Inst. Stand. Technol. <http://physics.nist.gov/asd> [2018, November 27].
- Krolik JH, McKee CF. 1978. *Ap. J. Suppl.* 37:459–83
- Krumholz MR, Fumagalli M, da Silva RL, et al. 2015. *MNRAS* 452:1447–67
- Kurtz S. 2002. In *Hot Star Workshop III: The Earliest Stages of Massive Star Birth*, ed. P Crowther. *ASP Conf. Ser.* 267:81–94
- Kurucz RL. 1979. *Ap. J. Suppl.* 40:1–340
- Lara-López MA, Cepa J, Bongiovanni A, et al. 2010. *Astron. Astrophys.* 521:L53
- Larson RB, Tinsley BM. 1978. *Ap. J.* 219:46–59
- Laurent O, Mirabel IF, Charmandaris V, et al. 2000. *Astron. Astrophys.* 359:887–99
- Law KH, Gordon KD, Misselt KA. 2011. *Ap. J.* 738:124
- Law KH, Gordon KD, Misselt KA. 2018. *Ap. J. Suppl.* 236:32
- Lee SJ, Hyung S. 2013. *Astron. Astrophys.* 549:A65
- Leitherer C. 2008. In *Low-Metallicity Star Formation: From the First Stars to Dwarf Galaxies, Proc. IAU Symp.* 255, ed. LK Hunt, S Madden, R Schneider, pp. 305–9. Cambridge, UK: Cambridge Univ. Press
- Leitherer C, Ekström S, Meynet G, et al. 2014. *Ap. J. Suppl.* 212:14
- Leitherer C, Schaerer D, Goldader JD, et al. 1999. *Ap. J. Suppl.* 123:3–40
- Leitherer C, Tremonti CA, Heckman TM, Calzetti D. 2011. *Astron. J.* 141:37
- Lequeux J, Peimbert M, Rayo JF, et al. 1979. *Astron. Astrophys.* 80:155–66
- Levesque EM, Kewley LJ, Larson KL. 2010. *Astron. J.* 139:712–27
- Levesque EM, Leitherer C, Ekstrom S, et al. 2012. *Ap. J.* 751:67
- Liang YC, Hammer F, Yin SY. 2007. *Astron. Astrophys.* 474:807–14
- Liang YC, Hammer F, Yin SY, et al. 2007. *Astron. Astrophys.* 473:411–21
- Liang YC, Yin SY, Hammer F, et al. 2006. *Astron. Astrophys.* 447:113–19

- Lilly SJ, Carollo CM, Pipino A, et al. 2013. *Ap. J.* 772:119
- Liu XW, Barlow MJ, Zhang Y, et al. 2006. *MNRAS* 368:1959–70
- Liu XW, Luo SG, Barlow MJ, et al. 2001. *MNRAS* 327:141–68
- Liu XW, Storey PJ, Barlow MJ, et al. 2000. *MNRAS* 312:585–628
- Livadiotis G, Desai MI, Wilson III LB. 2018. *Ap. J.* 853:142
- López-Sánchez ÁR, Dopita MA, Kewley LJ, et al. 2012. *MNRAS* 426:2630–51
- Luridiana V, Cerviño M. 2003. In *Star Formation Through Time: A Conference to Honour Roberto J. Terlevich*, ed. E Perez, RM Gonzalez Delgado, G Tenorio-Tagle. *ASP Conf. Ser.* 297:49–54
- Lutz D. 2014. *Annu. Rev. Astron. Astrophys.* 52:373–414
- Ly C, Malkan MA, Nagao T, et al. 2014. *Ap. J.* 780:122
- Ly C, Malkan MA, Rigby JR, Nagao T. 2016. *Ap. J.* 828:67
- Ma X, Hopkins PF, Faucher-Giguère CA, et al. 2016. *MNRAS* 456:2140–56
- MacAlpine GM. 1974. *Ap. J.* 193:37–42
- Madsen GJ, Reynolds RJ, Haffner LM. 2006. *Ap. J.* 652:401–25
- Maier C, Lilly SJ, Carollo CM, et al. 2006. *Ap. J.* 639:858–67
- Maier C, Lilly SJ, Ziegler BL, et al. 2014. *Ap. J.* 792:3
- Maiolino R, Caselli P, Nagao T, et al. 2009. *Astron. Astrophys.* 500:L1–4
- Maiolino R, Cox P, Caselli P, et al. 2005. *Astron. Astrophys.* 440:L51–54
- Maiolino R, Nagao T, Grazian A, et al. 2008. *Astron. Astrophys.* 488:463–79
- Malmann JAH, Copetti MVF, Dos Santos ICF, et al. 2002. In *X Reunión Regional Latinoamericana de Astronomía, LAU*, ed. JJ Claria, D Garcia Lambas, H Levato. *Rev. Mex. Astron. Astrofis. Conf. Ser.* 14:57
- Mannucci F, Cresci G, Maiolino R, et al. 2010. *MNRAS* 408:2115–27
- Marino RA, Gil de Paz A, Sánchez SF, et al. 2016. *Astron. Astrophys.* 585:47
- Marino RA, Rosales-Ortega FF, Sánchez SF, et al. 2013. *Astron. Astrophys.* 559:A114
- Martin CL. 1996. *Ap. J.* 465:680
- Martin CL. 1997. *Ap. J.* 491:561–83
- Mathez G. 1969. *Astron. Astrophys.* 3:127–34
- Mathis JS. 1985. *Ap. J.* 291:247–59
- Mathis JS. 2000. *Ap. J.* 544:347–55
- Mathis JS, Liu XW. 1999. *Ap. J.* 521:212–16
- Mathis JS, Rosa MR. 1991. *Astron. Astrophys.* 245:625–34
- McCall ML, Rybski PM, Shields GA. 1985. *Ap. J. Suppl.* 57:1–62
- McGaugh SS. 1991. *Ap. J.* 380:140–50
- McGaugh SS, de Blok WJG. 1997. *Ap. J.* 481:689–702
- McLeod AF, Gritschneider M, Dale JE, et al. 2016. *MNRAS* 462:3537–69
- Medling AM, U V, Rich JA, et al. 2015. *MNRAS* 448:2301–11
- Mendoza C, Zeppen CJ. 1983. *MNRAS* 202:981–86
- Mesa-Delgado A, Esteban C. 2010. *MNRAS* 405:2651–67
- Minter AH, Balser DS. 1997. *Ap. J. Lett.* 484:L133–36
- Molina M, Eracleous M, Barth AJ, et al. 2018. *Ap. J.* 864:90
- Morisset C, Delgado-Inglada G, Sánchez SF, et al. 2016. *Astron. Astrophys.* 594:A37
- Moustakas J. 2006. *Spectral diagnostics of galaxy evolution*. PhD Thesis, Univ. Ariz.
- Moustakas J, Kennicutt RC Jr., Tremonti CA, et al. 2010. *Ap. J. Suppl.* 190:233–66
- Moy E, Rocca-Volmerange B. 2002. *Astron. Astrophys.* 383:46–55
- Moy E, Rocca-Volmerange B, Fioc M. 2001. *Astron. Astrophys.* 365:347–59
- Nagamine K, Fukugita M, Cen R, Ostriker JP. 2001. *Ap. J.* 558:497–504
- Nagao T, Maiolino R, De Breuck C, et al. 2013. In *New Trends in Radio Astronomy in the ALMA Era: The 30th Anniversary of Nobeyama Radio Observatory*, eds. R Kawabe, N Kuno, S Yamamoto. *ASP Conf. Ser.* 476:29–32
- Nagao T, Maiolino R, Marconi A. 2006. *Astron. Astrophys.* 459:85–101
- Nagao T, Maiolino R, Marconi A, Matsuhara H. 2011. *Astron. Astrophys.* 526:A149
- Nagar NM, Falcke H, Wilson AS. 2005. *Astron. Astrophys.* 435:521–43

- Naiman JP, Pillepich A, Springel V, et al. 2018. *MNRAS* 477:1206–24
- Nakajima K, Ouchi M, Shimasaku K, et al. 2013. *Ap. J.* 769:3
- Negrete CA, Dultzin D, Marziani P, Sulentic JW. 2012. *Ap. J.* 757:62
- Nicholls DC, Dopita MA, Sutherland RS. 2012. *Ap. J.* 752:148
- Nicholls DC, Sutherland RS, Dopita MA, et al. 2017. *MNRAS* 466:4403–22
- Nieva MF, Przybilla N. 2012. *Astron. Astrophys.* 539:A143
- Nussbaumer H, Schild H. 1979. *Astron. Astrophys.* 75:L17–19
- O'Dell CR, Ferland GJ, Henney WJ, et al. 2015. *Astron. J.* 150:108
- Oey MS, Meurer GR, Yelda S, et al. 2007. *Ap. J.* 661:801–14
- Oey MS, Shields JC. 2000. *Ap. J.* 539:687–705
- Osterbrock DE. 1989. *Astrophysics of Gaseous Nebulae and Active Galactic Nuclei*. Sausalito, CA: Univ. Sci. Books
- Osterbrock DE, Parker RAR. 1966. *Ap. J.* 143:268–70
- Osterbrock DE, Pogge RW. 1985. *Ap. J.* 297:166–76
- Otte B, Gallagher JS III, Reynolds RJ. 2002. *Ap. J.* 572:823–37
- Pagel BEJ, Edmunds MG, Blackwell DE, et al. 1979. *MNRAS* 189:95–113
- Pagel BEJ, Edmunds MG, Smith G. 1980. *MNRAS* 193:219–30
- Park JW, Min KW, Seon KI, et al. 2010. *Ap. J.* 719:1964–68
- Pauldrach A, Puls J, Kudritzki RP. 1986. *Astron. Astrophys.* 164:86–100
- Pauldrach AWA, Hoffmann TL, Lennon M. 2001. *Astron. Astrophys.* 375:161–95
- Pauldrach AWA, Vanbeveren D, Hoffmann TL. 2012. *Astron. Astrophys.* 538:A75
- Peña-Guerrero MA, Peimbert A, Peimbert M. 2012. *Ap. J. Lett.* 756:L14
- Peimbert A, Peimbert M. 2010. *Ap. J.* 724:791–98
- Peimbert A, Peimbert M. 2013. *Ap. J.* 778:89
- Peimbert M. 1967. *Ap. J.* 150:825–34
- Peimbert M, Costero R. 1969. *Bol. Obs. Tonantzintla Tacubaya* 5:3–22
- Peimbert M, Peimbert A, Delgado-Inglada G. 2017. *Publ. Astron. Soc. Pac.* 129:082001–30
- Peimbert M, Sarmiento A, Fierro J. 1991. *Publ. Astron. Soc. Pac.* 103:815–23
- Peimbert M, Storey PJ, Torres-Peimbert S. 1993. *Ap. J.* 414:626–31
- Peimbert M, Torres-Peimbert S, Luridiana V. 1995. In *Gaseous Nebulae and Star Formation*, ed. M Pena, S Kurtz. *Rev. Mex. Astron. Astrofis. Conf. Ser.* 3:296. Abstr.
- Pellegrini EW, Oey MS, Winkler PF, et al. 2012. *Ap. J.* 755:40
- Pérez E, González Delgado R, Vílchez JM. 2001. *Astrophys. Space Sci. Suppl.* 277:83–86
- Perez J, Michel-Dansac L, Tissera PB. 2011. *MNRAS* 417:580–90
- Pérez-Montero E. 2017. *Publ. Astron. Soc. Pac.* 129:043001
- Pérez-Montero E, Contini T. 2009. *MNRAS* 398:949–60
- Pérez-Montero E, Hägele GF, Contini T, Díaz ÁI. 2007. *MNRAS* 381:125–35
- Pettini M. 2002. In *Chemical Enrichment of Intracuster and Intergalactic Medium*, ed. R Fusco-Femiano, F Matteucci. *ASP Conf. Ser.* 253:181–87
- Pettini M, Pagel BEJ. 2004. *MNRAS* 348:L59–63
- Phillips JP. 2007. *MNRAS* 380:369–73
- Phillips JP. 2008. *New Astron. Rev.* 13:60–64
- Phillips MM, Jenkins CR, Dopita MA, et al. 1986. *Astron. J.* 91:1062–85
- Pilyugin LS, Thuan TX. 2005. *Ap. J.* 631:231–43
- Piovan L, Tantaló R, Chiosi C. 2006. *MNRAS* 366:923–44
- Poetrodojo HM, Groves B, Kewley LJ, et al. 2018. *MNRAS* 479:5235–65
- Popescu CC, Tuffs RJ. 2013. *MNRAS* 436:1302–21
- Popescu CC, Yang R, Tuffs RJ, et al. 2017. *MNRAS* 470:2539–58
- Proxauf B, Öttl S, Kimeswenger S. 2014. *Astron. Astrophys.* 561:A10
- Ramirez-Ballinas I, Hidalgo-Gómez AM. 2014. *MNRAS* 442:2282–95
- Ramos-Larios G, Phillips JP, Pérez-Grana JA. 2010. *MNRAS* 405:245–56
- Rand RJ. 1998. *Publ. Astron. Soc. Pac.* 15:106–10
- Rich JA, Dopita MA, Kewley LJ, Rupke DSN. 2010. *Ap. J.* 721:505–17

- Rich JA, Kewley LJ, Dopita MA. 2011. *Ap. J.* 734:87
- Rich JA, Kewley LJ, Dopita MA. 2015. *Ap. J. Suppl.* 221:28
- Rich JA, Torrey P, Kewley LJ, et al. 2012. *Ap. J.* 753:5
- Rigby JR, Bayliss MB, Chisholm J, et al. 2018. *Ap. J.* 853:87
- Rigby JR, Wuyts E, Gladders MD, et al. 2011. *Ap. J.* 732:59
- Rix SA, Pettini M, Leitherer C, et al. 2004. *Ap. J.* 615:98–117
- Rocca-Volmerange B, Lequeux J, Maucherat-Joubert M. 1981. *Astron. Astrophys.* 104:177–84
- Rosa DA, Dors OL, Krabbe AC, et al. 2014. *MNRAS* 444:2005–21
- Rose M, Tadhunter C, Ramos Almeida C, et al. 2018. *MNRAS* 474:128–56
- Rubin RH. 1968. *Ap. J.* 153:761–82
- Rubin RH. 1969. *Ap. J.* 157:1461–62
- Rubin RH, Simpson JP, Lord SD, et al. 1994. *Ap. J.* 420:772–82
- Rubin RH, Simpson JP, O'Dell CR, et al. 2011. *MNRAS* 410:1320–48
- Rubin VC, Ford WK, Whitmore BC. 1984. *Ap. J. Lett.* 281:L21–24
- Rupke DSN, Kewley LJ, Barnes JE. 2010. *Ap. J. Lett.* 710:L156–60
- Salim S, Lee JC, Ly C, et al. 2014. *Ap. J.* 797:126
- Sánchez SF, Rosales-Ortega FF, Iglesias-Páramo J, et al. 2014. *Astron. Astrophys.* 563:A49
- Sánchez SF, Rosales-Ortega FF, Jungwiert B, et al. 2013. *Astron. Astrophys.* 554:A58
- Sarzi M, Shields JC, Schawinski K, et al. 2010. *MNRAS* 402:2187–210
- Savaglio S, Glazebrook K, Le Borgne D, et al. 2005. *Ap. J.* 635:260–79
- Schaerer D. 2013. In *The First Galaxies*, ed. T Wiklind, B Mobasher, V Bromm. *Astrophys. Space Sci. Libr.* 396:345–76. Berlin/Heidelberg: Springer
- Schmutz W, Hamann WR, Wessolowski U. 1989. *Astron. Astrophys.* 210:236–48
- Schneider N, Bontemps S, Motte F, et al. 2016. *Astron. Astrophys.* 591:A40
- Scudder JM, Ellison SL, Mendel JT. 2012. *MNRAS* 423:2690–704
- Seaton MJ. 1958. *MNRAS* 118:504–18
- Seaton MJ. 1960. *MNRAS* 120:326–37
- Sellmaier FH, Yamamoto T, Pauldrach AWA, Rubin RH. 1996. *Astron. Astrophys.* 305:L37
- Shapley AE, Erb DK, Pettini M, et al. 2004. *Ap. J.* 612:108–21
- Sharp RG, Bland-Hawthorn J. 2010. *Ap. J.* 711:818–52
- Shaw RA, Dufour RJ. 1995. *Publ. Astron. Soc. Pac.* 107:896
- Shields GA. 1974. *Ap. J.* 191:309–16
- Shields GA. 1990. *Annu. Rev. Astron. Astrophys.* 28:525–60
- Shirazi M, Vegetti S, Nesvadba N, et al. 2013. *MNRAS* 440(3):2201–21
- Simón-Díaz S, García-Rojas J, Esteban C, et al. 2011. *Astron. Astrophys.* 530:A57
- Simpson JP, Colgan SWJ, Cotera AS, et al. 2007. *Ap. J.* 670:1115–31
- Simpson JP, Rubin RH, Colgan SWJ, et al. 2004. *Ap. J.* 611:338–52
- Simpson JP, Rubin RH, Erickson EF, Haas MR. 1986. *Ap. J.* 311:895–908
- Singh R, van de Ven G, Jahnke K, et al. 2013. *Astron. Astrophys.* 558:A43
- Skillman ED. 1989. *Ap. J.* 347:883–93
- Smith LJ, Westmoquette MS, Gallagher JS, et al. 2006. *MNRAS* 370:513–27
- Snijders L, Kewley LJ, van der Werf PP. 2007. *Ap. J.* 669:269–88
- Somerville RS, Primack JR. 1999. *MNRAS* 310:1087–110
- Spinoglio L, Pereira-Santaella M, Dasyra KM, et al. 2015. *Ap. J.* 799:21
- Spoon HWW, Marshall JA, Houck JR, et al. 2007. *Ap. J. Lett.* 654:L49–52
- Stanghellini L, Kaler JB. 1989. *Ap. J.* 343:811–27
- Stasińska G. 1980. *Astron. Astrophys.* 84:320–28
- Stasińska G. 2005. *Astron. Astrophys.* 434:507–20
- Stasińska G. 2006. *Astron. Astrophys.* 454:L127–30
- Stasińska G, Cid Fernandes R, Mateus A, et al. 2006. *MNRAS* 371:972–82
- Stasińska G, Izotov Y, Morisset C, Guseva N. 2015. *Astron. Astrophys.* 576:A83
- Steidel CC, Erb DK, Shapley AE, et al. 2010. *Ap. J.* 717:289–322

- Steinacker J, Baes M, Gordon KD. 2013. *Annu. Rev. Astron. Astrophys.* 51:63–104
- Storchi-Bergmann T, Calzetti D, Kinney AL. 1994. *Ap. J.* 429:572–81
- Storey PJ, Hummer DG. 1995. *MNRAS* 272:41–48
- Strickland DK, Heckman TM, Colbert EJM, et al. 2004. *Ap. J.* 606:829–52
- Strömgren B. 1939. *Ap. J.* 89:526–47
- Strömgren B. 1948. *Ap. J.* 108:242–75
- Struve O, Elvey CT. 1938. *Ap. J.* 88:364–68
- Sutherland RS, Dopita MA. 1993. *Ap. J. Suppl.* 88:253–327
- Sutherland RS, Dopita MA. 2017. *Ap. J. Suppl.* 229:34
- Talbot RJ Jr., Arnett WD. 1971. *Ap. J.* 170:409–22
- Tarter CB, Salpeter EE. 1969. *Ap. J.* 156:953–66
- Tarter CB, Tucker WH, Salpeter EE. 1969. *Ap. J.* 156:943–52
- Thomas AD, Dopita MA, Kewley LJ, et al. 2018a. *Ap. J.* 856:89
- Thomas AD, Groves BA, Sutherland RS, et al. 2016. *Ap. J.* 833:266
- Thomas AD, Kewley LJ, Dopita MA, et al. 2018b. *Ap. J. Lett.* 861:L2
- Thornley MD, Schreiber NMF, Lutz D, et al. 2000. *Ap. J.* 539:641–57
- Tinsley BM. 1968. *Ap. J.* 151:547–66
- Tinsley BM. 1972. *Astron. Astrophys.* 20:383–96
- Tinsley BM. 1973. *Ap. J.* 186:35–49
- Tinsley BM, Gunn JE. 1976. *Ap. J.* 203:52–62
- Torres-Flores S, Scarano S, Mendes de Oliveira C, et al. 2014. *MNRAS* 438:1894–908
- Torres-Peimbert S, Peimbert M, Fierro J. 1989. *Ap. J.* 345:186–95
- Torrey P, Cox TJ, Kewley L, Hernquist L. 2012. *Ap. J.* 746:108
- Tremblin P, Minier V, Schneider N, et al. 2013. *Astron. Astrophys.* 560:A19
- Tremonti CA, Heckman TM, Kauffmann G, et al. 2004. *Ap. J.* 613:898–913
- Troncoso P, Maiolino R, Sommariva V, et al. 2014. *Astron. Astrophys.* 563:A58
- Truran JW, Cameron AGW. 1971. *Ap. Space Sci.* 14:179–222
- Tsamis YG, Barlow MJ, Liu XW, et al. 2004. *MNRAS* 353:953–79
- Tsamis YG, Péquignot D. 2005. *MNRAS* 364:687–704
- Tsamis YG, Walsh JR, Péquignot D, et al. 2008. *MNRAS* 386:22–46
- Valtchanov I, Virdee J, Ivison RJ, et al. 2011. *MNRAS* 415:3473–84
- Vandenbroucke B, Wood K. 2018. *Astron. Comput.* 23:40–59
- Vazdekis A, Koleva M, Ricciardelli E, et al. 2016. *MNRAS* 463:3409–36
- Veilleux S, Cecil G, Bland-Hawthorn J. 2005. *Annu. Rev. Astron. Astrophys.* 43:769–826
- Veilleux S, Osterbrock DE. 1987. *Ap. J. Suppl.* 63:295–310
- Veilleux S, Shopbell PL, Rupke DS, et al. 2003. *Astron. J.* 126:2185–208
- Vidal-García A, Charlot S, Bruzual G, Hubeny I. 2017. *MNRAS* 470:3532–56
- Vila-Costas MB, Edmunds MG. 1992. *MNRAS* 259:121–45
- Vilchez JM, Esteban C. 1996. *MNRAS* 280:720–34
- Villar-Martin M, Binette L, Fosbury RAE. 1996. *Astron. Astrophys.* 312:751–60
- Villar-Martin M, Tadhunter C, Clark N. 1997. *Astron. Astrophys.* 323:21–30
- Walch S, Whitworth AP, Bisbas TG, et al. 2015. *MNRAS* 452:2794–803
- Wang W, Liu XW, Zhang Y, Barlow MJ. 2004. *Astron. Astrophys.* 427:873–86
- Wang X, Jones TA, Treu T, et al. 2018. *Ap. J.* Submitted. arXiv:1808.08800
- Weber JA, Pauldrach AWA, Hoffmann TL. 2015. *Astron. Astrophys.* 583:A63
- Weiner BJ, Coil AL, Prochaska JX, et al. 2009. *Ap. J.* 692:187–211
- Wild V, Heckman T, Charlot S. 2010. *MNRAS* 405:933–47
- Wild V, Kauffmann G, White S, et al. 2008. *MNRAS* 388:227–41
- Williams RE. 1967. *Ap. J.* 147:556–74
- Wu YZ, Zhang SN, Zhao YH, Zhang W. 2016. *MNRAS* 457:2929–35
- Wuyts E, Kurk J, Förster Schreiber NM, et al. 2014. *Ap. J. Lett.* 789:L40
- Wyse RFG, Silk J. 1985. *Ap. J. Lett.* 296:L1–5

- Xiao L, Stanway ER, Eldridge JJ. 2018. *MNRAS* 477:904–34
- Yan R, Blanton MR. 2012. *Ap. J.* 747:61
- Yates RM, Kauffmann G, Guo Q. 2012. *MNRAS* 422:215–31
- Yeh SCC, Matzner CD. 2012. *Ap. J.* 757:108–26
- Yin SY, Liang YC, Hammer F, et al. 2007. *Astron. Astrophys.* 462:535–46
- Yuan TT, Kewley LJ, Richard J. 2013. *Ap. J.* 763:9
- Yuan TT, Kewley LJ, Swinbank AM, Richard J. 2012. *Ap. J.* 759:66–77
- Zahid HJ, Dima GI, Kudritzki RP, et al. 2014. *Ap. J.* 791:130
- Zahid HJ, Geller MJ, Kewley LJ, et al. 2013a. *Ap. J. Lett.* 771:L19
- Zahid HJ, Kashino D, Silverman JD, et al. 2013b. *Ap. J.* 792:75–93
- Zahid HJ, Kewley LJ, Bresolin F. 2011. *Ap. J.* 730:137
- Zanstra H. 1951. *Bull. Astron. Inst. Neth.* 11:359
- Zastrow J, Oey MS, Pellegrini EW. 2013. *Ap. J.* 769:94
- Zetterlund E, Levesque EM, Leitherer C, Danforth CW. 2015. *Ap. J.* 805:151
- Zhang K, Yan R, Bundy K, et al. 2017. *MNRAS* 466:3217–43
- Zuckerman B, Aller LH. 1986. *Ap. J.* 301:772–89



Contents

Nancy Grace Roman and the Dawn of Space Astronomy <i>Nancy Grace Roman</i>	1
Angular Momentum Transport in Stellar Interiors <i>Conny Aerts, Stéphane Mathis, and Tamara M. Rogers</i>	35
Millimeterwave and Submillimeterwave Laboratory Spectroscopy in Support of Observational Astronomy <i>Susanna L. Widicus Weaver</i>	79
Cometary Chemistry and the Origin of Icy Solar System Bodies: The View After <i>Rosetta</i> <i>Kathrin Altwegg, Hans Balsiger, and Stephen A. Fuselier</i>	113
The Properties of the Solar Corona and Its Connection to the Solar Wind <i>Steven R. Cranmer and Amy R. Winebarger</i>	157
New View of the Solar Chromosphere <i>Mats Carlsson, Bart De Pontieu, and Viggo H. Hansteen</i>	189
Star Clusters Across Cosmic Time <i>Mark R. Krumholz, Christopher F. McKee, and Joss Bland-Hawthorn</i>	227
The Most Luminous Supernovae <i>Avisbay Gal-Yam</i>	305
Cosmological Tests of Gravity <i>Pedro G. Ferreira</i>	335
The Faintest Dwarf Galaxies <i>Joshua D. Simon</i>	375
Fast Radio Bursts: An Extragalactic Enigma <i>James M. Cordes and Shami Chatterjee</i>	417
Relativistic Jets from Active Galactic Nuclei <i>Roger Blandford, David Meier, and Anthony Readhead</i>	467
Understanding Galaxy Evolution Through Emission Lines <i>Lisa J. Kewley, David C. Nicholls, and Ralph S. Sutherland</i>	511

Accuracy and Precision of Industrial Stellar Abundances <i>Paula Jofré, Ulrike Heiter, and Caroline Soubiran</i>	571
Exoplanetary Atmospheres: Key Insights, Challenges, and Prospects <i>Nikku Madhusudhan</i>	617

Indexes

Cumulative Index of Contributing Authors, Volumes 46–57	665
Cumulative Index of Article Titles, Volumes 46–57	668

Errata

An online log of corrections to *Annual Review of Astronomy and Astrophysics* articles may be found at <http://www.annualreviews.org/errata/astro>